



scale room-corridor-room enclosure. This configuration is geometrically similar to a full-scale fire test facility, where local conditions were characterized near five ionization type smoke detectors placed throughout the enclosure. The full-scale fire and salt-water model results were scaled using the fundamental equations that govern dispersion. An evaluation of the local conditions and dispersive event times for both systems was used to formulate a preliminary predictive detector response model for use with the hydraulic analogue.

PREDICTING SMOKE DETECTOR RESPONSE USING A QUANTITATIVE  
SALT-WATER MODELING TECHNIQUE

by

Sean Phillip Jankiewicz

Thesis submitted to the Faculty of the Graduate School of the  
University of Maryland, College Park in partial fulfillment  
of the requirements for the degree  
Master of Science  
2004

Advisory Committee:  
Professor André W. Marshall, Chair  
Professor Richard J. Roby  
Professor James G. Quintiere  
Professor Arnaud Trouvé



## Acknowledgements

The work presented in this Master's Thesis was fully funded by Combustion Science and Engineering, Inc. in Columbia Maryland. I wanted to thank Richard Roby, Mike Klassen, and the rest of the Combustion Science team for this great opportunity to expand my knowledge; you all will never be forgotten. I would like to thank Professor André Marshall, my advisor, mentor, and friend. Not only did Dr. Marshall spend countless hours with me in the lab but also his guidance, knowledge and support allowed me to overcome several obstacles and acquire a vast array of knowledge throughout the completion of this work.

I would also like to extend a note of gratitude to the rest of my thesis committee, Professor Richard Roby, Professor James Quintiere, and Professor Arnaud Trouvé. The support from each member of my committee has truly been appreciated. A special thanks is in order for Xiaobo Yao for his aid in this research, without his help I don't know how this project could have been completed. In addition I would like to thank my family for providing a strong foundation for learning and assisting me in more ways than can be expressed throughout my collegiate experience. Last but not least, I would like to thank my loving girlfriend Heather Martin, for her immeasurable emotional support throughout this research. Thank you all for helping me get through this.

## Table of Contents

List of Tables.....	v
List of Figures.....	vi
Chapter 1. Introduction.....	1
1.1 Overview.....	1
1.2 Literature Review.....	6
1.3 Research Objectives.....	13
Chapter 2. Scaling.....	15
2.1 Appropriate Scales for Fire / Salt-Water Analogy.....	16
2.1.1 Determination of the Velocity Scale.....	16
2.1.2 Source Based Scaling for Fires.....	17
2.1.3 Source Based Scaling for Salt-Water Analog.....	20
2.2 Dimensionless Equations for Fire / Salt-Water Analogy.....	23
2.2.1 Governing Equations for the Fire Flow.....	23
2.2.2 Governing Equations for the Salt-Water Flow.....	28
Chapter 3. Experimental Approach.....	32
3.1 Experimental Test Facility.....	32
3.1.1 Gravity Feed System.....	33
3.1.2 Model Description.....	35
3.1.3 Injection System.....	36
3.1.4 Recirculation System.....	37
3.1.5 Positioning System.....	38
3.1.6 Optics.....	38
3.1.7 Image Acquisition.....	41
3.2 Quantitative Methodology.....	41
3.2.1 Injection Consideration.....	41
3.2.2 PLIF Requirements.....	44
3.2.3 Optimizing Image Quality.....	47
3.2.4 Light Sheet Distribution.....	50
3.2.5 Converting Light Intensity Measurements to Salt Mass Fraction, $Y_{salt}$ .....	51
3.3 Experimental Procedure.....	54
Chapter 4. Analysis.....	55
4.1 Calculating Dimensionless Parameters for Fire Test Data.....	55
4.1.1 Dimensionless Energy Release Rate, $Q^*$ .....	58
4.1.2 Dimensionless Fire Time, $t_{fire}^*$ .....	59
4.1.3 Dimensionless Thermal Dispersion Signature, $\theta_r^*$ .....	59
4.1.4 Converting Optical Measurements to Smoke Mass Fraction, $Y_{smoke}$ .....	60

4.1.5 Dimensionless Smoke Dispersion Signature, $\theta_{smoke}^*$ .....	61
4.2 Calculating Dimensionless Parameters for Salt-Water Model .....	62
4.2.1 Dimensionless Salt Mass Flux, $\dot{m}_{salt}^*$ .....	63
4.2.2 Dimensionless Salt-Water Model Time, $t_{sw}^*$ .....	64
4.2.3 Dimensionless Salt Dispersion Signature, $\theta_{sw}^*$ .....	64
4.3 Converting from Salt-Water to Fire Quantities .....	65
Chapter 5. Results and Discussion.....	67
5.1 Salt-Water Dispersion Analysis.....	67
5.1.1 Initial Plume and Ceiling Jet.....	67
5.1.2 Initial Doorway Flow Dynamics.....	70
5.1.3 Corridor Frontal Flow Dynamics.....	72
5.1.4 Secondary Doorway Flow Dynamics .....	74
5.2 Fire Response Time Analysis .....	76
5.2.1 Local Conditions at the Time of Alarm .....	77
5.2.2 Dispersion and Detector Response Times .....	80
5.3 Predicting Detector Response Time.....	82
5.3.1 Front Arrival Comparison.....	83
5.3.2 Activation Lag Time .....	84
5.3.3 Detector Response Time Predictions .....	85
5.4 Salt-Water and Fire Dispersive Parameter Comparison .....	87
5.4.1 Dispersion Comparison at Activation Time .....	87
5.4.2 Evolving Dispersion Signature Comparison.....	89
Chapter 6. Conclusions.....	98
Appendix A: Experimental Results .....	100
Appendix B: Check List.....	101
Appendix C: Experimental Procedure .....	102
Bibliography .....	111

## List of Tables

TABLE 1: MORTON LENGTH SCALE FOR SALT-WATER INLET CONDITIONS.....	43
TABLE 2: DIMENSIONLESS TURBULENCE CRITERION.....	44
TABLE 3: PREDICTED DETECTOR RESPONSE TIMES.....	87
TABLE 4: FULL-SCALE FIRE EXPERIMENTAL RESULTS.....	100
TABLE 5: NON-DIMENSIONAL FIRE EXPERIMENTAL RESULTS.....	100
TABLE 6: NON-DIMENSIONAL SALT-WATER MODEL EXPERIMENTAL RESULTS.....	100

## List of Figures

FIGURE 1: ENCLOSURE MODEL AND SMOKE DETECTOR LOCATIONS .....	5
FIGURE 2: SCHEMATIC OF THE EXPERIMENTAL TEST FACILITY.....	32
FIGURE 3: GRAVITY FEED DELIVERY SYSTEM AND CONTROL VALVE SETUP.....	34
FIGURE 4: FLOW CONTROL SYSTEM AND METERING DEVICE.....	34
FIGURE 5: PHOTOGRAPH OF ROOM-CORRIDOR-ROOM MODEL .....	36
FIGURE 6: SALINE SOLUTION INJECTION SYSTEM.....	37
FIGURE 7: MODEL STAND AND POSITIONING SYSTEM.....	39
FIGURE 8: OPTICAL SET UP .....	39
FIGURE 9: OPTICAL DESCRIPTION OF SPATIAL FILTER .....	40
FIGURE 10: MAXIMUM INCIDENT PATH LENGTH W/O ABSORBSION .....	46
FIGURE 11: LIGHT INTENSITY PROFILE (+/-) CAMERA GAIN .....	48
FIGURE 12: NORMALIZED LIGHT INTENSITY PROFILE (+/-) CAMERA GAIN.....	48
FIGURE 13: LIGHT INTENSITY VS. SALT MASS FRACTION.....	53
FIGURE 14: LOCAL $T_{\text{FIRE}}$ IN FULL-SCALE FIRE EXPERIMENT .....	56
FIGURE 15: LOCAL $\theta_T^*$ IN FULL-SCALE FIRE EXPERIMENT .....	56
FIGURE 16: LOCAL $Y_{\text{SMOKE}}$ IN FULL-SCALE FIRE EXPERIMENT .....	57
FIGURE 17: LOCAL $\theta_{\text{smoke}}^*$ IN FULL-SCALE FIRE EXPERIMENT .....	57
FIGURE 18: LOCAL $Y_{\text{SALT}}$ IN SALT-WATER MODEL.....	62
FIGURE 19: LOCAL $\theta_{\text{sw}}^*$ IN SALT-WATER MODEL .....	63
FIGURE 20: PLANAR SHEET LOCATION #1.....	68
FIGURE 21: PLUMES INTERACTION WITH CEILING (SERIES) .....	69

FIGURE 22: SOURCE ROOM CEILING LAYER / DOORWAY SPILL (SERIES).....	71
FIGURE 23: PLANAR SHEET LOCATION #3.....	72
FIGURE 24: CORRIDOR FLOW DYNAMICS (SERIES).....	73
FIGURE 25: PLANAR SHEET LOCATION #4.....	74
FIGURE 26: CORRIDOR TO ADJACENT ROOM DOORWAY SPILL (SERIES).....	75
FIGURE 27: ENCLOSURE AND SMOKE DETECTOR LOCATIONS.....	76
FIGURE 28: LOCALIZED GAS TEMPERATURE RISE.....	78
FIGURE 29: LOCALIZED SMOKE MASS FRACTION.....	79
FIGURE 30: CEILING-MOUNTED SMOKE DETECTOR RESPONSE (FIRE).....	81
FIGURE 31: SIDEWALL-MOUNTED SMOKE DETECTOR RESPONSE (FIRE).....	81
FIGURE 32: DIMENSIONLESS FRONT ARRIVAL TIME.....	84
FIGURE 33: DIMENSIONLESS ACTIVATION LAG TIME.....	85
FIGURE 34: PREDICTED SMOKE DETECTOR RESPONSE TIME.....	86
FIGURE 35: DIMENSIONLESS DISPERSION PARAMETER AT DETECTION.....	89
FIGURE 36: EVOLUTION OF DISPERSION (RM1 – C).....	92
FIGURE 37: EVOLUTION OF DISPERSION (RM1 – S).....	93
FIGURE 38: EVOLUTION OF DISPERSION (COR – C).....	94
FIGURE 39: EVOLUTION OF DISPERSION (COR – S).....	97
FIGURE 40: EVOLUTION OF DISPERSION (RM2 - C).....	97

# Chapter 1. Introduction

## 1.1 Overview

The prediction of detector response times is an extremely important issue and has been one of great debate in the field of fire science. From a life safety aspect, it is important to understand that the majority of fatalities from fire are due to smoke inhalation in areas that are far from the fire source. Proper detection devices that notify occupants early on reduce evacuation times and subsequent exposure to hazardous conditions. Smoke detection devices have slowly evolved with advances in technology. With this evolution much work has been done to optimize their functionality with the majority of focus being placed on reducing nuisance alarms. There is ongoing research in determining important flow properties that govern detection; however accurately predicting detection based on flow properties is still a challenge. Previous studies have attempted to develop empirical correlations linking localized gas properties with ionization smoke detector response. The accuracy of these studies is extremely limited. Furthermore, these studies did little to advance the current understanding of the physics behind the detection device and its interaction with the surrounding environment. The variables associated with the fuel type, the specific detection device and its radial distance from the source plume must not be neglected. Thus, finding a general rule of thumb for determining detector response times is unlikely.

The response of smoke detectors is strongly governed by the dispersive behavior of the fire gasses. Characterizing detection behavior is useful for fire analysis and investigation and improving the performance of detectors. Photoelectric and ionization smoke

detectors are the most common detection devices used today and the current study is limited to the examination of ionization type smoke detectors, due to the limited test data available. However, the general finding of this work can be extended to include other types of detectors. The current study uses modeling to assess the practicality of predicting ionization type detector response times.

For many years, engineers and designers have implemented model studies to predict the behavior of a physical system of interest.<sup>1</sup> The physical system of interest is often called the prototype. It is understood that there are two objectives in developing a prototype: (i) to test that we fully understand the fundamentals of the physical process; and (ii) to provide an alternative to carrying out a large number of expensive, full scale tests to discover the effect of varying different parameters. For both, it is necessary to check the results against experimental data.<sup>2</sup> There are both analytical (computer) and physical (laboratory) models that allow such predictions to be made.

Because of the hazardous conditions and inherently destructive nature of fire, models are used extensively to study fire behavior. Analytical fire modeling includes examples ranging from complex computational fluid dynamic simulators to simple zone models. These tools are used to predict the evolution of temperature and smoke conditions within an enclosure at a fraction of the cost and time associated with full scale fire testing. Physical modeling is also performed extensively in fire research. Scaled down reacting experiments of small fires or certain aspects of fires are often studied. Salt-water modeling is an excellent example of a physical model to study fire induced flows.

Previous work has been performed using salt-water introduced into a fresh-water environment as a means to recreate the buoyant characteristics associated with the flows of a hot fire plume. Salt-water modeling physically reproduces the dispersion dynamics related to an adiabatic enclosure fire while allowing experiments to be conducted with little cost and at a laboratory scale. The current investigation evaluates the strengths and weaknesses of this technique and the practicality of using this model to characterize the response of ionization type smoke detectors in a particular fire scenario.

While the development of a valid physical model could prove to be an invaluable tool in the prediction of smoke dispersion within complex compartments, it is imperative that the design criteria and limitations be well documented and understood. For the salt-water model to be considered true, a series of similarity requirements must be met, which necessitates the matching of non-dimensional groups. Models for which all of the similarity requirements are not met are called distorted models. Salt-water modeling is considered a distorted model because many but not all dimensionless groups can be matched.

For successful use of salt-water modeling as a predictive tool, it is imperative that the results be interpreted in a manner consistent with the initial design intentions. As with most models, simplifying assumptions are made with regard to the variables of interest. Thus, some uncertainty is expected when interpreting results from the model. In the

current investigation predictive results are compared to the prototype data, in order to validate the salt-water model, in an analogous reproduction of the actual experiment.

In this study, a 1/7<sup>th</sup> scale model is constructed using clear polycarbonate. The model used in the salt-water experiments is shown in Figure 1. It is geometrically similar to a full-scale room-corridor-room test facility located at Combustion Science and Engineering, Inc. in Columbia, MD. The full-scale test facility consisted of two 7.5 ft. by 8.5 ft. rooms connected by a 3.5 ft. by 15 ft. corridor with an enclosure height of 8 ft. The full-scale tests conducted at this facility included three ceiling and two side wall ionization type smoke detectors in which the local gas temperature and light obscuration are measured just outside of each detector.<sup>3</sup> The mass loss rate of the fuel is monitored during testing, along with the smoke detector activation times at each location. In the current study, the environmental conditions in the full-scale and model enclosures are evaluated at the detector locations with special attention near the time of alarm. The time for the initial ceiling jet front to arrive at a given detector and the delay time associated with the detectors activation is evaluated. This study also examines the trends relating the detector activation times with the fire dispersion dynamics. Salt-water scale model experiments are conducted to test the feasibility of using this modeling technique as a method for predicting smoke detector activation times.

The model is also used in this study to examine the flow characteristics and quantitative conditions observed in a complex geometry. The salt-water model provides detailed

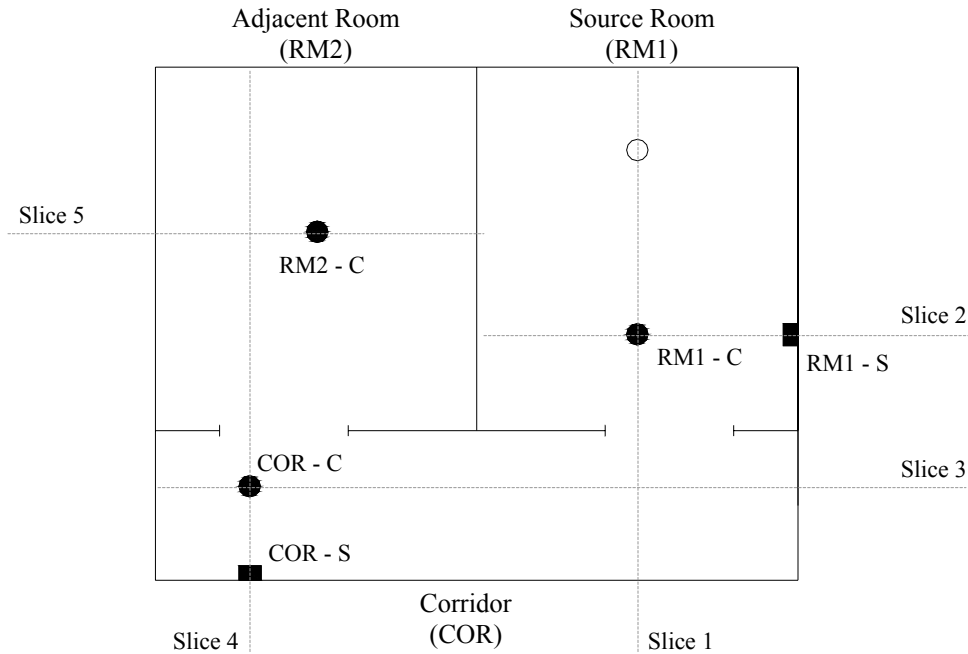


Figure 1: Aerial view of the enclosure model and respective smoke detector locations; dashed lines represent vertical planar laser slice, ○ represents the fire or salt-water source location, ● represents ceiling mounted smoke detectors and ■ represents sidewall mounted smoke detectors

dispersion data for doorway flows, corridor flows, plume/ceiling jet interaction, and general compartment filling. A planar laser induced fluorescence (PLIF) diagnostic technique was used in these salt-water model experiments to measure the dispersion of salt. The dispersion of salt can be related to the dispersion of hot gasses and smoke. The experiments conducted within this study involve introducing a source consisting of a mixture of salt-water solution and a small quantity of dye. The mixing between the salt, the fluorescent dye, and the water is homogeneous and occurs at the molecular level. In the turbulent salt-water flows differential diffusion can be neglected so that the source fluids dilute in the same manner. Thus, the concentration of dye is directly proportional to

the salt-mass fraction within the salt-water, throughout the flow. This source solution is gently introduced into a fresh water environment within the scale model.

The fluorescent dye becomes chemically excited by passing a laser sheet through the flow. The excited dye emits light with an intensity that is a direct function of the dye concentration and the incident laser light. The recorded light intensity, emitted by the dye, is converted into quantitative salt mass fraction data with the use of digital still photography and several post processing tools. The technique provides quantitative spatially and temporally resolved dispersion data within the enclosure.

Digital photography is used to evaluate the PLIF images at various locations of interest and stages of dispersion. The current study uses the PLIF technique in conjunction with salt-water modeling to obtain non-intrusive quantitative measurements of the dispersion dynamics within a complex enclosure. Several planar slices are examined within the enclosure. Data is recorded for various flow conditions and the results are spatially and temporally resolved. The experimental data is used to visualize and characterize plume dispersion throughout the enclosure. Ultimately, a comparison of the salt-water and full-scale fire experiments is made to evaluate salt-water modeling as a predictive tool for determining smoke detector activation times.

## **1.2 Literature Review**

The relationship between salt-water movement in fresh water and hot smoke movement in cool (ambient) air has been a topic of interest for many years in fire science. Several

authors have conducted experiments using salt-water modeling as a qualitative technique in which the flow dynamics of fire induced gasses can be estimated. Thomas et al. used salt-water to model the effect of vents in the removal of smoke from large compartments.<sup>4</sup> Tangren et al. used salt-water to model the smoke layer migration and density changes within a small-ventilated compartment.<sup>5</sup> Zukoski used salt-water modeling to aid in the prediction of smoke movement within high-rise buildings.<sup>6</sup> Steckler, Baum and Quintiere also used this technique to evaluate smoke movement within a Navy combat ship.<sup>7</sup> The experiments conducted within these studies involved mixing saline solution with a dark blue dye for better flow visualization. As the dyed salt-water becomes diluted, which is analogous to air entrainment, the color lightens. The tracer dye allows visualization of the dispersion dynamics and front movement within an enclosure. Sequential imaging of the traced dye, allowed the front arrival times and ceiling layer descent to be examined. This application of salt-water modeling is purely qualitative and does not allow for concentration measurements within the flow to be examined in detail.

More precise measurements have been taken by placing a conductivity probe within the tank at a location of interest. Thus, allowing the salinity of the water to be monitored at a specified point within the test enclosure. It is important to note that the use of conductivity probes disturbs the flow field, allows only point measurements to be taken. There is also a lag time associated with these measurements. Kelly has used this technique in evaluating the movement of smoke within a two-story compartment, in which the salt-water front movement is compared to predictions from FDS.<sup>8</sup> The study

demonstrated that under different flow conditions the analogue results scaled well internally, as did the FDS results for various fire source strengths. The dispersion dynamics for both systems suggest that the salt-water analogue is a useful tool for predicting the front arrival times of the hot gasses produced from a fire. However, dissimilarity is encountered between the magnitudes of the dimensionless dispersion parameters for the FDS and salt-water results. Quantitatively, the differences are difficult to ascertain as a physical analogue model is being compared to an analytical model.

Currently, a quantitative visualization technique called planar laser-induced fluorescence (PLIF) is available that allows non-intrusive measurements to be taken within the entire spatial domain of a planar slice. PLIF is far superior to point measurements because it reveals the instantaneous spatial relationships that are important for understanding complex turbulent flows.<sup>9</sup> Planar laser induced fluorescence is a diagnostic tool that has proven to be effective in measuring concentration fields within mixing reactions, to describe the onset of turbulence in a free air flow and to capture the particular flow phenomena in wave induced motion, just to state a few examples.<sup>10,11, 12</sup> PLIF diagnostics have recently been used in conjunction with salt-water modeling to better visualize the dynamics of dispersion. Law & Wang use PLIF and salt-water modeling to examine of the mixing process associated with turbulent jets and provide insight on the experimental and calibration techniques.<sup>13</sup> Peters et al. describe the bounds associated with PLIF image processing and temporal averaging while assessing the flow dynamics of gravity current heads.<sup>14</sup> A recent validation study has found good agreement between results using PLIF in conjunction with salt-water modeling and the hydrodynamic

simulator of FDS.<sup>15</sup> For the current study this diagnostics technique will be used to quantitatively measure the dispersive dynamics associated within a complex enclosure.

The validity of the salt-water modeling technique is based on the analogy found between the equations that represent dispersion of heat and mass for the fire and salt-water cases, respectively. Baum and Rehim conducted a study on three-dimensional buoyant plumes in enclosures, in which large-scale transport was calculated directly from equations of motion.<sup>16</sup> Within this study, a previous set of “thermally expandable fluid” equations developed by the authors was introduced and the Bousinesq transport equations were derived.<sup>17</sup> The derivation of the non-dimensional governing equations for the flow of in-viscid gas within the enclosure is presented in terms of a fire plume and an injected salt-water plume. The turbulent dispersion dynamics for the fire and salt-water model are analogous and are described by the momentum, mass species and energy equations. Although the mass transport of the salt and dye occurs by molecular diffusion and turbulent mixing, previous studies have concluded that molecular diffusion is insignificant compared to turbulent mixing for a flow not-close to boundaries.<sup>7</sup> The time scales associated with the convection-dominated flows are far too small to concern the effects of the slow diffusion process.<sup>14</sup>

The salt-water modeling test facility used in this study is concurrently being used to examine the dynamics associated with turbulent plume dispersion and plume ceiling jet interactions. Original findings from this work aided in the current study. A detailed evaluation of the governing equations for the analog also revealed more appropriate

scaling parameters for the salt-water equations. The new scaling parameters provide an improved formulation of the salt-water analogy.<sup>18</sup> A detailed dimensional analysis is provided in the Chapter 3, and the dimensional parameters are computed and presented in the analysis section of this study.

An extensive examination of the current literature encompassing the use of salt-water modeling has been conducted for this study, in order to assess the physical and experimental requirements necessary for the model. Morton et al. describe in detail the physical parallel that can be ascertained between the injection of salt water and a buoyant fire plume.<sup>19</sup> The gravitational convective or buoyant characteristics maintain the same general form, provided certain criteria are met. The local changes in density within the plume must be small when compared to the ambient density. Dai et al. reveal that in order to maintain the self-preserving behavior of a turbulent plume, the density within the flow must not be very different from the ambient density, such that

$$\left( \frac{\rho_{\max} - \rho_o}{\rho_o} \right) \ll 1$$

where  $\rho_{\max}$  is the maximum density within cross-section of the flow and  $\rho_o$  is the surrounding fresh water density.<sup>20</sup> This condition is incorporated into the salt-water model to maintain consistency with classical plume theory. Within the salt-water analogue, it is also required that the source does not produce an appreciable amount of momentum at its origin. Morton suggests that the initial momentum of the origin is unimportant at a distance far from the source in which buoyancy dominates the flow dynamics.<sup>21</sup> This distance is characterized by the Morton length scale

$$\frac{l_M}{d} = \left( \frac{\pi}{4} \right)^{1/4} \left( \frac{\rho_o u_{inj}^2}{(gd|\rho_{inj} - \rho_o|)} \right)^{1/2}$$

where  $d$  is the diameter of the source,  $g$  is acceleration due to gravity and  $u_{inj}$  is the injection velocity. For the current study, the Morton length scale is used to determine the flow conditions necessary to produce a buoyancy dominated plume. The momentum effects are considered insignificant and the plume becomes buoyancy dominated at a distance above the source equal to  $5 \times l_M$ .<sup>21</sup>

Past authors have chosen the source strength of the salt-water model to satisfy a critical Reynolds number criterion. A  $Re > 10^4$  based on a buoyant velocity scale and enclosure height has been specified in previous studies to ensure a turbulent flow.<sup>7,8,15</sup> The current study also recognizes the importance of a turbulent flow; however, criterion is specified based on a critical Grashof number. A detailed explanation of this criterion and its effect on the selection of flow conditions is presented in § 3.2.1.

Existing literature demonstrates that salt-water modeling can be a useful tool in describing the flow conditions brought forth by smoke. With this in mind, it may be possible to predict detector response times using the salt-water analog. The little work that has been done in regards to the predictability of smoke detector activation has attempted to describe a threshold for activation with empirical data.<sup>22,23</sup> Until recently the most commonly accepted engineering approach for predicting the activation times of smoke detectors used a temperature-based correlation, in which a temperature rise of 13°C in the vicinity of the detector was used to describe smoke detector activation. This

approach, initially proposed by Heskestad and Delichatsios, used the temperature criterion selected from the experimental results of a wide range of fuels and detector styles in which the values ranged from 2°C to over 20°C.<sup>22</sup> Extensions of this work include investigations of localized temperature and/or light obscuration measurements outside of a detector at the time of activation.<sup>25,26,27,28,29,30</sup> However, neither ionization nor photoelectric smoke detectors operate based on light obscuration or changes in temperature.<sup>31</sup> Furthermore, the details of these empirical predictions are vague and have often been found to lack repeatability.<sup>27,28,29,32</sup>

More advanced studies have been conducted that are more realistic to the operating principles of ionization smoke detectors. These models have been created to describe a threshold based on the fuel specific smoke properties, such as particle size and concentration, and the devices specific entrance dynamics and operational parameters. The details associated with these predictions are beyond the realm of a practical engineering model and include inherent errors associated with the measurements needed.<sup>32</sup> Even when considering a fuel with well-documented properties there still exists a large range in smoke particle sizes (0.005 – 5  $\mu\text{m}$ ), smoke concentrations ( $10^4$  –  $10^{10}$  particles /  $\text{cm}^3$ ) and the effect of smoke aging resulting from particle coagulation and agglomeration, that makes the above prediction in virtually unobtainable outside a laboratory environment.<sup>33</sup> A recent study conducted by Cleary, et al. focuses on quantifying the significance of smoke entry lag as a function of the incident ceiling jet velocity.<sup>34</sup> The entry lag is defined as a combination of the delay associated with the velocity reduction as the smoke enters the sensing chamber (dwell time) and the delay

associated with the mixing that occurs in the sensing chamber (mixing time). The entry lag was determined to be inversely proportional to the velocity for the detectors included in the study. Though, this work provides a detailed means for better understanding detector response, it is still a relatively new concept and the general applicability has not been fully tested.<sup>32</sup>

The findings and recommendations of previous authors provide a strong foundation for this study. Salt-water modeling has been successfully used for the past decade as an analog for the dispersion of hot gasses produced in a fire. While at the same time, one of the most debatable and significant aspects of fire science are found in evaluating detector response times, which are strongly governed by the dispersive behavior of the fire gasses. Yet, no research has been done to evaluate the ability of the salt-water analog to be used as a predictive tool for determining detector activation times. The current study incorporates the use of state of the art laser diagnostics with a well-established physical model to determine the predictive capabilities of salt-water modeling.

### **1.3 Research Objectives**

The primary objective of this study is to examine the use of salt-water modeling as a predictive tool for determining the response time of ionization type smoke detectors. A series of reduced-scale salt-water model experiments was used to recreate full-scale fire tests, which examined the local conditions of five smoke detectors positioned throughout a complex room-corridor-room enclosure. A planar laser induced fluorescence (PLIF) diagnostic technique was used in conjunction with salt-water modeling for quantitative

non-intrusive planar measurements describing the spatial and temporal dispersion behavior.

PLIF visualization provides insight into the dispersive details of the fluid in the regions of interest, i.e. in the vicinity of each detector. The PLIF technique provides opportunity to visualize the various stages of dispersion including; the initial plume regime, the impinging plume ceiling interaction, the ceiling layer descent, as well as the doorway and corridor flow characteristics. A secondary objective of this investigation is to gain insight into dispersive phenomenon within the enclosure.

In order to achieve the primary objective of this investigation, multiple considerations must be made regarding the possible conditions governing detector response. The quantitative capabilities of the PLIF technique are exploited to evaluate the dispersion signature at select locations. These signatures are taken at locations corresponding to detector positions in the full-scale fire test. The time evolution of dispersion parameters from the salt-water model and the full-scale fire are compared with a special focus on the detector activation event. The dispersion parameters include temperature and smoke parameters for the fire and a salt parameter for the salt-water model. In addition, a detailed analysis of the front arrival times for both the full and reduced scale experiments is conducted based on the dispersion parameters signatures. The trends and relative values are used to demonstrate the strengths and weaknesses of using salt-water modeling as a predictive tool for smoke detector response.

## Chapter 2. Scaling

It has been found, through the use of dimensional analysis that a direct link can be made between the thermal strength of the source fire and the salt mass strength of the salt-water source. Assumptions must be made regarding the factors that govern smoke movement for this analogy to be drawn. The salt-water modeling, or the hydraulic analogue technique, represents adiabatic fire conditions where buoyancy is the dominating factor in the migration of smoke within an enclosure. Smoke is dispersed throughout the enclosure and is driven by the hot gasses that accelerate toward the ceiling in the initial plume regime. The buoyant force is a result of the density difference between the hot gasses produced from a fire and the cool ambient environment. Thus, the source strength and the height of the enclosure dictate the manner in which the dispersion occurs. Similarly, salt-water is introduced into a freshwater environment where the density difference creates a buoyant driving force. The plume regime drives the flow with the ceiling height and source strength controlling the dispersion dynamics within the entire enclosure.

Understanding the equations that govern these dynamics allows the similarities and differences to be compared for both the fire and salt-water experiments. By scaling the governing equations, non-dimensional parameters that represent the dispersion dynamics can be obtained. The following section provides a detailed explanation of the appropriate dimensionless terms for both the fire and salt-water analogy and incorporates the appropriate scales into the governing equations that describe the dispersion dynamics of both systems.

This chapter demonstrates the similarities between the governing equations for these flows. A detailed explanation of the methods used to compute and visualize dimensionless variables and parameters for fire analysis is presented in Chapter 4.

## 2.1 Appropriate Scales for Fire / Salt-Water Analogy

### 2.1.1 Determination of the Velocity Scale

The momentum equation with a Boussinesq treatment of the density is provided as

$$\rho_o \left( \frac{\partial u_j}{\partial t} + u_i \frac{\partial u_j}{\partial x_i} \right) = - \frac{\partial (p - p_a)}{\partial x_j} + \mu \frac{\partial^2 u_j}{\partial x_i \partial x_i} + (\rho - \rho_o) f_j, \quad (1)$$

where  $\rho_o$  is the ambient density,  $u_j$  is the velocity vector,  $t$  is the time,  $p$  is the pressure,  $p_a$  is the atmospheric pressure,  $\mu$  dynamic viscosity,  $\rho$  is the fluid density, and  $f_j$  is the body force.

Let us consider scales of terms in a convective buoyancy dominated flow “not close” to a boundary described by Eqn. (1). The scales for these terms are

$$\frac{\rho_o U_o}{\tau_o}; \frac{\rho_o U_o^2}{L} : \frac{p_o}{L}; \frac{\mu U_o}{L^2}; |\rho_{source} - \rho_o| g,$$

where  $L$  is the length scale,  $U_o$  is the velocity scale,  $\tau_o$  is the time scale,  $p_o$  is the pressure scale,  $g$  is the gravitational acceleration constant, and  $p_{source}$  is the source pressure scale.

Assuming transients are governed by a convective time scale,  $\tau_o = \frac{L}{U_o}$ , the terms reduce

to

$$\frac{\rho_o U_o^2}{L} : \frac{p_o}{L}; \frac{\mu U_o}{L^2}; |\rho_{source} - \rho_o| g.$$

Because the flow is convective and buoyancy dominated, the convective and buoyancy terms balance and

$$\frac{\rho_o U_o^2}{L} \sim |\rho_{source} - \rho_o| g.$$

An appropriate velocity scale for a convective buoyancy dominated flow “not close” to the boundary is thus

$$U_o \sim \left( \frac{|\rho_{source} - \rho_o|}{\rho_o} \right)^{1/2} (gL)^{1/2}. \quad (2)$$

It is important to note that if the flow is “close” to the wall, the viscous terms would become important, the appropriate length scales would change, and the corresponding velocity scales would change.

### 2.1.2 Source Based Scaling for Fires

The scale for  $U_o$  is provided in terms of the density deficit,  $|\rho_{source} - \rho_o|/\rho_o$ . For fires the density deficit is not well established and a scale for  $U_o$  and other quantities of interest based on the source strength is more useful. For a fire

$$Q \sim \dot{m}_{fire} c_p (T_{source} - T_o) \quad (3)$$

where  $\dot{m}_{fire}$  is a characteristic mass flux from the fire plume source and  $T_{source}$  is a characteristic temperature of the fire plume source. Furthermore,

$$\frac{Q}{T_o} \sim \dot{m}_{fire} \frac{c_p (T_{source} - T_o)}{T_o}. \quad (4)$$

A scale for the source can be determined by recognizing

$$\dot{m}_{fire} \sim \rho_{source} U_o L_f^2$$

or alternatively,

$$\dot{m}_{fire} \sim \left( \frac{\rho_{source}}{\rho_o} \right) \rho_o U_o L_f^2 \quad (5)$$

Where  $\rho_{source}$  is the density of the source flow. Substituting Eqn. (5) into Eqn. (4) and rearranging results in a new expression for the velocity scale:

$$U_o \sim \left( \frac{Q}{\rho_o c_p T_o L_f^2} \right) \left( \frac{T_{source} - T_o}{T_o} \right)^{-1} \left( \frac{\rho_{source}}{\rho_o} \right)^{-1} \quad (6)$$

This velocity expression has the source strength but also a temperature difference term. More analysis is required to simplify the expression.

For a Boussinesq flow, the density changes are small and a Taylor series expansion can accurately describe the density. For fires, only the effect of temperature on density is considered. Composition changes within the fire-induced flow are assumed to have a negligibly small impact on the density. The density can be expressed as

$$\rho = \rho_o + \left. \frac{\partial \rho}{\partial T} \right|_{p,o} (T - T_o) + \text{Higher order terms} \quad (7)$$

or

$$\rho = [\rho_o - \rho_o \beta_T (T - T_o)] + \text{Higher order terms},$$

where  $\beta_T$  is the volumetric thermal expansion coefficient defined as

$$\beta_T = -\frac{1}{\rho} \frac{\partial \rho}{\partial T}.$$

Furthermore, the fire-induced flow is assumed to behave like an ideal gas so that

$$\rho = \frac{p}{RT} \quad (8)$$

and

$$\left. \frac{\partial \rho}{\partial T} \right|_{p,o} = \frac{-\rho_o}{RT_o^2} = \frac{-\rho_o}{T_o} \quad (9)$$

Combining Eqns. (7) and (9) results in

$$\rho \approx \rho_o - \rho_o \frac{(T - T_o)}{T_o} \quad (10)$$

and  $\beta_T$  is the volumetric thermal expansion coefficient given by

$$\beta_T = \frac{1}{T_o}.$$

The linear expression in Eqn. (10) resulting from the Buossinesq approximation helps to simplify the scales.

Substitution of Eqn. (10) into Eqn. (6) and only retaining leading order terms results in

$$U_o \sim \left( \frac{Q}{\rho_o c_p T_o L_f^2} \right) \left( \frac{(T_{source} - T_o)}{T_o} \right)^{-1}. \quad (11)$$

Furthermore, a relationship between the density deficit and the dimensionless temperature difference is provided by Eqn. (10). Substitution results in

$$\frac{\rho - \rho_o}{\rho} = -\frac{(T - T_o)}{T_o} \quad \text{or} \quad \frac{\rho - \rho_o}{\rho} = -\beta_T (T - T_o). \quad (12)$$

Applying Eqn. (12) and substituting into Eqn. (11) results in

$$U_o \sim \left( \frac{Q}{\rho_o c_p T_o L_f^2} \right) \left( -\frac{(\rho_{source} - \rho_o)}{\rho_o} \right)^{-1}. \quad (13)$$

Combining Eqn. (13) and Eqn. (2) results in an expression relating the density deficit to the source strength given by

$$\left(-\frac{|\rho_{source} - \rho_o|}{\rho_o}\right)^{1/2} (gL_f)^{1/2} \sim \left(\frac{Q}{\rho_o c_p T_o L_f^2}\right) \left(-\frac{(\rho_{source} - \rho_o)}{\rho_o}\right)^{-1}.$$

Recognizing that  $|\rho_{source} - \rho_o| = -(\rho_{source} - \rho_o)$  for a fire and simplifying results in

$$\frac{(\rho_{source} - \rho_o)}{\rho_o} \sim (Q^*)^{2/3}, \quad (14)$$

where

$$Q^* = \left(\frac{Q}{\rho_o c_p T_o g^{1/2} L_f^{5/2}}\right).$$

Substitution of Eqn. (10) into Eqn. (2) results in a scale for  $U_o$  in terms of the source given by

$$U_o \sim (Q^*)^{1/3} (gL_f)^{1/2}. \quad (15)$$

### 2.1.3 Source Based Scaling for Salt-Water Analog

The scale for  $U_o$  is provided in terms of the density deficit,  $|\rho_{source} - \rho_o|/\rho_o$ . Although this quantity can be calculated for salt-water sources, for a completely parallel analogy, a source-based scale for  $U_o$  and other quantities of interest are developed for the salt-water flow just as for the fire flow. For salt-water flows

$$\dot{m}_{salt} = \rho_{source} (Y_{salt}) \dot{V}, \quad (16)$$

where  $\dot{V}$  is the volumetric flow rate of salt-water,  $Y_{salt}$  is the mass fraction of salt in the injected source flow and  $\dot{m}_{salt}$  is the mass flow rate of salt introduced into the system.

Alternatively,

$$\dot{m}_{salt} = \left( \frac{\rho_{source}}{\rho_o} \right) \rho_o (Y_{salt}) \dot{V}.$$

An expression for the mass flux of salt can also be given in terms of a characteristic flow velocity as

$$\dot{m}_{salt} \sim \left( \frac{\rho_{source}}{\rho_o} \right) (\rho_o U_o L_{sw}^2) (Y_{salt}). \quad (17)$$

Rearranging results in

$$U_o \sim \left( \frac{\dot{m}_{salt}}{\rho_o L_{sw}^2} \right) \left( \frac{\rho_{source}}{\rho_o} \right)^{-1} (Y_{salt})^{-1}. \quad (18)$$

This velocity expression has the source strength,  $\dot{m}_{salt}$ , but also a salt mass fraction term,  $Y_{salt}$ . More analysis is required to simplify the expressions.

For the salt-water flow, an empirical expression for the density of salt-water as a function of the salt mass fraction has been established as

$$\rho = \rho_o + 0.76 \rho_o Y_{salt}.$$

The expression was determined from existing data. The empirical expression shows that the salt-water density is a linear function of the salt mass fraction. A first-order Taylor series expansion of the density about changes in mass fraction will also provide a linear relationship for density. This expansion provides some physical insight into the empirical expression. The expansion is given by

$$\rho = \rho_o + \left. \frac{\partial \rho}{\partial Y} \right|_o (Y_{salt}), \quad (19)$$

and similar to the fire case a density modification coefficient,  $\beta_{sw}$  is defined as

$$\beta_{sw} = \frac{1}{\rho} \frac{\partial \rho}{\partial Y}. \quad (20)$$

Substitution of Eqn. (20) into Eqn. (19) and equating results in

$$\rho = \rho_o + \beta_{sw} \rho_o Y_{salt}, \quad (21)$$

where  $\beta_{sw} = 0.76$ . Note the similarity between Eqn. (21) and the expression for temperature based density in Eqn. (10) recognizing that  $\beta_T = 1/T_o$ .

Rearranging Eqn. (21) results in

$$\frac{\rho_{source} - \rho_o}{\rho_o} = \beta_{sw} Y_{source} \quad (22)$$

Comparison of Eqns. (22) and (12) demonstrates the quantities that result in buoyancy for the fire and the salt-water model. in simulating the buoyant force which drives fire induced flows. Substitution of Eqn. (21) into Eqn. (18) and retaining only leading order gives

$$U_o \sim \left( \frac{\dot{m}_{source}}{\rho_o L_{sw}^2} \right) \left( \frac{1}{\beta_{sw}} \right)^{-1} \left( \frac{\rho_{source} - \rho_o}{\rho_o} \right)^{-1} \quad (23)$$

Combining Eqns. (23) and (2) results in

$$\left( \frac{|\rho_{source} - \rho_o|}{\rho_o} \right)^{1/2} (gL_{sw})^{1/2} \sim \left( \frac{\dot{m}_{source}}{\rho_o L_{sw}^2} \right) \left( \frac{1}{\beta_{sw}} \right)^{-1} \left( \frac{\rho_{source} - \rho_o}{\rho_o} \right)^{-1}$$

$$\frac{\rho_{source} - \rho_o}{\rho_o} \sim (\dot{m}^*)^{2/3} \quad (24)$$

where

$$\dot{m}_{sw}^* = \frac{\beta_{sw} \dot{m}_{source}}{\rho_o g^{1/2} L_{sw}^{5/2}} \quad (25)$$

$$\frac{\rho_{source} - \rho_o}{\rho_o} \sim (\dot{m}^*)^{2/3} \quad (24)$$

where

$$\dot{m}_{sw}^* = \frac{\beta_{sw} \dot{m}_{source}}{\rho_o g^{1/2} L_{sw}^{5/2}} \quad (25)$$

Substitution of (24) into (2) results in a velocity scale in terms of the source strength given by

$$U_o \sim (\dot{m}_{sw}^*)^{1/3} (gL_{sw})^{1/2} \quad (26)$$

## 2.2 Dimensionless Equations for Fire / Salt-Water Analogy

### 2.2.1 Governing Equations for the Fire Flow

#### Momentum Equation:

The momentum equation is given by

$$\rho_o \left( \frac{\partial u_j}{\partial t} + u_i \frac{\partial u_j}{\partial x_i} \right) = - \frac{\partial (p - p_o)}{\partial x_j} + \mu \frac{\partial^2 u_j}{\partial x_i \partial x_i} + (\rho - \rho_o) f_j \quad (27)$$

where

$$f_1 = 0, \quad f_2 = -g, \quad f_3 = 0$$

Define dimensionless variables as follows

$$\hat{t} = \frac{t_{fire}}{\tau_o}, \quad x_j^* = \frac{x_j}{L_f}, \quad \hat{u}_j = \frac{u_j}{U_o}, \quad \hat{p} = \frac{p - p_a}{p_o}$$

$$\hat{\theta} = \frac{(\rho - \rho_o) / \rho_o}{(\rho_{source} - \rho_o) / \rho_o}, \quad f_j^* = \frac{f_j}{g}$$

so that

$$f_1^* = 0, \quad f_2^* = -1, \quad f_3^* = 0$$

$$\frac{L_f}{U_o \tau_o} \frac{\partial \hat{u}_j}{\partial \hat{t}} + \hat{u}_i \frac{\partial \hat{u}_j}{\partial x_i^*} = -\frac{p_o}{\rho_o U_o^2} \frac{\partial \hat{p}}{\partial x_i^*} + \frac{\mu}{U_o L_f} \frac{\partial^2 \hat{u}_j}{\partial x_i^* \partial x_i^*} + \frac{(\rho_{source} - \rho_o) g L_f}{\rho U_o^2} \hat{\theta} \cdot f_j^*$$

We will set

$$\frac{L_f}{\tau_o U_o} = 1$$

so that the characteristic development time or transient is based on the flow time. We will also get

$$\frac{p_o}{\rho_o U_o^2} = 1$$

so that the characteristic pressure is based on the flow pressure. Rewriting results in

$$\frac{\partial \hat{u}_j}{\partial \hat{t}} + \hat{u}_i \frac{\partial \hat{u}_j}{\partial x_i^*} = -\frac{\partial \hat{p}}{\partial x_i^*} + \frac{\nu}{U_o L_f} \frac{\partial^2 \hat{u}_j}{\partial x_i^* \partial x_i^*} + \frac{(\rho_{source} - \rho_o) g L_f}{\rho U_o^2} \hat{\theta} \cdot f_j^* \quad (28)$$

The fire induced flow expressions are available in terms of the source strength for  $U_o$  and  $(\rho_{source} - \rho_o)/\rho_o$ . These expressions are given by Eqns. (14) and (15). Substitution of these scale results into expressions for the dimensionless variables in Eqn. (28) gives

$$\frac{\partial u_j^*}{\partial t^*} + u_i^* \frac{\partial u_j^*}{\partial x_i^*} = -\frac{\partial p^*}{\partial x_i^*} + \frac{\nu}{(Q^*)^{1/3} (g L_f)^{1/2} L_f} \frac{\partial^2 u_j^*}{\partial x_i^* \partial x_i^*} + \theta_T^* \cdot f_j^*$$

or

$$\frac{\partial u_j^*}{\partial t^*} + u_i^* \frac{\partial u_j^*}{\partial x_i^*} = -\frac{\partial p^*}{\partial x_i^*} + \frac{1}{(Gr_{source}^{fire})^{1/3}} \frac{\partial^2 u_j^*}{\partial x_i^* \partial x_i^*} + \theta_T^* \cdot f_j^* \quad (29)$$

where

$$\frac{\rho_o c_p T_o \nu^3 g^{1/2} L_f^{5/2}}{Q g^{3/2} L_f^{3/2} L_f^3} = \frac{T_o \mu c_p \nu^2}{Q g L_f^2} = \frac{1}{Gr_{source}^{fire}}$$

or alternatively for an ideal gas

$$Gr_{source}^{fire} = \frac{\beta_T g Q L_f^2}{\rho_o c_p \nu^3} = \frac{g Q L_f^2}{\rho_o c_p T_o \nu^3} \quad (30)$$

And the scaled variables in terms of the source terms are

$$t_{fire}^* = t_{fire} \cdot (g/L_f)^{1/2} (Q^*)^{1/3}, \quad u_j^* = \frac{u_j}{(Q^*)^{1/3} (g L_f)^{1/2}},$$

$$\theta_T^* = \frac{\beta_T (T - T_o)}{(Q^*)^{2/3}}, \quad p^* = \frac{p}{(Q^*)^{2/3} \rho_o g L_f}$$

$$\text{where } \beta_T = \frac{1}{T_o} \quad (31)$$

### Energy Equation:

A dimensionless energy equation is also derived beginning with the energy equation given by

$$\rho_o c_p \left( \frac{\partial T}{\partial t} + u_i \frac{\partial T}{\partial x_i} \right) = k \frac{\partial^2 T}{\partial x_i \partial x_i} + q''' \quad (32)$$

Scale parameters are defined as follows:

$$\hat{t} = \frac{t_{fire}}{\tau_o}, \quad x_i^* = \frac{x_i}{L_f}, \quad \hat{u}_i = \frac{u_i}{U_o}, \quad \hat{q}^* = \frac{\dot{q}''' L_f^3}{Q} \quad (33)$$

$$\theta_T^* = \frac{\beta_T (T - T_o)}{(Q^*)^{2/3}}.$$

Substitution of scales results in

$$\frac{\rho_o c_p (Q^*)^{2/3}}{\beta_T \tau_o} \frac{\partial \theta_T^*}{\partial \hat{t}} + \frac{\rho_o c_p (Q^*)^{2/3} U_o}{\beta_T L_f} \hat{u}_i \frac{\partial \theta_T^*}{\partial x_i^*} = \frac{k (Q^*)^{2/3}}{\beta_T L_f^2} \frac{\partial^2 \theta_T^*}{\partial x_i^* \partial x_i^*} + \frac{Q}{L_f^3} \hat{q}^*.$$

Rearranging results in

$$\frac{L_f}{U_o \tau_o} \frac{\partial \theta_T^*}{\partial \hat{t}} + \hat{u}_i \frac{\partial \theta_T^*}{\partial x_i^*} = \frac{\nu}{U_o L_f} \frac{\alpha}{\nu} \frac{\partial^2 \theta_T^*}{\partial x_i^* \partial x_i^*} + \beta_T \frac{QL_f}{\rho_o c_p (Q^*)^{2/3} U_o L_f^2} \dot{q}^* . \quad (34)$$

Just as before

$$\frac{L_f}{\tau_o U_o} = 1$$

And the scale for  $U_o$  in Eqn. (15) is set equal to  $U_o$ , the scale for  $\beta_T(T - T_o)$  is

determined from Eqns. (12) and (14) and set equal to  $\beta_T(T - T_o)$  yielding

$$\frac{\partial \theta_T^*}{\partial t_{fire}^*} + u_i^* \frac{\partial \theta_T^*}{\partial x_i^*} = \left( \frac{\nu}{(Q^*)^{1/3} g^{1/2} L_f^{1/2} L_f} \right) \frac{\alpha}{\nu} \frac{\partial^2 \theta_T^*}{\partial x_i^* \partial x_i^*} + \dot{q}^* ,$$

or

$$\frac{\partial \theta_T^*}{\partial t_{fire}^*} + u_i^* \frac{\partial \theta_T^*}{\partial x_i^*} = \left( \frac{1}{(Gr_{source}^{fire})^{1/3}} \right) \left( \frac{1}{Pr} \right) \frac{\partial^2 \theta_T^*}{\partial x_i^* \partial x_i^*} + \dot{q}^* , \quad (35)$$

where  $Gr_{source}^{fire}$  is given in Eqn. (30) and

$$Pr = \frac{\nu}{\alpha} .$$

The scaled variables in terms of the source terms are defined in Eqn. (31).

### Smoke Mass Species Equation:

The smoke mass species equation involves generation of smoke due to reaction and dispersion of smoke due to density differences. The dispersion is primarily associated with differences in temperature. Consider the mass species equation describing the dispersion of smoke:

$$\rho_o \left( \frac{\partial Y_{smoke}}{\partial t_{fire}} + u_i \frac{\partial Y_{smoke}}{\partial x_i} \right) = \rho_o D \frac{\partial^2 Y_{smoke}}{\partial x_i \partial x_i} + \dot{w}_{smoke}, \quad (36)$$

where  $Y_{smoke}$  is the smoke mass fraction,  $D$  is the mass diffusion coefficient, and  $\dot{w}_{smoke}$  is the smoke generation term. Scaling parameters are defined to create a non-dimensional equation. The non-dimensional equation reveals important dimensionless parameters that govern the smoke dispersion. Scale parameters are defined as

$$\hat{t} = \frac{t_{fire}}{\tau_o}, \quad x_i^* = \frac{x_i}{L_f}, \quad \hat{u}_i = \frac{u_i}{U_o}, \quad w_{smoke}^* = \frac{\dot{w}_{smoke} L_f^3}{\dot{m}_{smoke}}$$

Substitution results in

$$\frac{L_f}{U_o \tau_o} \frac{\partial Y_{smoke}}{\partial \hat{t}} + \hat{u}_i \frac{\partial Y_{smoke}}{\partial x_i^*} = \frac{D}{U_o L_f} \frac{\partial^2 Y_{smoke}}{\partial x_i^* \partial x_i^*} + \frac{w_{smoke}^* \dot{m}_{smoke}}{U_o \rho_o L_f^2}, \quad (37)$$

In the fire, the velocity scale is given by Eqn. (15).

It should also be recognized that

$$\dot{m}_{smoke} = (\dot{m}_{fuel})(y_{smoke}) = \frac{Q(y_{smoke})}{\Delta H_c} \quad (38)$$

Using the characteristic flow time  $\tau_o = L_f / U_o$  and substituting Eqns. (38) and the fire velocity scale into Eqn. (37) yields

$$\frac{\partial Y_{smoke}}{\partial \hat{t}} + \hat{u}_i^* \frac{\partial Y_{smoke}}{\partial x_i^*} = \frac{D}{U_o L_f} \frac{\partial^2 Y_{smoke}}{\partial x_i^* \partial x_i^*} + \frac{w_{smoke}^* Q(y_{smoke})}{\rho_o \Delta H_c (Q^*)^{1/3} g^{1/2} L_f^{5/2}}.$$

The source term can be reduced yielding

$$\frac{\partial Y_{smoke}}{\partial \hat{t}} + \hat{u}_i^* \frac{\partial Y_{smoke}}{\partial x_i^*} = \frac{D}{(Q^*)^{1/3} (gL_f)^{1/2} L_f} \frac{\partial^2 Y_{smoke}}{\partial x_i^* \partial x_i^*} + \frac{w_{smoke}^* (Q^*)^{1/3} y_{smoke} c_p T_o}{\Delta H_c}. \quad (39)$$

A dimensionless smoke dispersion parameter can be defined as

$$\theta_{smoke}^* = \frac{Y_{smoke} \Delta H_c}{y_{smoke} c_p T_o (Q^*)^{2/3}}. \quad (40)$$

Substituting Eqn. (40) into Eqn. (39) results in

$$\frac{\partial \theta_{smoke}^*}{\partial t^*} + u_i^* \frac{\partial \theta_{smoke}^*}{\partial x_i^*} = \frac{D}{(Q^*)^{1/3} (gL_f)^{1/2} L_f} \frac{\partial^2 \theta_{smoke}^*}{\partial x_i^* \partial x_i^*} + w_{smoke}^*.$$

Recall the definition  $Gr_{source}^{fire}$  provided in Eqn. (30). Substitution results in

$$\frac{\partial \theta_{smoke}^*}{\partial t^*} + u_i^* \frac{\partial \theta_{smoke}^*}{\partial x_i^*} = \frac{1}{(Gr_{source}^{fire})^{1/3} Sc} \frac{\partial^2 \theta_{smoke}^*}{\partial x_i^* \partial x_i^*} + w_{smoke}^*$$

The dimensionless variables are

$$t_{fire}^* = \frac{t_{fire}}{(Q^*)^{-1/3} (g/L_f)^{-1/2}}, \quad u_j^* = \frac{u_j}{(gL_f)^{1/2} (Q^*)^{1/3}}, \quad \theta_{smoke}^* = \frac{\beta_T \Delta H_c Y_{smoke}}{y_{smoke} c_p (Q^*)^{2/3}}$$

$$\text{where } \beta_T = \frac{1}{T_o}.$$

## 2.2.2 Governing Equations for the Salt-Water Flow

### Momentum Equation:

The momentum equation is given by

$$\rho_o \left( \frac{\partial u_j}{\partial t} + u_i \frac{\partial u_j}{\partial x_i} \right) = - \frac{\partial (p - p_o)}{\partial x_j} + \mu \frac{\partial^2 u_j}{\partial x_i \partial x_i} + (\rho - \rho_o) f_j, \quad (41)$$

where

$$f_1 = 0, \quad f_2 = -g, \quad f_3 = 0$$

Define parameters as follows

$$\hat{t} = \frac{t}{\tau_o}, \quad x_j^* = \frac{x_j}{L_{sw}}, \quad \hat{u}_j = \frac{u_j}{U_o}, \quad p^* = \frac{p - p_o}{p_o} \quad (42)$$

$$\hat{\theta} = \frac{(\rho - \rho_o)}{(\rho_{source} - \rho_o) / \rho_o}, \quad f_j^* = \frac{f_j}{g} \text{ so that } f_1 = 0, \quad f_2 = 1, \quad f_3 = 0$$

Substitution of these scales results in

$$\frac{\rho_o U_o}{\tau_o} \frac{\partial \hat{u}_j}{\partial \hat{t}} + \frac{\rho_o U_o^2}{L_{sw}} \hat{u}_i \frac{\partial \hat{u}_j}{\partial x_i^*} = - \frac{\rho_o}{L_{sw}} \frac{\partial p^*}{\partial x_j^*} + \frac{\mu U_o}{L_{sw}^2} \frac{\partial^2 \hat{u}_j}{\partial x_i^* \partial x_i^*} + \frac{(\rho_{source} - \rho_o)}{\rho_o} g \hat{\theta} \cdot f_j^*$$

Rearranging results in

$$\frac{L_{sw}}{U_o \tau_o} \frac{\partial \hat{u}_j}{\partial \hat{t}} + \hat{u}_i \frac{\partial \hat{u}_j}{\partial x_i^*} = - \frac{p_o}{\rho_o U_o^2} \frac{\partial p^*}{\partial x_j^*} + \frac{\nu}{U_o L_{sw}^2} \frac{\partial^2 \hat{u}_j}{\partial x_i^* \partial x_i^*} + \frac{(\rho_{source} - \rho_o) g L_{sw}}{\rho U_o^2} \hat{\theta} \cdot f_j^*$$

Just as before

$$\frac{L_{sw}}{\tau_o U_o} = 1$$

so that the characteristic development time or transient is based on the flow time. Also,

$$\frac{p_o}{\rho_o U_o^2} = 1$$

so that the characteristic pressure is based on the flow pressure. Rewriting results in

$$\frac{\partial \hat{u}_j}{\partial \hat{t}} + \hat{u}_i \frac{\partial \hat{u}_j}{\partial x_i^*} = - \frac{\partial p^*}{\partial x_j^*} + \frac{\nu}{U_o L_{sw}} \frac{\partial^2 \hat{u}_j}{\partial x_i^* \partial x_i^*} + \frac{(\rho_{source} - \rho_o) g L_{sw}}{\rho U_o^2} \hat{\theta} \cdot f_j^* \quad (43)$$

For the salt-water flow scales are available in terms of the source strength for  $U_o$  and

$(\rho_{source} - \rho_o) / \rho_o$ . These expressions are given by Eqn. (24) and Eqn. (26). Substitution

results in

$$\frac{\partial u_j^*}{\partial t^*} + \hat{u}_i \frac{\partial u_j^*}{\partial x_i^*} = - \frac{\partial p^*}{\partial x_i^*} + \frac{\nu}{(\dot{m}_{sw}^*)^{1/3} (g L_{sw})^{1/2} L_{sw}} \frac{\partial^2 u_j^*}{\partial x_i^* \partial x_i^*} + \theta_{sw}^* \cdot f_j^*,$$

or

$$\frac{\partial u_j^*}{\partial t^*} + u_i^* \frac{\partial u_j^*}{\partial x_i^*} = -\frac{\partial p^*}{\partial x_i^*} + \frac{1}{(Gr_{source}^{sw})^{1/3}} \frac{\partial^2 u_j^*}{\partial x_i^* \partial x_i^*} + \theta_{sw}^* \cdot f_j^*, \quad (44)$$

where

$$Gr_{source}^{sw} = \frac{\beta_{sw} \dot{m}_{salt} g L_{sw}^2}{\rho_o \nu^3}. \quad (45)$$

And the scaled variables in terms of the source terms are

$$t_{sw}^* = \frac{t_{sw}}{(\dot{m}_{sw}^*)^{-1/3} (g/L_{sw})^{-1/2}}, \quad u_j^* = \frac{u_j}{(gL_{sw})^{1/2} (\dot{m}_{sw}^*)^{1/3}}, \quad \theta_{sw}^* = \frac{\beta_{sw} Y_{salt}}{(\dot{m}_{sw}^*)^{2/3}},$$

where  $\beta_{sw} = 0.76$ . (46)

### Salt Mass Species Equation:

The mass species equation for the salt-water flow is

$$\rho_o \left( \frac{\partial Y_B}{\partial t} + u_i \frac{\partial Y_B}{\partial x_i} \right) = \rho_o D \frac{\partial^2 Y_B}{\partial x_i \partial x_i} + \dot{w}_B \quad (47)$$

Dimensionless variables defined for the mass species equation are given by

$$\hat{t} = \frac{t_{sw}}{\tau_o}, \quad x_i^* = \frac{x_i}{L_{sw}}, \quad \hat{u}_i = \frac{u_i}{U_o}, \quad w_B^* = \frac{\dot{w}_B L_{sw}^3}{\dot{m}_B}$$

and 
$$\theta_{sw}^* = \frac{\beta_{sw} Y_{salt}}{(\dot{m}_{sw}^*)^{2/3}} \text{ from Eqn. (46)}$$

Substitution results in

$$\left( \frac{(\dot{m}_{sw}^*)^{2/3}}{\beta_{sw}} \right) \left( \frac{\rho_o}{\tau_o} \right) \frac{\partial \theta_{sw}^*}{\partial \hat{t}} + \left( \frac{(\dot{m}_{sw}^*)^{2/3}}{\beta_{sw}} \right) \left( \frac{\rho_o U_o}{L_{sw}} \right) \hat{u}_i \frac{\partial \theta_{sw}^*}{\partial x_i^*} = \left( \frac{\rho_o D}{L_{sw}^2} \right) \left( \frac{(\dot{m}_{sw}^*)^{2/3}}{\beta_{sw}} \right) \frac{\partial^2 Y_B}{\partial x_i^* \partial x_i^*} + \frac{\dot{m}_B}{L_{sw}^3} \dot{w}_B^*.$$

Rearranging terms results in

$$\frac{L_{sw}}{U_o \tau_o} \frac{\partial \hat{\theta}_{sw}}{\partial \hat{t}} + u_i^* \frac{\partial \hat{\theta}_{sw}}{\partial x_i^*} = \left( \frac{\nu}{U_o L_{sw}} \right) \left( \frac{D}{\nu} \right) \frac{\partial^2 \hat{\theta}_{sw}}{\partial x_i^* \partial x_i^*} + \left( \frac{\dot{m}_B}{U_o \rho_o L_{sw}^2} \right) \left( \frac{\beta_{sw}}{(\dot{m}_{sw}^*)^{2/3}} \right) \dot{w}_B^* \quad (48)$$

Just as before the characteristic flow time is represented by setting  $\tau_o = \frac{L_{sw}}{U_o}$  thus making

$$\frac{L_{sw}}{U_o \tau_o} = 1.$$

And the scale for  $U_o$  in Eqn. (26) is substituted into Eqn. (48) yielding

$$\frac{\partial \theta_{sw}^*}{\partial \hat{t}} + u_i^* \frac{\partial \theta_{sw}^*}{\partial x_i^*} = \left( \frac{\nu}{(\dot{m}_{sw}^*)^{1/3} g^{1/2} L_{sw}^{1/2} L_{sw}} \right) \left( \frac{D}{\nu} \right) \frac{\partial^2 \theta_{sw}^*}{\partial x_i^* \partial x_i^*} + \dot{w}_B^*,$$

or

$$\frac{\partial \theta_{sw}^*}{\partial \hat{t}} + u_i^* \frac{\partial \theta_{sw}^*}{\partial x_i^*} = \left( \frac{\nu^3}{\frac{\beta_{sw} \dot{m}_{salt}}{\rho_o g^{1/2} L_{sw}^{5/2}} g^{3/2} L_{sw}^{1/2}} \right) \left( \frac{D}{\nu} \right) \frac{\partial^2 \theta_{sw}^*}{\partial x_i^* \partial x_i^*} + \dot{w}_B^*,$$

or

$$\frac{\partial \theta_{sw}^*}{\partial \hat{t}} + u_i^* \frac{\partial \theta_{sw}^*}{\partial x_i^*} = \left( \frac{1}{(Gr_{source}^{sw})^{1/3} Sc} \right) \frac{\partial^2 \theta_{sw}^*}{\partial x_i^* \partial x_i^*} + \dot{w}_B^*; \quad (49)$$

$Gr_{source}^{sw}$  is defined in Eqn. (45) and

$$Sc = \frac{\nu}{D}. \quad (50)$$

The scaled variables are defined as stated previously in Eqn. (46).

## Chapter 3. Experimental Approach

### 3.1 Experimental Test Facility

The salt-water modeling study was conducted in the Fire Engineering and Thermal Science Laboratory (FETS) at the University of Maryland in College Park, MD. The experimental facility presented in Figure 2 consists of a large capacity fresh-water tank, a scaled room-corridor-room model, a gravity feed delivery system, a 500 mW Argon/Ion laser, focusing optics, a CCD camera fitted with a high pass filter, and an image acquisition computer. The scale model is attached to an aluminum frame for stability and placed in the large fresh-water tank.

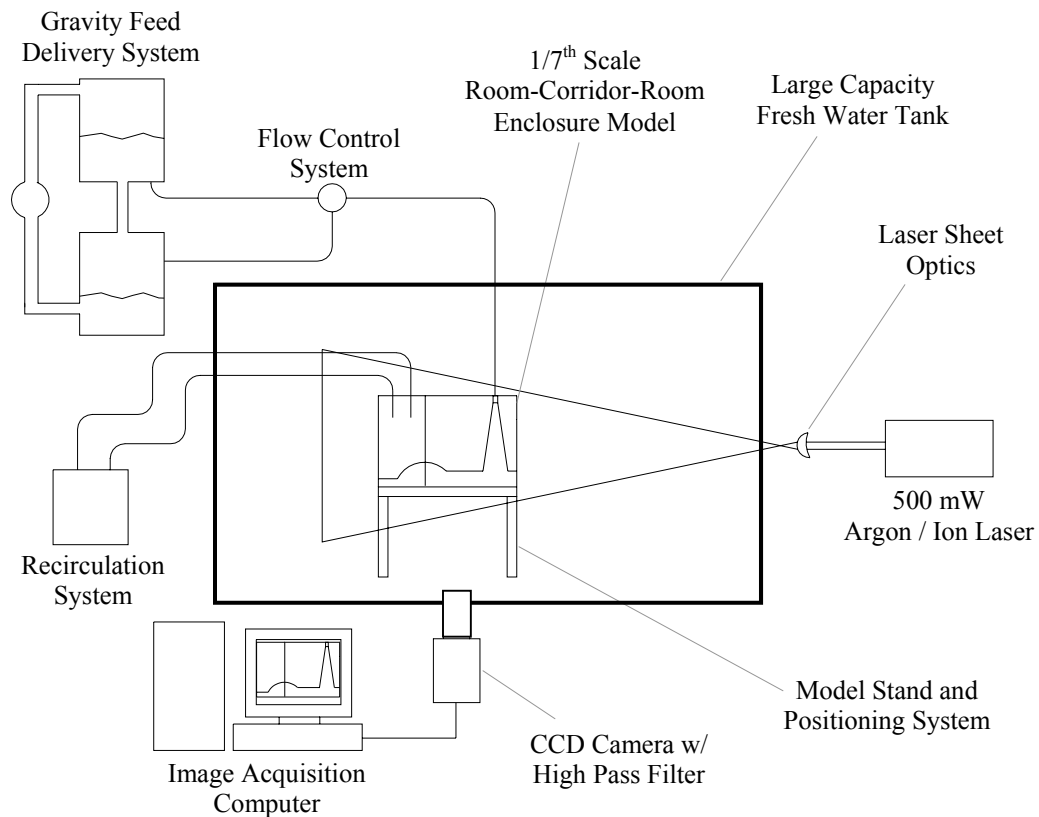


Figure 2: General schematic of the experimental test facility.

The gravity feed delivery system is used to supply salt-water to a tube fixed to the at the source location. A laser sheet is used to illuminate a plane with in the model. The CCD camera records the light distribution from the fluoresced dye within the illuminated plane. The images are stored on an image acquisition computer and compiled for further processing. The following sections describe and illustrate each component of the experimental facility in detail.

### **3.1.1 Gravity Feed System**

The salt-water delivery system used for the current study is detailed in Figures 3 and 4. The delivery system consists of an upper chamber, in which the gravity head is maintained constant, and a lower chamber that serves as an overflow compartment. The chambers are made from plastic cylindrical containers, black painted to reduce photo aging of the Rhodamine dye associated with ambient light exposure. A single in-line pump and a series of PVC pipes connecting the two containers allows the solution to be circulated within the delivery system. The inline pump maintains a constant water level in the upper container thus maintaining the proper gravity head and assures that the salt, water, and Rhodamine dye are in a well-mixed state.

Several PVC valves are used to regulate the direction of the flow for the gravity feed delivery system. For the pump to function properly, the excess air upstream of the pump is removed by attaching a siphoning devise to the release valve (1). Prior to testing the pump is used to increase the circulation through the delivery lines by opening valve (2). Valve (3) is used to regulate the pumps flow from the overflow tank to the gravity head

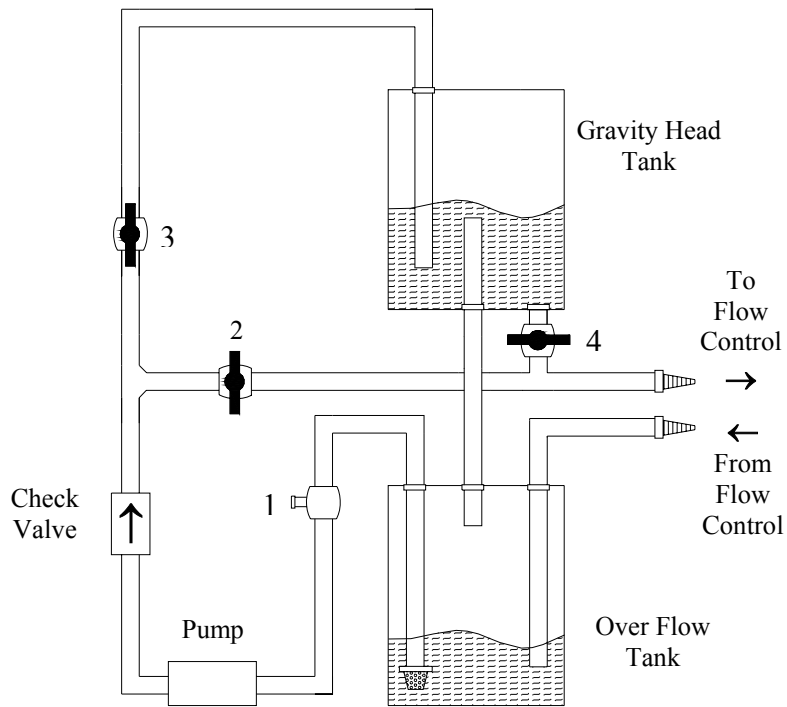


Figure 3: Gravity feed delivery system and control valve setup.

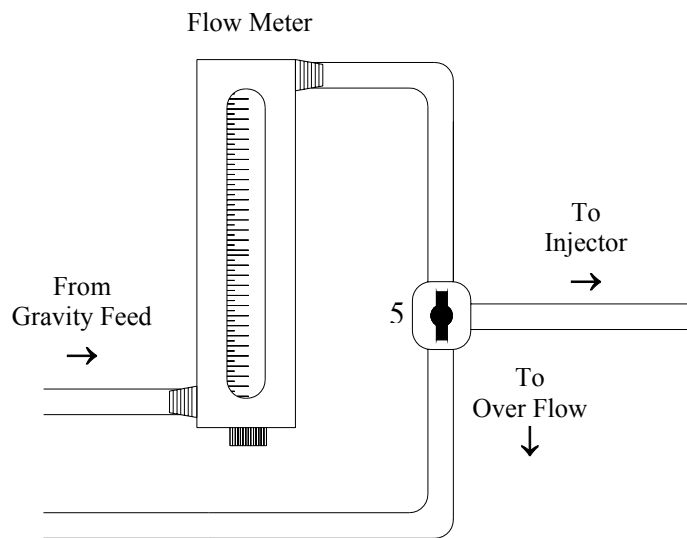


Figure 4: Flow control system and metering device.

tank and is set in the open position during testing. Valve (4) is used to direct the mixed saline solution from the gravity feed tank to the flow control system. The flow control system is presented in Figure 4. Within the flow control system, an inline flow meter is used to adjust and monitor the volumetric delivery rate. Beyond the flow meter a three-way flow valve (5) is used to direct the saline solution to the injector or to the overflow tank for recirculation.

### **3.1.2 Model Description**

A 1/7<sup>th</sup> scale clear polycarbonate model of a room-corridor-room enclosure was constructed for this study. A photograph of the room-corridor-room model is included as Figure 5. The model's dimensions are geometrically scaled to match those of the fire test facility located at Combustion Science and Engineering, Inc. in Columbia, Maryland. The design goals required the model to have walls that are optically transparent, an index of refraction close to that of water, and strong / rigid construction, while also minimizing the wall thickness and associated weight.

A variety of different plastics were analyzed and tested leading to the choice of 1/8<sup>th</sup> inch clear polycarbonate. The particular scale was chosen so that the model could easily be rotated within the large freshwater tank and lifted by a single person. The walls of the model are joined with acrylic cement and the joints are sealed with clear silicone caulk. The walls are reinforced with 1-inch plastic braces in order to prevent separation and increase rigidity. A series of cross members beneath the floor of the model were implemented in the design for added structural stability.

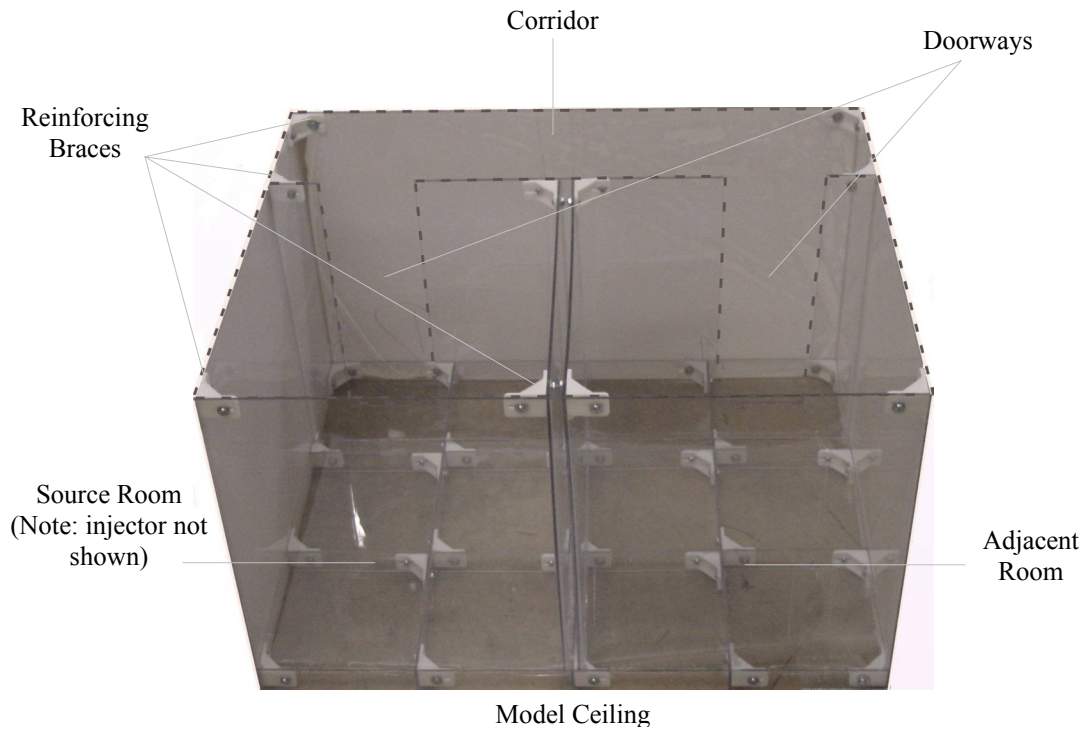


Figure 5: Photograph of 1/7<sup>th</sup> scale room-corridor-room enclosure model. Dashed lines are added to better illustrate boundary walls.

### 3.1.3 Injection System

The saline solution is introduced into the model by means of an adjustable injection system, which is depicted in Figure 6. The system consists of a stainless steel tube with a 5.6 mm internal diameter, fitted with a Teflon elbow connector attaching the injector to a delivery line from the flow control. The stainless steel tube is set in place with an adjustable Teflon compression fitting allowing easy vertical positioning of the injector. The compression fitting is mounted to a 1/8<sup>th</sup> inch sheet of clear acrylic that is attached to the model in the source room.

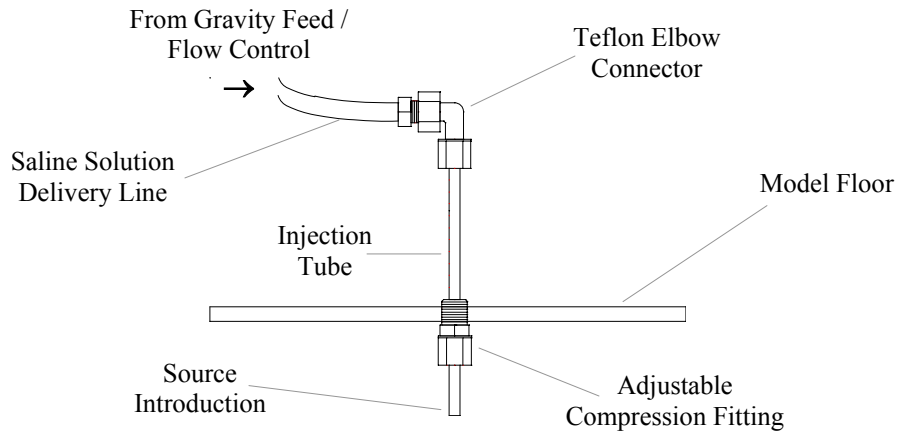


Figure 6: Saline solution injection system mounted to enclosure model

### 3.1.4 Recirculation System

Several experiments are conducted for a single planar view within the geometry and the results are compared with one another. Thus, it is of great importance to be able to conduct the experiments without disturbing the position of the camera and the model. Steps were taken to eliminate movement so that the various conditions can be properly compared and scaled. The first of which is a recirculation system. The system is used to remove the injected saline solution from the model enclosure after each test is run without compromising the enclosures position with respect to the camera.

A series of tubes are placed in the enclosure and are used to send clean water into the model while at the same time removing the old water. Thus, allowing the majority of the dye that accumulated from the prior test to be circulated out. The in flow of clean water is pressurized from a faucet adjacent to the large tank and directed through a high flow inline filter and through flexible tubing that is fastened to the tanks frame. The outflow of

“dirty” water is gravity driven; the flow rate is controlled by an adjustable PVC valve and directed into a sink adjacent to the large tank. It is important to note that the water level within the enclosure must remain slightly above that of the surrounding water in the large tank to prevent the model from floating. Thus, the outflow valve must be monitored and adjusted accordingly to maintain a constant water level. The water within the enclosure is circulated until the presence of fluorescent dye is no longer visible.

### **3.1.5 Positioning System**

A positioning system illustrated in Figure 7 has been implemented in the experimental setup in order to further restrict the movement of the model enclosure between experiments. The entire system is constructed of Bosh aluminum framing. The model rests on a stand fixed with two triangular aluminum plates that serve to stabilize the enclosure and prevent any shifting with respect to the stand. The stand is connected to a cross member that is mounted to the top of the large tank. The cross member is used for positioning and to stabilize the frame itself. Additional support and weight is added to the frame by means of cinder block stands located beneath the model. Cinder blocks are placed on the cinder block stands after the positioning of the frame is set.

### **3.1.6 Optics**

A 500-mW Argon Ion CW laser and a series of laser optics, illustrated in Figure 8, is used to create the planar light sheet for the PLIF diagnostics. The laser is mounted to a stand built with Bosh aluminum framing and the entire system is bolted to an optics table. The initial beam is passed through a spatial filter and collimated with a dual convex lens.

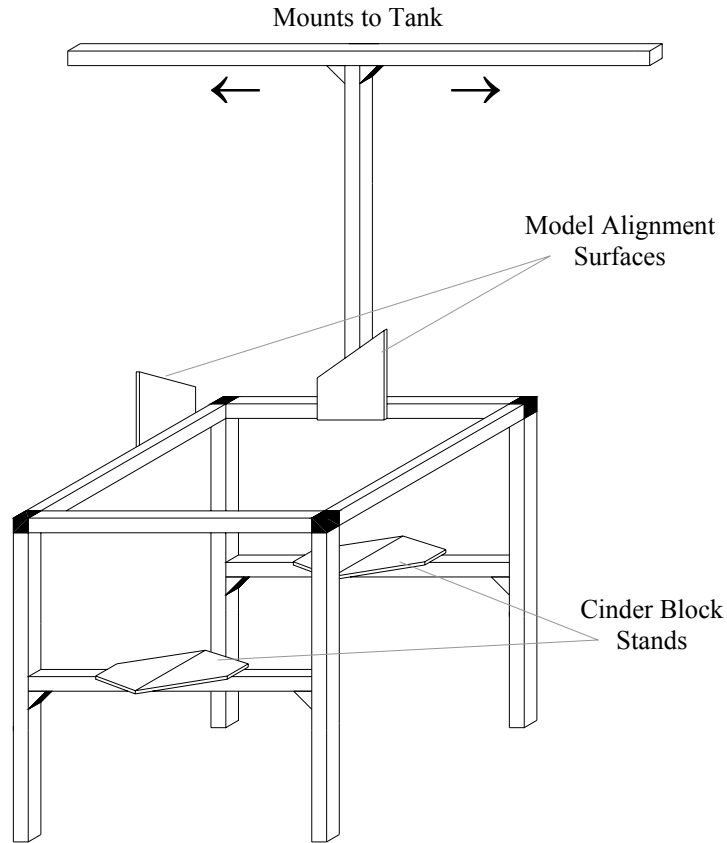


Figure 7: Model stand and positioning system.

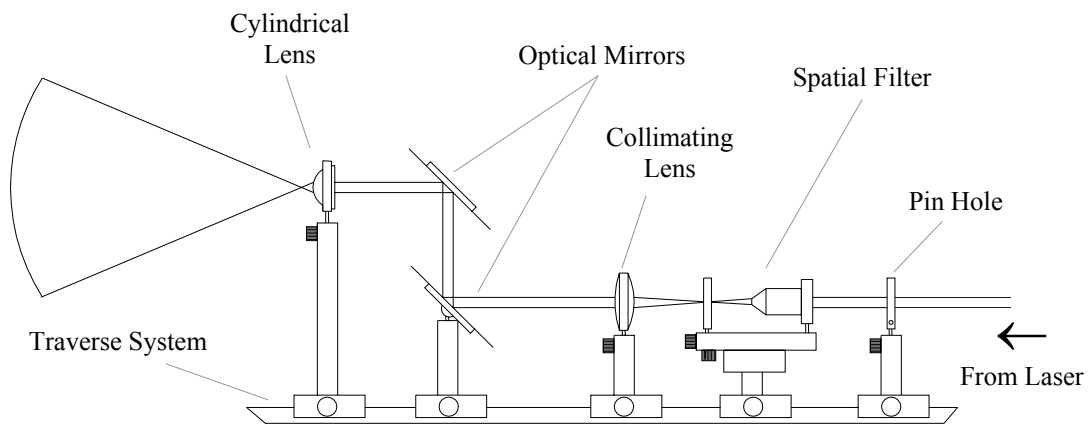


Figure 8: Optical set up used to generate and position planar laser sheet.

The spatial filter is used to produce a “clean” light sheet. The PLIF technique requires a light sheet with a well-defined intensity profile. The argon-ion laser produces a Gaussian light intensity profile. However, imperfections in optics result in spatial deviations from this profile as shown in Figure 9. A spatial filter is used to remove imperfections in the beam intensity profile. The spatial filter is composed of a microscopic objective and a high intensity pinhole, both of which are aligned using a micro-traverse system. The microscopic objective focuses the beam down to a point, in which it is passed through the pinhole to remove spatial noise.

After the spatial filter and collimating lens, the beam is then redirected by a series of optical mirrors. Finally, the collimated beam is passed through a cylindrical lens that refocuses the light into a vertical planar sheet. The position of the cylindrical lens is adjusted based on the spatial requirements of the light sheet.

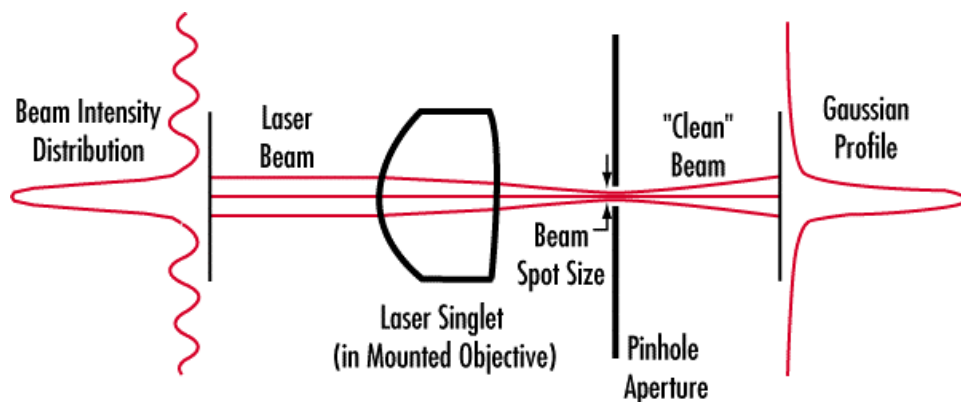


Figure 9: Optical description of spatial filter and beam profile

### **3.1.7 Image Acquisition**

A Cohu 8-bit (NTSC) CCD camera is used for digital still imaging within this study. The camera captures interlaced images with 480 by 752 lines of resolution. An adjustable optical zoom lens is mounted to the camera. The lens is fitted with a 550 nm high pass filter to restrict all wavelengths of light outside the range of the dyes fluorescence wavelength. The camera is linked to a data acquisition computer through a image grabber board. Image grabbing software is used to store the initial images to the computers hard drive.

## **3.2 Quantitative Methodology**

Prior to this study, the salt-water test facility was used for qualitative analysis and has since been retrofitted to allow for laser diagnostics and quantitative analysis of an enclosure model configuration. Many experimental configuration and testing methodology considerations had to be carefully evaluated during this transition. Several new experimental methods had to be established to obtain quantitative data from the salt water-modeling technique.

### **3.2.1 Injection Consideration**

In order to properly model the fire behavior, the salt-water injection must provide buoyancy dominated turbulent plume behavior very near the source. The injector geometry and injection flow rates were adjusted to meet this requirement. The absorption characteristics of the dye also places limits on the maximum plume width and the maximum injection diameter. These considerations are discussed at length in § 3.2.2. For

the current study flow rates of 50, 100, 150 and 200 ml/min. were delivered to a 5.6 mm diameter injector. These injector conditions provide analogous behavior and were within the limits of our experimental constants.

The salt-water source is initially momentum dominated because the saline solution is introduced as a jet. The initial jet-like behavior of the salt-water source differs from the immediate buoyancy dominated behavior near the source in an accidental fire. The initial momentum of the salt-water jet must be minimized to maintain analogous behavior between the salt-water and fire flows. The initial velocity disturbs the validity of the salt-water analogue close to the source. The initial momentum of the salt-water plume is unimportant at a distance far from the source in which buoyancy dominates the flow dynamics.<sup>19</sup> This distance is characterized by the Morton length scale

$$\frac{l_M}{d} = \left( \frac{\pi}{4} \right)^{1/4} \left( \frac{\rho_o u_{inj}^2}{(gd|\rho_{inj} - \rho_o|)} \right)^{1/2}$$

where  $d$  is the diameter of the source,  $g$  is acceleration due to gravity,  $l_M$  is the Morton length scale and  $u_{inj}$  is the injection velocity. For the current study, the Morton length scale is used to determine the flow conditions necessary to produce a buoyancy dominated plume. The momentum effects are considered insignificant and the plume becomes buoyancy dominated at a distance above the source equal to  $L_{plume}$  or  $5 \times l_M$ . Morton length scales and buoyancy dominated flow criterion are presented in Table 1 for the experimental flow conditions. It should be noted that plume like behavior is achieved within 20% of the enclosure height for all flow conditions.

Table 1: Morton length scale results for salt-water model inlet conditions; ( $Y_{salt} = 0.10$ )

Flow Rate (ml/min)	$l_m$ (mm)	$L_{plume}$ (mm)	% of Model Height
50.0	2.8	13.8	4.5
100.0	5.5	27.5	9.0
150.0	8.3	41.3	13.5
200.0	11.0	55.0	18.1

The salt-water flow is only analogous to the fire flow in the turbulent regime. It is therefore essential for turbulent conditions to be established early in the flow field, i.e. near the source. A critical Reynolds number criterion for turbulence dominated flow based on the compartment height and the buoyancy induced convective velocity scale has been specified by other investigators.<sup>8,16</sup> The current investigation requires that turbulent transition occurs close to the source.

A source based Grashof number, provided in Eqn. (45), is calculated using the plume dominated length scale,  $L_{plume}$ , which should be very near the source. Previous investigators determined that turbulent transition occurs when  $Gr_{source}^{sw} > 1.5 \times 10^7$ .<sup>35</sup> In this investigation, the flow is assumed to be turbulence dominated when  $Gr_{source}^{sw} > 1.5 \times 10^7$  based on the plume dominated length scale  $L_{plume}$ . Criteria for turbulence-dominated flow based on critical Reynolds and Grashof numbers are provided in Table 2.

Table 2: Important dimensionless turbulence criterion; ( $Y_{salt} = 0.10$ )

Flow Rate (ml/min)	$Gr_{source}^{sw}$	$Re$
50.0	1.3E+08	3.4E+03
100.0	1.0E+09	3.9E+03
150.0	3.4E+09	4.6E+03
200.0	8.1E+09	4.7E+03

For the flows examined in this study, the critical Grashof number is achieved with the exception of 50 ml/min. Preliminary results demonstrated a significant discrepancy in the scaling for this flow (50 ml/min.). Therefore, this flow was not used in the final analysis presented in this investigation. However, all of the flows examined fall short of the critical Reynolds number requirement specified by other investigators. Based on the turbulent transition arguments, which are the basis of the critical Grashof number used in this investigation, the critical Reynolds number recommended by previous investigators may be overly conservative.<sup>35</sup>

### 3.2.2 PLIF Requirements

In order to obtain quantitative data within the spatial domain of interest it is necessary that the requirements of the technique be strictly followed. Light absorption is an important characteristic of all fluorescent dyes. It is a function of the dye concentration and the path length of the incident light. At high dye concentrations the excited dye begins to self absorb the incident light along the beam path length. The images recorded in this study are only representative of quantitative data within the spatial domain where

light absorption does not affect the linear response of the dye. A critical path length has been established for each planar sheet based on the light absorption properties inherent with Rhodamine 6G dye.

Chandrasekar and Walker demonstrate that for a fluorescent dye at any arbitrary concentration, the absorption of light for a beam path  $z$  can be computed by

$$dI_e(z) = -\varepsilon \cdot C(z) \cdot I_e(z) dz \quad (51)$$

where  $I_e$  is the excitation intensity,  $\varepsilon$  is the extinction coefficient, and  $C$  is the dye concentration.<sup>35,37</sup> Guilbault and Arcoumanis suggest that the linear response of the fluorescent dye is only valid when less than 5% of the excited light is absorbed.<sup>38,39</sup>

Assuming the concentration is constant along the path length, neglecting the attenuation along the receiving path and assuming that  $I_e$  is known at a critical value for  $z$ . Then Eqn. (51) can be solved for a critical path length

$$\int_{I_1}^{I_2} \left( \frac{1}{I_e} \right) dI_e = -\varepsilon C \int_0^b dz \quad (52)$$

$$b(C) = \frac{\ln(I_2/I_1)}{-\varepsilon \cdot C} = \frac{\ln(0.95)}{-\varepsilon \cdot C} \quad (53)$$

where  $I_1$  is the maximum excitation intensity,  $I_2$  is the excitation intensity with absorption, and  $b$  is the critical beam path length occurring at 95% excited light fluorescence. The critical path length in which the dye excitation maintains a linear relationship with concentration is presented in Figure 10 as a function of the concentration of dye. The linearity of the dye's fluorescence allows quantitative

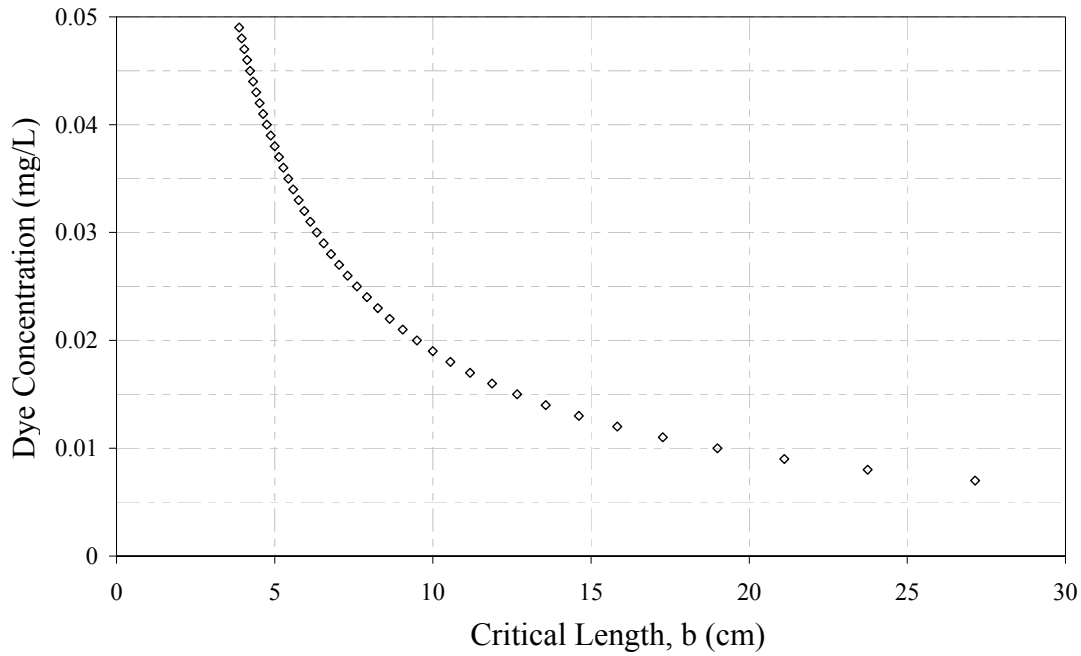


Figure 10: Maximum incident path length for which Rhodamine 6G fluorescent dye maintains linear emission characteristics.

measurements to be obtained; Eqn. (53) is used to control the spatial domain in which the measurements are valid.

The concentration of Rhodamine 6G dye used in this study was chosen based on the light absorption properties of the dye. An optimum dye concentration was computed for each planar view, to produce the highest light emission signal possible while staying within the linearity regime for the fluorescent dye.

It has also been observed by previous researchers that residual chlorine reacts with the fluorescent dye used in this study (Rhodamine 6G). The reaction causes a significant decay in the dye concentration. Additives and filtration are used to treat the dyed saline solution based on the Davidson's recommendations.<sup>40</sup>

### 3.2.3 Optimizing Image Quality

The limitations of the fluorescent dye restrict the use of high dye concentrations, so it is necessary to adjust the camera settings to improve the image depth. The depth of the captured image is descriptive of the amplitude between the minimum and maximum gray level captured by the camera. A comparison of the minimum and maximum gain settings on the camera is presented in Figure 11, which illustrates the light distribution within a uniformly mixed volume; refer to § 3.2.4. As the image depth of the camera is increased the magnitude of the fluctuations in the gray level increase as well. However, the fluctuations are relatively the same with respect to the maximum gray level value. Furthermore, when both intensity profiles are normalized by the maximum gray level value, they are virtually identical as seen in Figure 12. Therefore, increasing the gain increases the depth of the image without affecting the shape of the normalized signal.

By increasing the gain on the CCD camera, the amount of digital noise (salt & pepper) within the image is also increased; however the signal to noise ratio remains nearly the same. The signal to noise ratio is of great importance when performing any type of data imaging. To reduce the amount of digital noise, multiple images are taken over a given short time interval for transient experiments. Existing literature on PLIF techniques supports the use of time-averaging images to reduce noise levels without reducing the overall mean intensity level of the image. An optimization of the time-averaging period (~1 second, 30 images) has been previously examined for similar flow conditions found in gravity currents. For the current study this technique was employed and an optimal

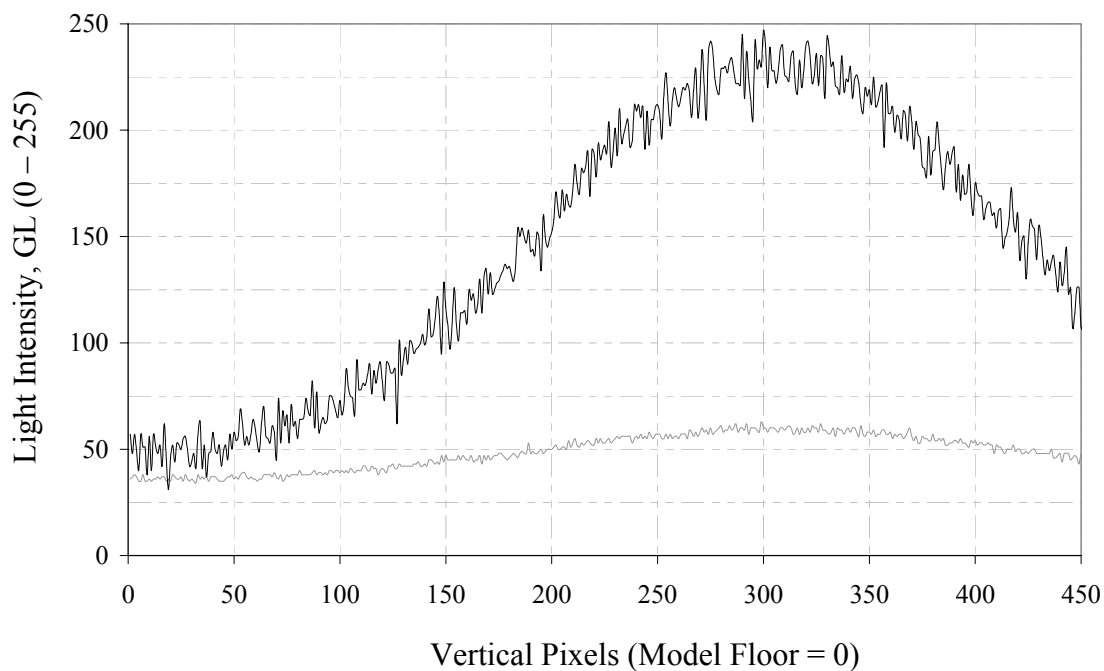


Figure 11: Light intensity profile with the camera's gain set to zero (—) and with a maximum gain setting (—).

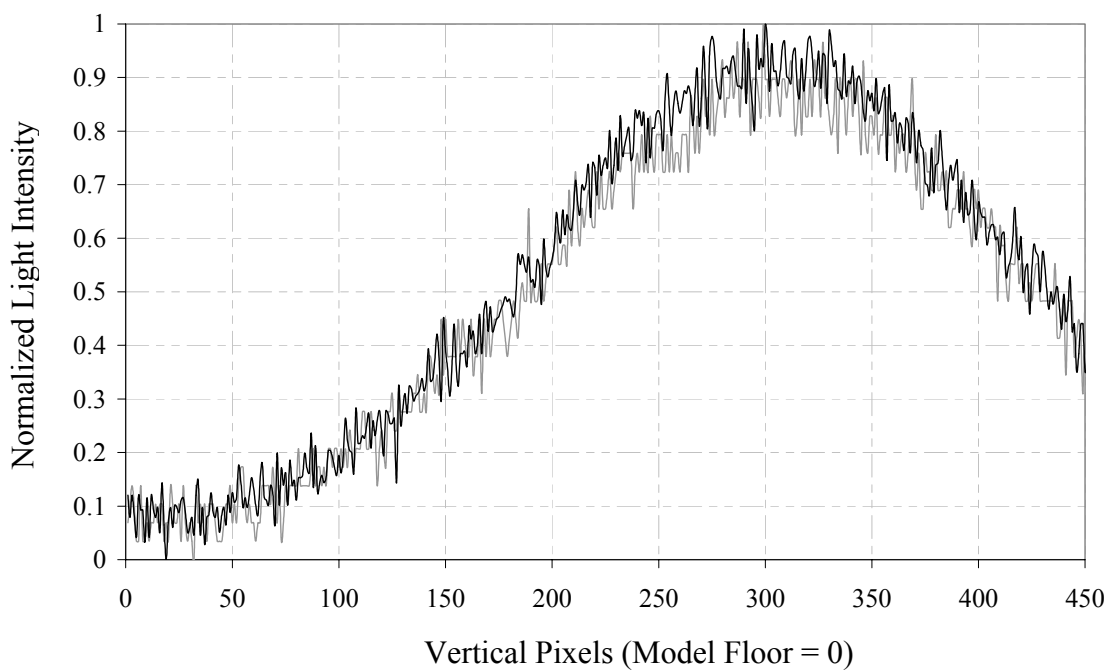


Figure 12: Normalized light intensity profile with the camera's gain set to zero (—) and with a maximum gain setting (—).

time-averaging period was obtained and applied to all images (~1/15 second, 4 images). It is important to note that the flows evaluated in this work are slow moving relative to the speed of the data acquisition systems buffer memory and that the digital noise associated with the gain of the CCD camera is random. With this in mind the consecutive images are viewed as a single time step. Averaging the consecutive images reduces the random digital noise while the intensity of the signal remains unchanged. Preliminary testing has been conducted to demonstrate that the flows are “frozen” within the sampling period used in this study. A macro was written within the image acquisition software to take two consecutive interlaced images that are 1/15<sup>th</sup> of a second apart and store them in the buffer memory of the computer. The images are saved to the hard disk and the procedure is repeated for each time step.

The images captured by the CCD camera are interlaced images with a resolution of 480 by 752 pixels. NTSC and PAL video images (US and European standards) are made up of two (2) interlaced fields. The horizontal lines of the image are broken into odd and even fields. Each field is captured over a period of 1/60<sup>th</sup> of a second resulting in a total image exposure time of 1/30<sup>th</sup> of a second. As described previously, the slow moving flows examined with in this study are considered frozen within this exposure time. An international data language (IDL) program is written to separate the odd and even fields of the interlaced image. The 240 odd and 240 even fields are stretched to represent two images each with 480 horizontal lines. Finally, an average is taken of the odd and even images. Incorporating this procedure with the time-averaging technique allows a single

time step to be represented by an average of four digital images. Thus, greatly increasing the images signal to noise ratio.

Sources of error are presented by the digital noise linked with the cameras gain as well as the background noise associated with the laser sheet interacting with the enclosure walls. The background noise can be greatly reduced by taking a series of background images prior to each experiment. After the experimental setup is complete, a series of 300 instantaneous images are taken with the laser sheet illuminating the selected slice within the room. The laser sheet reflects off of surfaces to create background noise. The CCD cameras high pass filter removes most of the noise, however the silicone caulk and the enclosures walls have trace amounts of dye present and the sheet illuminates the boundaries at the same wavelength as the fluoresced dye. The subtle noise associated with the boundaries is quantitatively measured by averaging these images. This average background image is subtracted from the instantaneous experimental images in post-processing.

### **3.2.4 Light Sheet Distribution**

Because of the Gaussian light intensity distribution, the vertical location of the light sheet is of great significance. It is important that the sheet is introduced in such a manner that the area of most interest is adequately illuminated, while at the same time providing adequate illumination through out the entire domain of interest. Preliminary tests have been conducted to locate the optimal light sheet dimensions and position, for each plane of interest with in the room-corridor-room model.

While using PLIF diagnostics it is important to understand that the light emitted by the excited dye is a function of the concentration of the dye and the intensity of the incident laser light, refer to Eqn. (51). Since the light sheet produced from the Argon/Ion laser has a Gaussian intensity profile, the experimental images not only describe the concentration distribution of the dye but also the incident light intensity distribution. Only the dye / salt dispersion is of interest so the effect of the light sheet distribution must be removed.

Previous studies provide details regarding calibration techniques for a non-uniform light distribution.<sup>13</sup> Calibration images are taken as a quantitative measurement of the light intensity distribution within the enclosure and are used in post-processing to correct the experimental images. For each test setup an average calibration image is needed due to the geometric differences within the enclosure and the variances associated with adjusting the corresponding light sheet. Calibration images are taken following a series of experiments, with the model location unchanged. The model is filled with a known dye concentration (0.01 mg/L), the laser sheet is activated, and a series of 300 instantaneous images are taken and used to create a single average calibration image. The averaged image represents the light sheet distribution within the spatial domain of the enclosure and is used in converting the captured light intensity to a salt mass fraction.

### **3.2.5 Converting Light Intensity Measurements to Salt Mass Fraction, $Y_{salt}$**

Testing in this study and elsewhere has demonstrated that the relationship between the fluoresced light intensity is purely a function of the dye concentration.<sup>37,38,40</sup> This relationship can be described by

$$I = C_1[DYE] \quad (54)$$

where  $I$  is the normalized light intensity (gray level) recorded by the camera,  $C_1$  is a factor that includes the salt mass fraction, and  $[DYE]$  is the dye mass concentration. The constant  $C_1$  is determined by a series of calibration images with known concentrations of dye. The normalized intensity is measured for these images and the constant  $C_1$  is determined from a linear curve fit of normalized intensity as a function of dye concentration. Assuming that the concentration of dye and salt dilute similarly (as discussed in § 1.1), the dye concentration  $[DYE]$  is related to the salt concentration  $[SALT]$  by

$$[DYE] = C_2[SALT] \quad (55)$$

$C_2$  is determined by the initial salt and dye concentrations at injection. The salt mass concentration can be expressed in terms of the salt mass fraction as follows:

$$[SALT] = \frac{m_{salt}}{V_{sw}} \frac{\rho_{sw}}{\rho_{sw}} = Y_{salt} \rho_{sw} \quad (56)$$

Furthermore, an expression for the salt-water density in terms of the salt mass fraction can be determined empirically. The density is given by

$$\rho_{sw} = C_3 + C_4 Y_{salt} \quad (57)$$

where  $C_3$  is the density of fresh water ( $= 1000 \text{ kg/m}^3$ ) and  $C_4$  is the constant relating the salt mass fraction within a salt-water solution to the solutions density ( $= 760 \text{ kg/m}^3$ ).

Combining Eqns. (54) and (55)

$$I = C_1 C_2 [SALT] \quad (58)$$

Combining equations (56) and (58)

$$I = C_1 C_2 Y_{salt} \rho_{sw}. \quad (59)$$

Combining Eqns. (57) and (59) results in the final expression relating the fluorescence intensity to salt mass fraction;

$$I = C_1 C_2 Y_{salt} (C_3 + C_4 Y_{salt}). \quad (60)$$

A characteristic plot of this relationship is provided in Figure 13. The mass fraction is determined from the measured intensity using the quadratic equation shown in Eqn. (60).

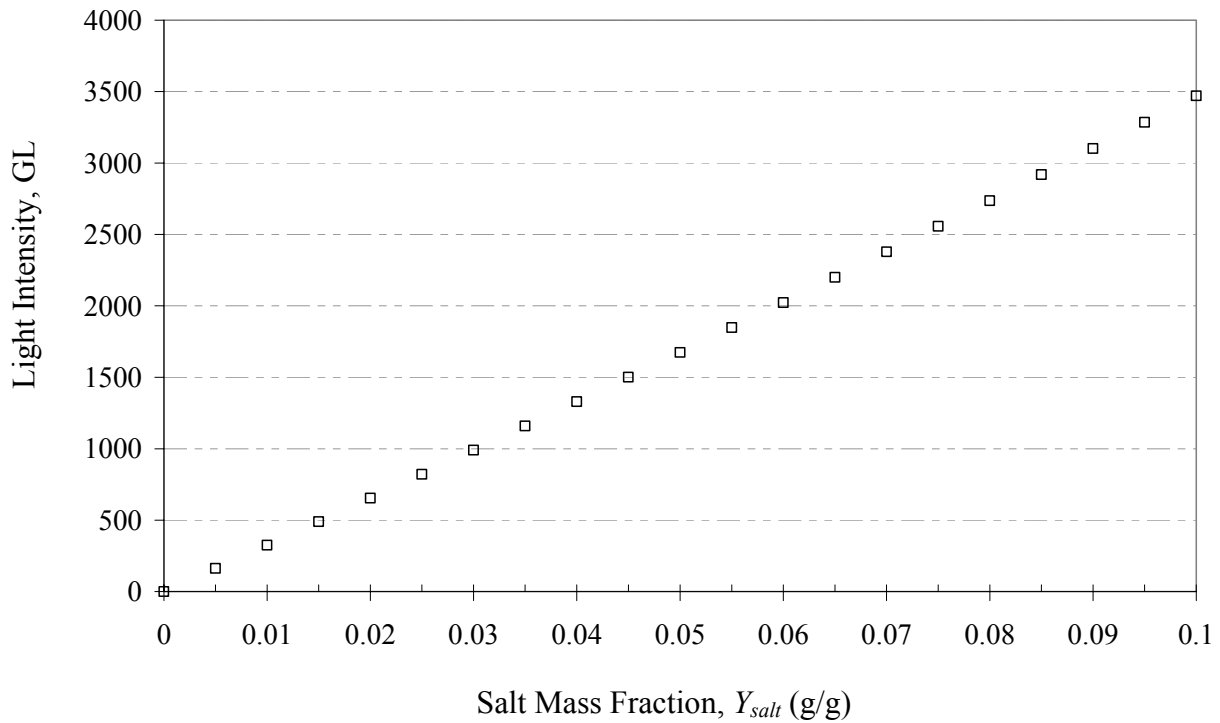


Figure 13: Second-order polynomial relating gray level to salt mass

### **3.3 Experimental Procedure**

The experimental procedure within this study follows a detailed methodology in order to produce dependable and precise measurements. A checklist has been created to ensure consistency, adequate documentation of the experiments and recording necessary measurements. The checklist is provided in Appendix A. For each planar view the positioning system, optics and the relative locations of the frame and injector are tested and recorded. Along with the spatial considerations of the experimental setup, several other important parameters are recorded using the checklist with regard to the diagnostics and other experimental variables. Detailed descriptions of the experimental procedure used for this study are included in Appendix B.

## Chapter 4. Analysis

### 4.1 Calculating Dimensionless Parameters for Fire Test Data

The salt-water analogue requires the fire experimental results to be presented in terms of dimensionless variables describing the dispersion within the enclosure. These variables are computed from experimental data obtained from the full-scale fire experiment. The following section provides an overview of the important variables and parameters for the fire experiment and the basic computations of each dimensionless quantity. For a detailed description of the derivation and scaling of governing equations for the full-scale fire refer to Chapter 2. The scaled parameters from the fire experiment are used to convert the local measurements at each of the five detectors in the room-corridor-room experiment into dimensionless quantities that describe the dispersion dynamics. The local gas temperatures shown in Figure 14 were converted into a dimensionless thermal dispersion signature as shown in Figure 15 for comparison with the salt-water results. The local smoke mass fraction measurements for the five detectors shown in Figure 16 were converted to the dimensionless smoke dispersion signatures as shown in Figure 17 for an analogous comparison with the salt-water results. The smoke and the thermal dispersion signatures are plotted against the dimensionless time for the same conditions in the previous smoke mass fraction and temperature time trace. A detailed examination of the dispersion signatures for the fire and salt-water experiments is presented in Chapter 5. Through this comparison the salt-water experiments are used to model the conditions of interest within the full-scale fire experiment. The computations necessary for this evaluation are described within this chapter for both the full-scale fire and salt-water model experimental results.

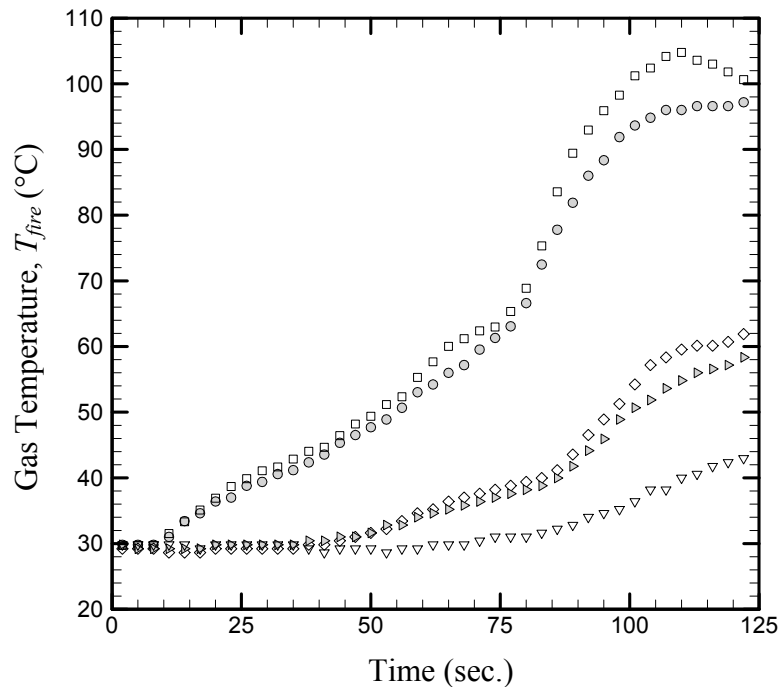


Figure 14: Local  $T_{fire}$  at detector for full-scale fire experiment:  
 $\square$  RM1 - C,  $\bullet$  RM1 - S,  $\diamond$  COR - C,  $\blacktriangleright$  COR - S,  $\nabla$  RM2 - C

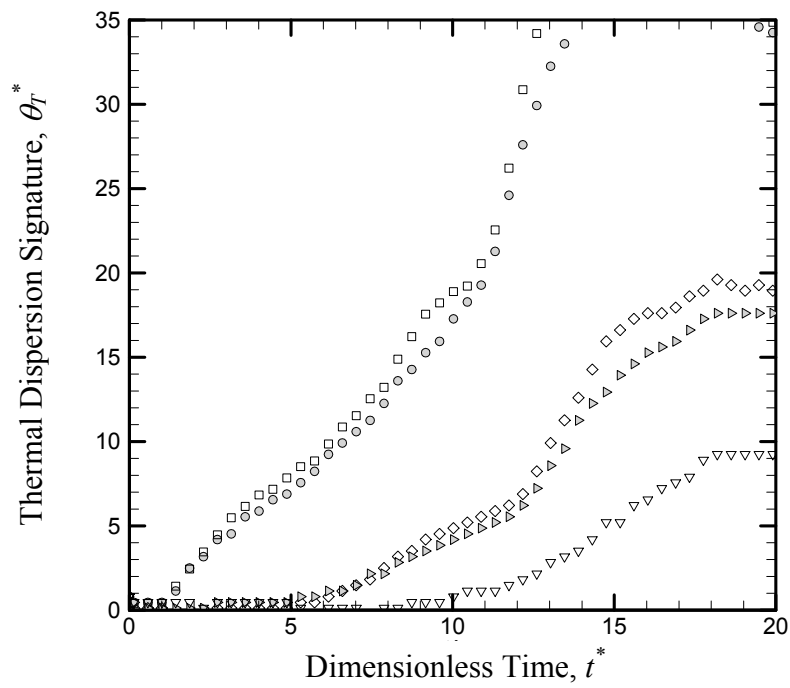


Figure 15: Local  $\theta_r^*$  at detector for full-scale fire experiment:  
 $\square$  RM1 - C,  $\bullet$  RM1 - S,  $\diamond$  COR - C,  $\blacktriangleright$  COR - S,  $\nabla$  RM2 - C

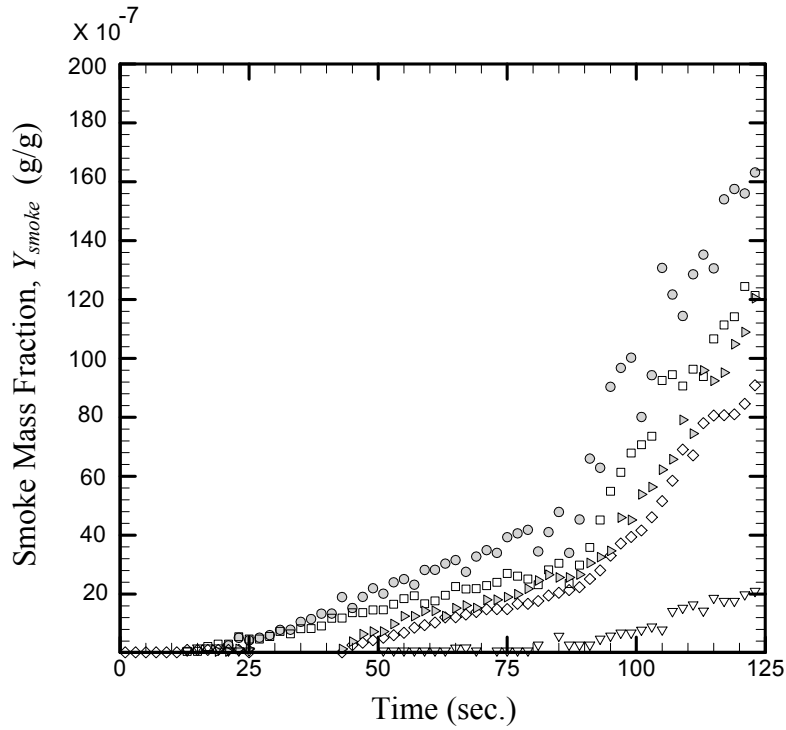


Figure 16: Local  $Y_{smoke}$  at detector for full-scale fire experiment:  
 □ RM1 - C, ● RM1 - S, ◇ COR - C, ► COR - S, ▽ RM2 - C

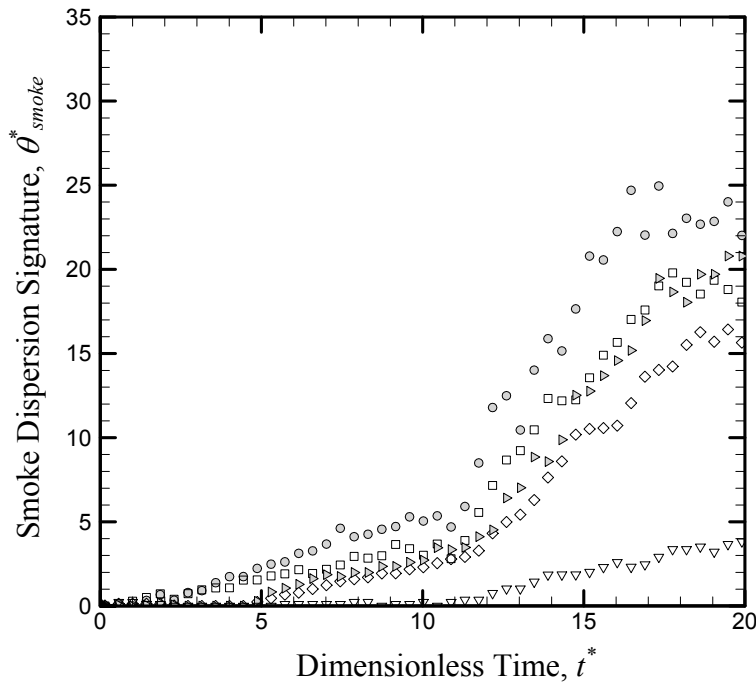


Figure 17: Local  $\theta_{smoke}^*$  at detector for full-scale fire experiment:  
 □ RM1 - C, ● RM1 - S, ◇ COR - C, ► COR - S, ▽ RM2 - C

#### 4.1.1 Dimensionless Energy Release Rate, $Q^*$

The scaling performed in § 2.1.2 presents the density deficit of the thermal plume in terms of a non-dimensional heat source strength term  $Q^*$ . This dimensionless parameter describing the source strength takes the form

$$Q^* = \left( \frac{Q}{\rho_o c_p T_o g^{1/2} L_f^{5/2}} \right),$$

where  $\rho_o$  is the density of air,  $c_p$  is the specific heat capacity of air,  $T_o$  is the ambient air temperature,  $L_f$  is the enclosure height and  $Q$  is the energy release rate of the fire.

The energy release rate,  $Q$ , for the full-scale fire test data is calculated based on the fuel type, geometry, and measured mass loss rate in which

$$Q = \chi \cdot \dot{m}'' \cdot A_f \cdot \Delta H_c$$

where  $\chi$  is the combustion efficiency factor ( $< 1.0$ ),  $\dot{m}''$  is the mass loss rate of the fuel per unit area,  $A_f$  is the fuel surface area, and  $\Delta H_c$  is the heat of combustion.<sup>2</sup> Literature values were chosen for the  $\chi$  factor and the  $\Delta H_c$  for the respective fuel mixture, (75% heptane and 25% toluene). A load cell was used to monitor the mass of fuel within the full-scale experiment. A constant mass loss rate,

$$\dot{m}_{fuel} = \dot{m}'' \cdot A_f$$

was computed based on a linear fit of the load cell data for the burning duration of the fuel.

#### 4.1.2 Dimensionless Fire Time, $t_{fire}^*$

The non-dimensional time for the full-scale fire experiment is derived in § 2.2.1 and presented in terms of the source strength in which

$$t_{fire}^* = \frac{t_{fire}}{(Q^*)^{-1/3} (L_f / g)^{1/2}}$$

where  $t_{fire}$  is the experimental (real) time and  $t_{fire}^*$  is the dimensionless time for the full-scale fire. The dimensionless time can be computed for any experimental time given a dimensionless fire source strength,  $Q^*$ , and an enclosure height,  $L_f$ .

#### 4.1.3 Dimensionless Thermal Dispersion Signature, $\theta_T^*$

The buoyancy force that moves smoke in a fire is due to a density deficit resulting from a temperature difference between the hot gasses and the cool ambient surroundings. A non-dimensional thermal dispersion term,  $\theta_T^*$ , can be used to describe this important parameter as previously defined in Eqn (31):

$$\theta_T^* = \frac{\beta_T (T - T_o)}{(Q^*)^{2/3}}$$

$$\text{where } \beta_T = \frac{1}{T_o},$$

where  $T$  is the buoyant gas temperature and  $T_o$  is the ambient air temperature. The local gas temperatures at each detector are thus converted into thermal dispersion signatures based on the dimensionless source strength.

#### 4.1.4 Converting Optical Measurements to Smoke Mass Fraction, $Y_{smoke}$

The full-scale fire experiment monitored the light obscuration at the local position of each of the five detectors. A laser beam and photodiode assembly were mounted 5 cm in front of each detector, to monitor the obscuration prior to entrance. The optical density of smoke is calculated based on the measured attenuation of the beam of light passing through the smoke. If the initial light intensity of the beam is  $I_o$  when there is no smoke present, then the reduced intensity ( $I$ ) is given by the Lambert-Beer Law:<sup>2</sup>

$$I = I_o \exp(-\kappa CL) \quad (61)$$

where  $C$  is the mass concentration of smoke particles,  $L$  is the optical path length of the beam and  $\kappa$  is the extinction coefficient. The optical density,  $D$ , is then defined in terms of natural logarithms given by:<sup>41</sup>

$$D = -\log\left(\frac{I}{I_o}\right) = \kappa CL$$

This expression can be rearranged to represent the mass concentration of smoke in terms of the extinction coefficient, the optical path length and light attenuation yielding

$$C = -\left(\frac{1}{\kappa L}\right) \cdot \log\left(\frac{I}{I_o}\right)$$

A baseline light intensity is measured and averaged over a two-minute interval prior to each test and is used within the calculations as the respective  $I_o$  for each detector location. The path length of 18 inches (0.4572 m) is maintained for the optical set up at each location. Literature supports the assumption that  $\kappa$  is nearly universal and remains constant for post-flame smoke produced in over-ventilated fires. The constant value used for the mass specific extinction coefficient for post-flame generated smoke is  $8.7 \text{ m}^2/\text{g}$

with a 95% confidence interval of 1.1 m<sup>2</sup>/g. The calculated value of the mass concentration of smoke particles,  $C$ , can also be viewed as a smoke density,  $\rho_{smoke}$ . The smoke density is used to calculate the mass fraction of smoke given by

$$Y_{smoke} = \frac{\rho_{smoke}}{\rho_{mix}}$$

Where  $\rho_{mix}$  is the density of the smoke and air mixture. It is assumed that the amount of air is much larger than the amount of smoke particles. Thus,  $\rho_{mix}$  is found using the properties of air and the ideal gas law for the local gas temperature. The mass fraction of smoke is also used to define a dispersion variable similar to  $\theta_T^*$  and  $\theta_{sw}^*$ .

#### 4.1.5 Dimensionless Smoke Dispersion Signature, $\theta_{smoke}^*$

Dimensional analysis of the fundamental equations allows the mass fraction of smoke to be presented in terms of a non-dimensional value (refer to Eqn. 40)

$$\theta_{smoke}^* = \frac{Y_{smoke}}{(Q^*)^{2/3} \left( \frac{c_p T_o (y_{smoke})}{\Delta H_c} \right)}$$

where  $\theta_{smoke}^*$  is a smoke dispersion parameter,  $Y_{smoke}$  is the mass fraction of the smoke at a specific location, and  $y_{smoke}$  is the smoke yield defined as the mass of smoke generated at the source per unit mass of fuel consumed. The  $\theta_{smoke}^*$  variable incorporates the driving force of the fire in terms of a non-dimensional energy release rate,  $Q^*$ , as well as the fuel specific smoke yield. Thus, the smoke dispersion parameter is sensitive to the source strength and the fuel type.

## 4.2 Calculating Dimensionless Parameters for Salt-Water Model

In an analogous representation of the dispersion dynamics, the salt-water mass fraction measurements shown in Figure 18 are converted into a dimensionless salt dispersion signature shown in Figure 19 for each respective detector location. Thus, allowing a direct comparison to be made between the dispersion terms for both systems. A detailed assessment of these terms is presented in Chapter 5. The scaled terms used in the conversion are based on experimental variables. An overview of the calculations is presented in this chapter.

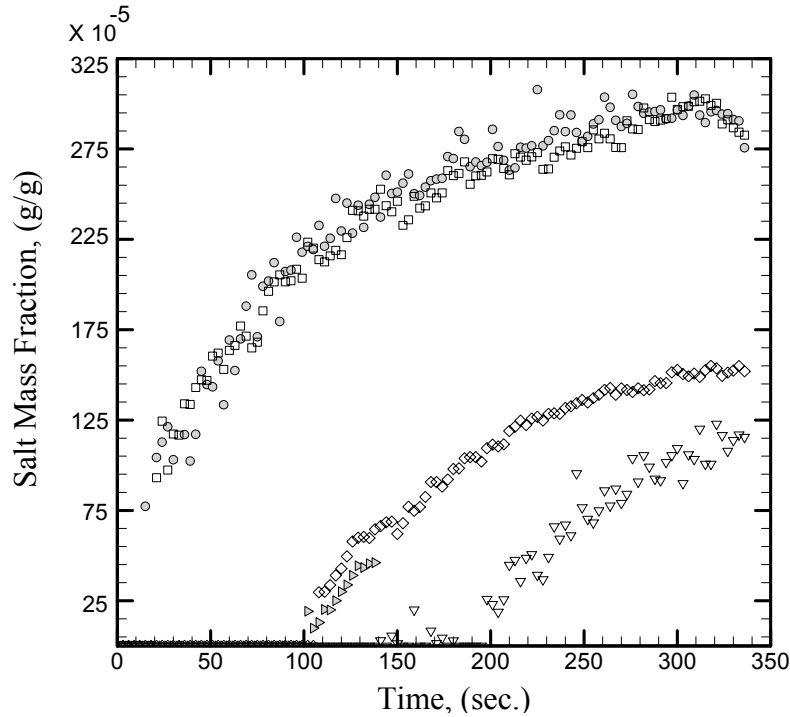


Figure 18: Local  $Y_{salt}$  at detector for salt-water model run with a flow rate of 100 ml/min and initial salt mass fraction of 0.10 g/g.  $\square$  RM1 - C,  $\bullet$  RM1 - S,  $\diamond$  COR - C,  $\blacktriangleright$  COR - S,  $\nabla$  RM2 - C

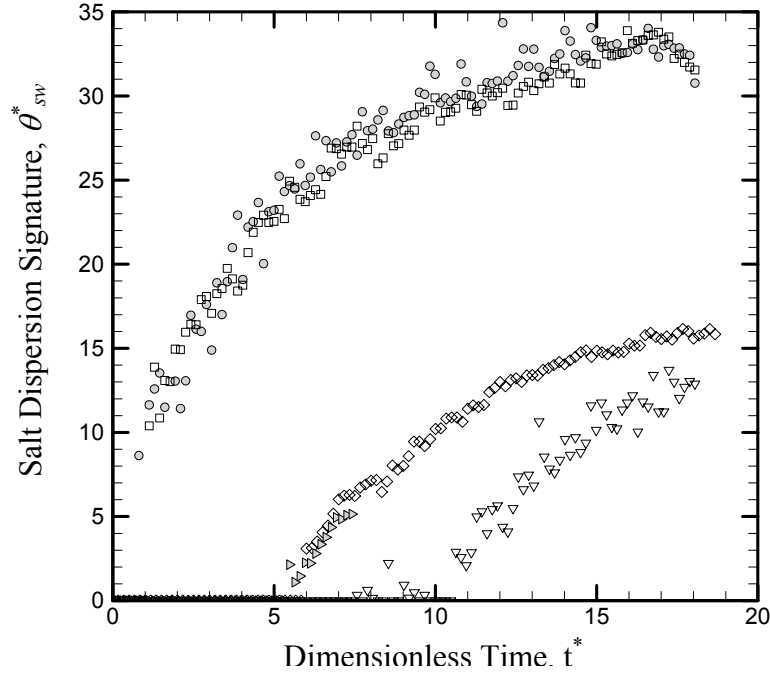


Figure 19: Local  $\theta_{sw}^*$  at detector for salt-water model run with a flow rate of 100 ml/min and initial salt mass fraction of 0.10 g/g.  $\square$  RM1 – C,  $\bullet$  RM1 - S,  $\diamond$  COR – C,  $\blacktriangleright$  COR - S,  $\nabla$  RM2 – C

#### 4.2.1 Dimensionless Salt Mass Flux, $\dot{m}_{salt}^*$

For a proper analysis of dispersive terms, the salt-water results are scaled in the same source based form as the fire data. The non-dimensional source strength for the salt-water model is previously defined in Chapter 2 as

$$\dot{m}_{salt}^* = \frac{\beta_{sw} \dot{m}_{source}}{\rho_o g^{1/2} L_{sw}^{5/2}}.$$

Similar to the fire equations the salt-water source strength can be presented in terms of a mass flux of salt at the injector given by

$$\dot{m}_{source} = \rho_{sw} (Y_{salt})_{inj} \dot{V},$$

where  $\dot{V}$  is the volumetric flow rate,  $(Y_{salt})_{inj}$  is the mass fraction of salt generated at the source, and  $\rho_{sw}$  is the density of the saline solution given by

$$\rho_{sw} = \rho_o + 0.76\rho_o(Y_{salt})_{inj},$$

where  $\rho_o$  is the density of fresh water.

#### 4.2.2 Dimensionless Salt-Water Model Time, $t_{sw}^*$

The non-dimensional time for the salt-water model derived in § 2.2.2 is similar to that of the full-scale fire experiment and is also presented in terms of the source strength in which

$$t_{sw}^* = \frac{t_{sw}}{(\dot{m}_{sw}^*)^{-1/3} (L_{sw} / g)^{1/2}}$$

where  $t_{sw}$  is the experimental time and  $t_{sw}^*$  is the dimensionless time for the salt-water model. The dimensionless time can be computed for any experimental time given a dimensionless injection source strength,  $\dot{m}_{sw}^*$ , and an enclosure height,  $L_{sw}$ .

#### 4.2.3 Dimensionless Salt Dispersion Signature, $\theta_{sw}^*$

Just as the buoyancy force moves smoke in a fire due to a thermal density deficit, the hydraulic analogue has a buoyant force due to the density deficit between the salt-water solution and the ambient fresh water surroundings. A non-dimensional salt-water dispersion term,  $\theta_{sw}^*$ , can be used to describe this important parameter as previously defined in Eqn. (46):

$$\theta_{sw}^* = \frac{\beta_{sw} Y_{salt}}{(\dot{m}_{sw}^*)^{2/3}}$$

where  $\beta_{sw} = 0.76$

where  $Y_{salt}$  is the salt mass fraction. The salt mass fraction is computed based on the measured light intensity of the PLIF images, the details of the conversion are presented in § 3.2.5. Thus, the local salt mass fraction measurement at each detector is converted into this salt-water dispersion signature based on the dimensionless source strength.

### 4.3 Converting from Salt-Water to Fire Quantities

The creation of dimensionless terms for both the salt-water and fire experiments is conducted in order to present the two systems in a parallel analogy. The terms are grouped based on what values actually govern the dynamic dispersion of a buoyant fluid. The source terms are used to create a dimensionless time for both systems. As previously discussed the dimensionless time for the full-scale fire experiment is given by

$$t_{fire}^* = \frac{t_{fire}}{(Q^*)^{-1/3} (L_f / g)^{1/2}}$$

and for the salt-water model

$$t_{sw}^* = \frac{t_{sw}}{(\dot{m}_{sw}^*)^{-1/3} (L_{sw} / g)^{1/2}}$$

By matching the dimensionless time for the fire and the salt-water experiments, a direct analogy is created where

$$\frac{t_{fire}}{(Q^*)^{-1/3}(L_f/g)^{1/2}} = \frac{t_{sw}}{(\dot{m}_{sw}^*)^{-1/3}(L_{sw}/g)^{1/2}}. \quad (62)$$

The dimensionless time for the salt-water and fire systems is a direct function of the dimensionless “source strength” and the length scale of the enclosure. Therefore, simultaneously equating the dimensionless time provides a relationship in which the two systems are in proper analogous form. Eqn. (61) is used to provide a salt-water model time that corresponds to the full-scale fire time of interest. The salt-water model results can be used to equate the fire conditions when the equality in Eqn. (61) is maintained. Thus, the dispersion parameters are directly analogous,

$$\theta_{sw}^* \approx \theta_T^* \approx \theta_{smoke}^*,$$

and the values of interest can be computed based on the experimental conditions of both systems.

## **Chapter 5. Results and Discussion**

### **5.1 Salt-Water Dispersion Analysis**

The following section includes an assortment of sequential still images representing several important stages of dispersion throughout the complex enclosure examined in the current study. The dynamic flows are better understood through visualization; nevertheless all images presented within this section are representative of quantitative spatial and temporal measurements of the flow structure. The salt-water model images are inverted vertically to provide a better comparison with the dispersion dynamics of hot gasses within an enclosure. A scale consistent with the spatial domain is provided for all images. The large tick marks correspond to a spacing of approximately 55 millimeters and the small tick marks represent approximately 11 millimeters, in scale model space. In the full-scale model, these dimensions correspond to 0.39 meters and 0.07 meters respectively. The time scales for the Figures illustrated in this section, range from 2 seconds to 10 seconds in model space and 0.7 seconds to 3.8 seconds in full-scale space.

#### **5.1.1 Initial Plume and Ceiling Jet**

A vertical planar slice is taken within the source room of the enclosure model. As shown in Figure 20, the planar sheet bisects the centerline of the injector and passes through the doorway leading into the corridor. The primary stages of dispersion within the source room of the salt-water model are captured in Figure 21. The large eddies seen in the initial region of the plume demonstrate strong turbulent dispersion characteristics. The turbulence is observed early on and is persistent throughout the height of the plume. The dynamics of the plumes early interaction with the ceiling depicts the generation of large

tornoidal vortex structures. This initial vortex flow is bounded by the adjacent enclosure wall and is forced to travel downward, quickly becoming engulfed by the plume. The unobstructed vortex flow slowly travels away from the plumes centerline and is dissipated by the underlying ceiling jet flow. The ceiling layer is inhomogeneous and has a total thickness of approximately  $H/10$  initially and grows to a height corresponding to the doorsill (illustrated by a gray line in Figure 21).

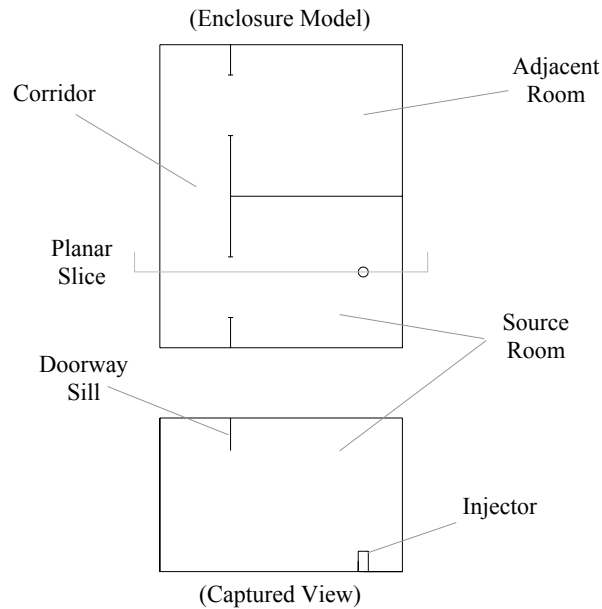
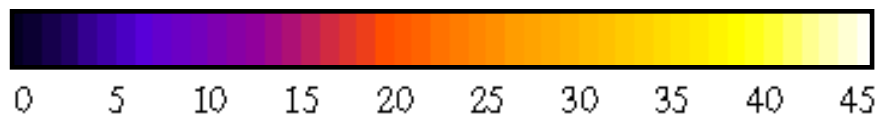
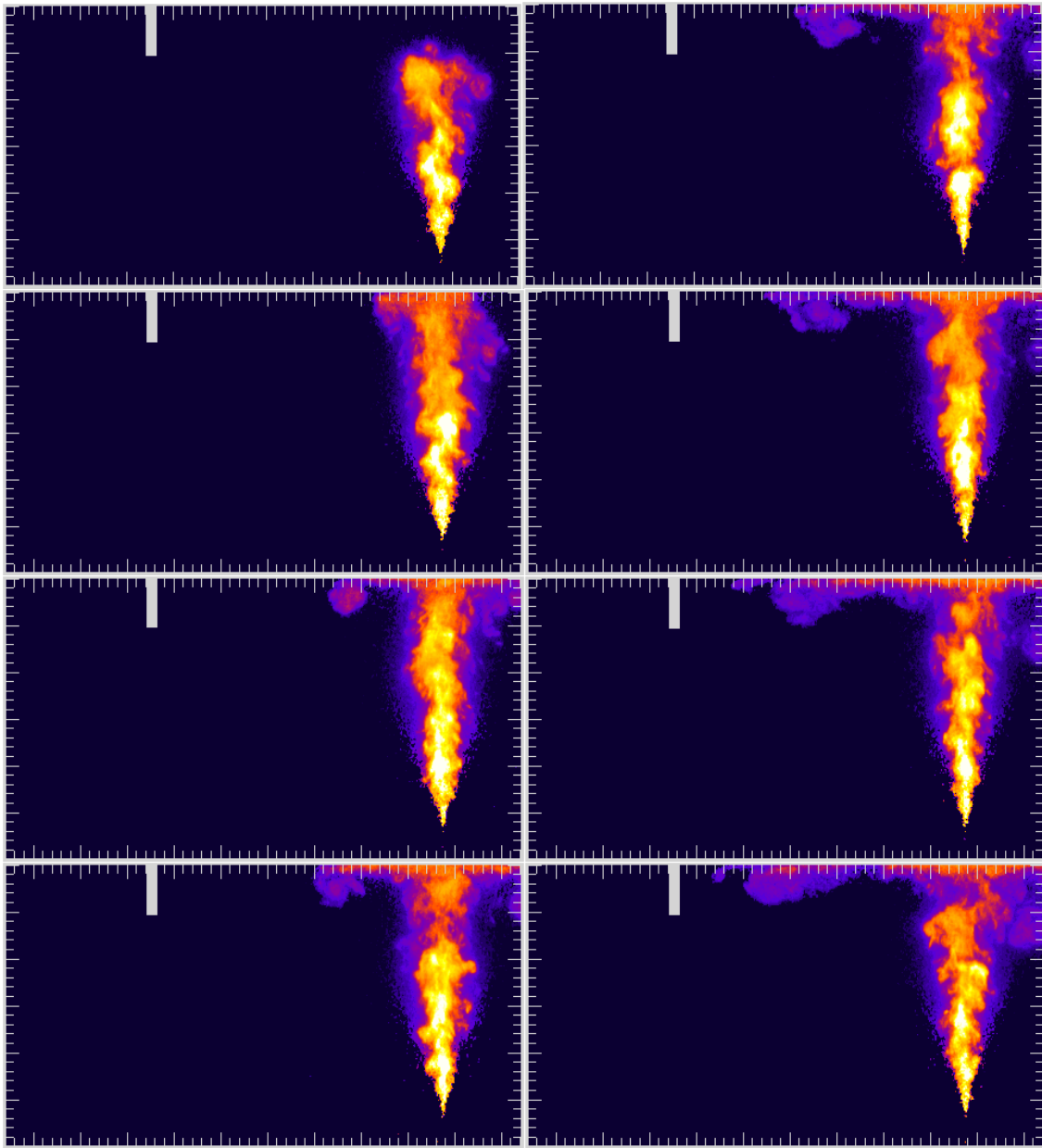


Figure 20: Aerial and side view of the planar sheet location for slice #1. Slice #1 bisects the injector and doorway of the source room.

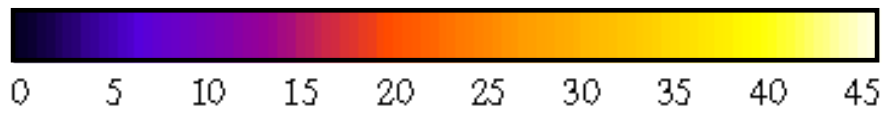
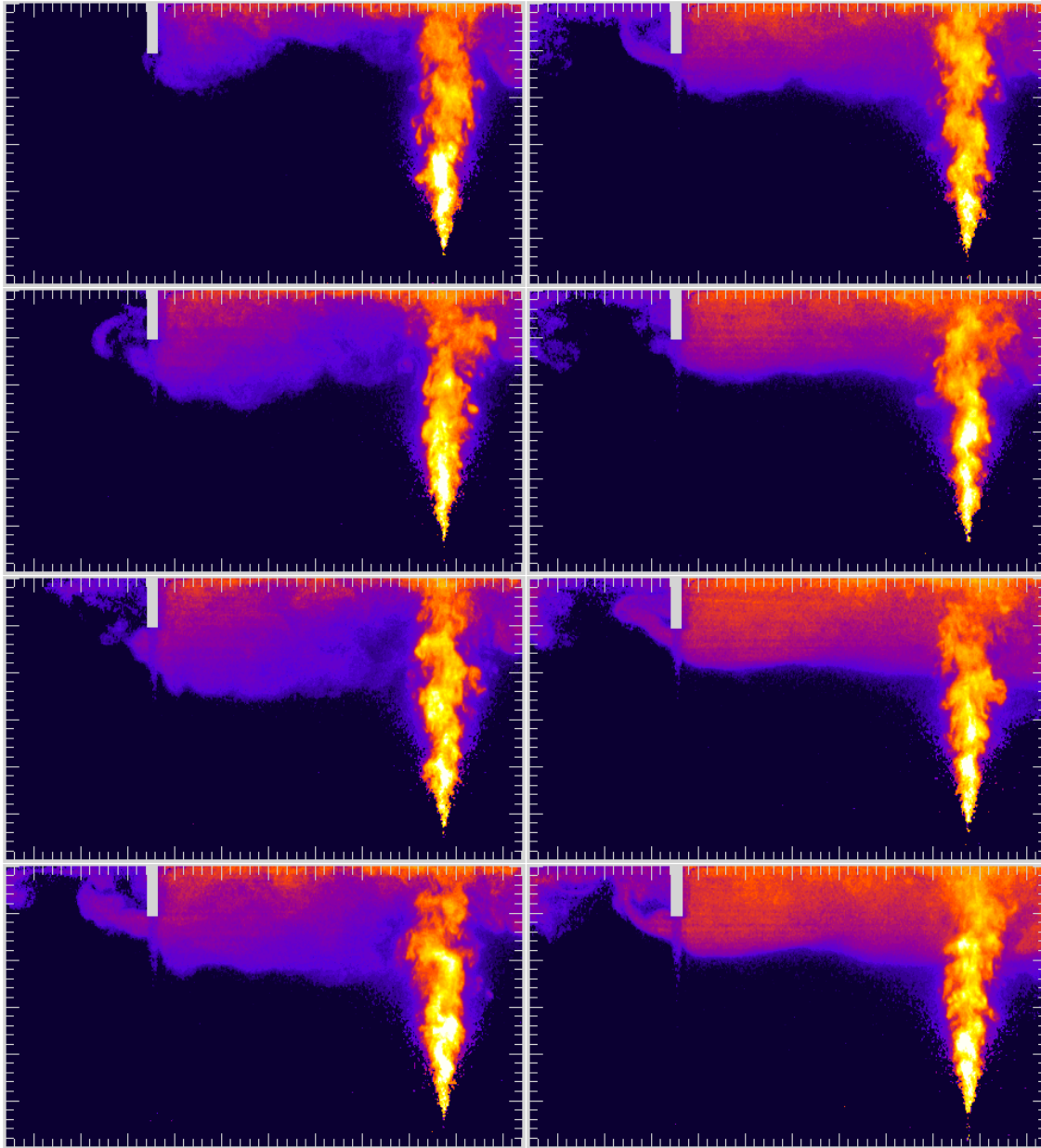


$\theta^*$

Figure 21: Series of primary images illustrating the plumes interaction with the ceiling. Images represent 2-second intervals in salt-water and 0.7-second intervals in fire experimental time,  $t^* = 0.10$ .

### **5.1.2 Initial Doorway Flow Dynamics**

The same planar view described by Figure 20 is examined as the time progresses and filling occurs. The secondary stages of dispersion within the source room are shown in Figure 22, where the ceiling layer descends below the doorsill and fluid spills into the adjacent corridor. The initial ceiling jet impinges on the doorsill creating a reflected wave directed toward the centerline of the plume. The wave creates a ceiling layer that is approximately 60% thicker than the ceiling layer on the wall side. The transient stages in the source room illustrate a non-homogeneous ceiling layer that descends to approximately twice the height of the doorsill. As the ceiling layer spills into the adjacent corridor the dynamics in the source room resemble steady state conditions. The uniformity of the ceiling layer increases significantly and the interface between the ceiling layer and the ambient environment becomes well established. Though the plume penetrates the ceiling layer, the inhomogeneities near penetration mix out with increasing radial distance from the plume centerline.



$\theta^*$

Figure 22: Series of images illustrating the source room ceiling layer doorway spill. Images represent 5-second intervals in salt-water and 1.9-second intervals in fire experimental time,  $t^* = 0.27$ .

### 5.1.3 Corridor Frontal Flow Dynamics

A cross-section through the length of the corridor connecting the two compartments is observed within this section as illustrated in Figure 23. The initial doorway flow seen in Figure 24, spills from the source room into the corridor in a non-uniform and unsteady manner. Once the spilling impinges the ceiling the flow experiences radial dispersion. The walls adjacent to the doorway restrict the horizontal movement of the ceiling layer to one direction. Small-scale wave reflection occurs throughout the corridor when the flow impinges upon the enclosure walls. The magnitude of the reflected waves varies due to the directional change of the original flow. Thus, creating cross currents and the instabilities that are seen in the ceiling layer. The localized layer thickness and strength increases temporally as the ceiling jet propagates along the length of the corridor. With the leading ceiling jet thickness being approximately  $H/6$  and the layer thickness above the doorway being approximately  $H/3$ . When the ceiling jet reaches the far end of the corridor a drastic reflected wave occurs that increases the total ceiling layer height to roughly half the enclosure height,  $H/2$ .

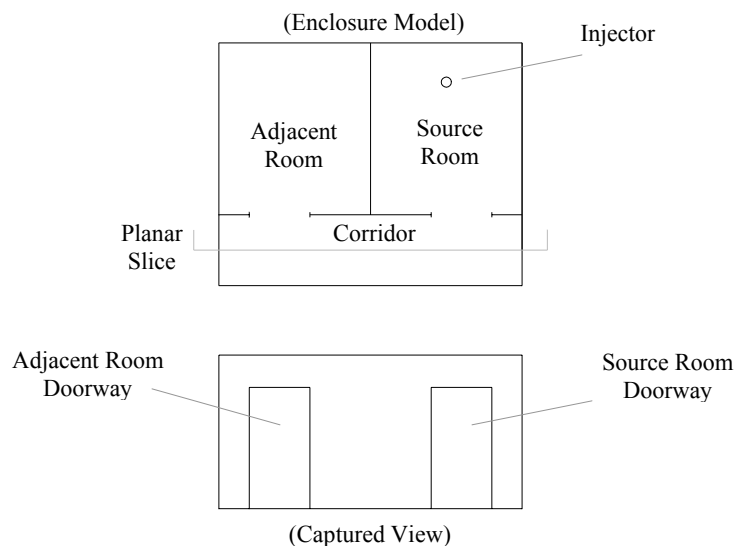
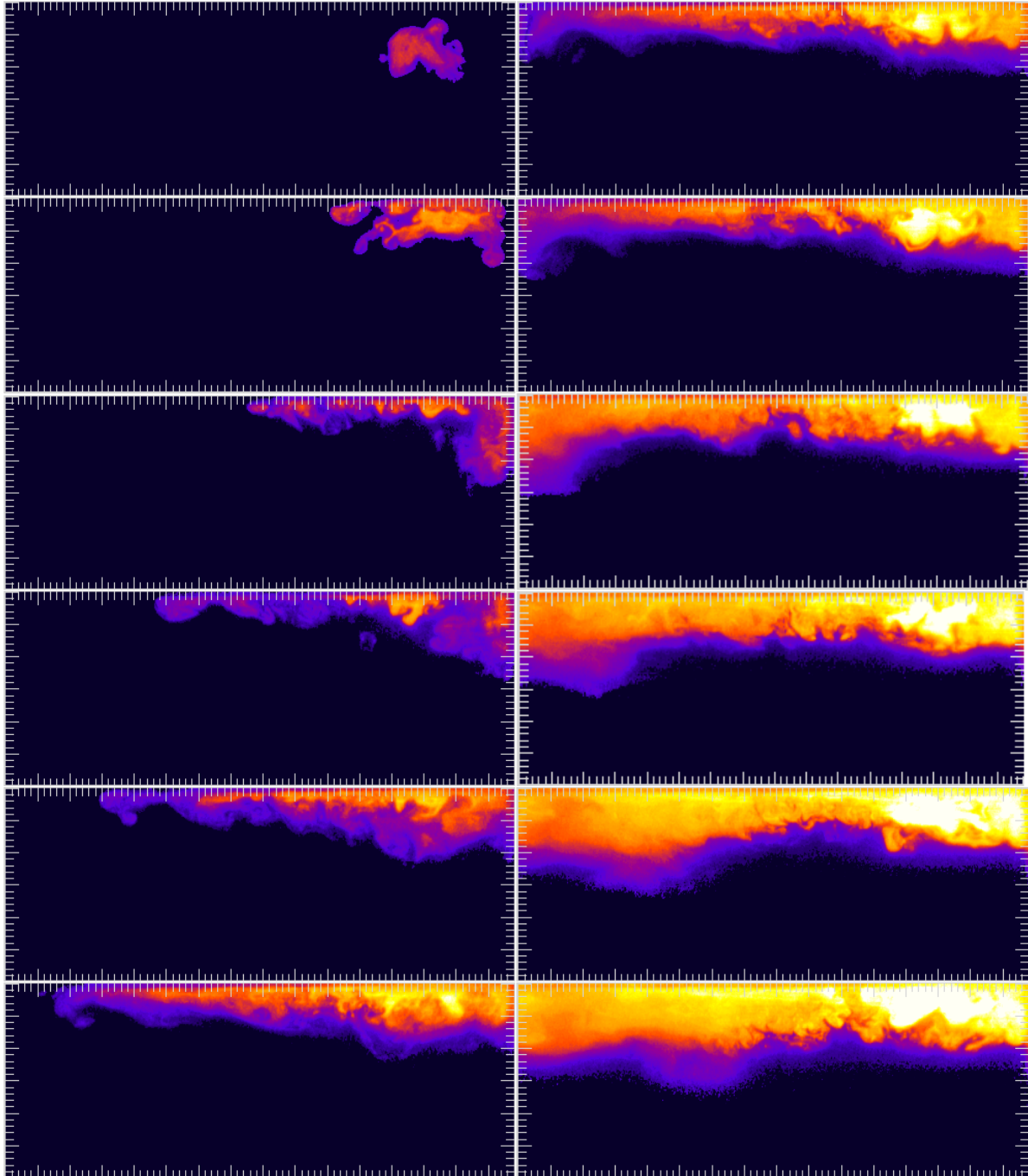


Figure 23: Arial and side view of the planar sheet location for slice #3.



$\theta^*$

Figure 24: Series of images illustrating the corridor flow dynamics. Images represent 10-second intervals in salt-water and 3.8-second intervals in fire experimental time,  $t^* = 0.54$ .

### 5.1.4 Secondary Doorway Flow Dynamics

The planar view examined in this section depicted by Figure 25. The final stage of dispersion examined within this study, in which the corridor flow begins to spill into the adjacent compartment is illustrated in Figure 26. The initial doorway flow from the corridor into the adjacent room is much more stable than the doorway flow examined in § 5.1.2 and maintains very ordered characteristics. As the doorway flow impinges upon the ceiling a very thin ceiling layer is created, with an initial thickness of less than  $H/15$ . The ceiling layer is relatively homogeneous throughout the adjacent enclosure and does not undergo any large scale mixing. The wave reflection that occurs once the ceiling jet reaches the far end of the enclosure does not create any significant mixing within the ceiling layer. Beyond the final image of the series below no substantial dynamics are observed as the adjacent room slowly fills with dispersed fluid. Only the initial spilling and ceiling jet propagation is provided, as future images are redundant and unrelated to the focus of this study.

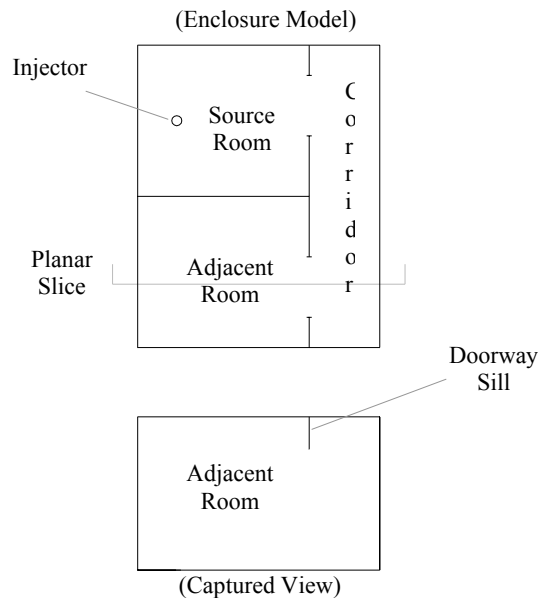


Figure 25: Arial and side view of slice of planar sheet location 4.

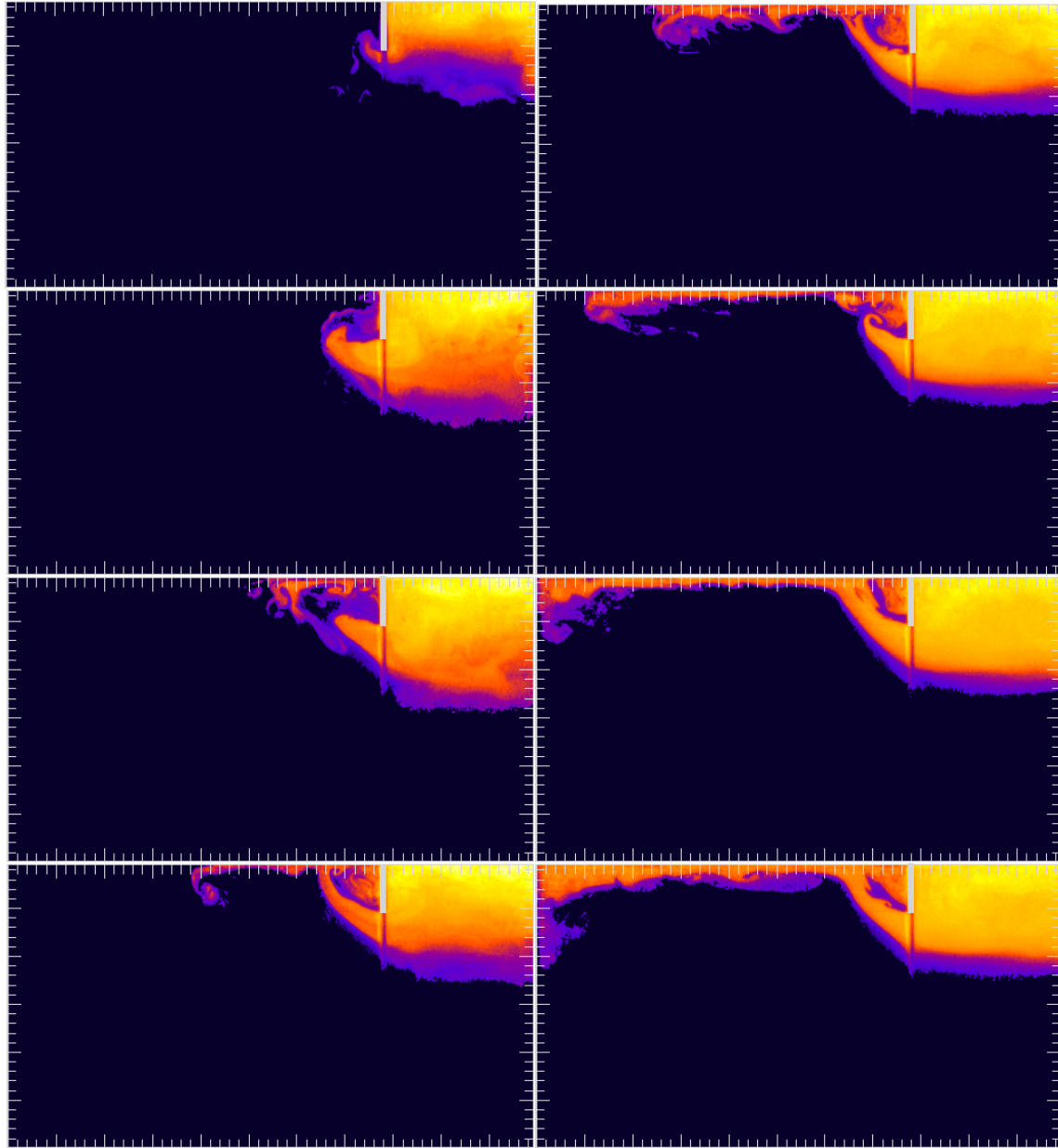


Figure 26: Series of images illustrating the corridor to adjacent room doorway spill. Images represent 10-second intervals in salt-water and 3.8-second intervals in fire experimental time,  $t^* = 0.54$ .

## 5.2 Fire Response Time Analysis

The following section provides an evaluation of the experimental data obtained from the full-scale fire test facility. The local conditions and dispersion dynamics are examined within the enclosure at the relative position of each of the five ionization smoke detectors. A schematic of the detector locations within the enclosure is provided by Figure 27. The data is presented in a manner that tests the functionality of the detectors response to various principles of dispersion. Please note, that any references made toward a smoke detector is suggestive of only the ionization type units examined in this study. Further examination is necessary to test this method for all smoke detection devices.

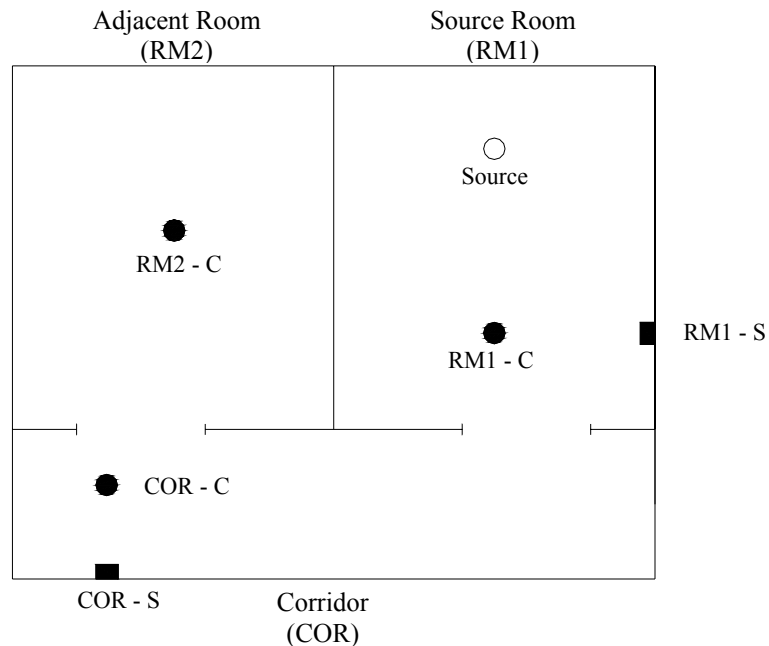


Figure 27: Arial view of the enclosure and smoke detector locations; ○ represents the fire or salt-water source, ● represents ceiling mounted smoke detectors and ■ represents sidewall mounted smoke detectors.

### 5.2.1 Local Conditions at the Time of Alarm

The local conditions including temperature and light obscuration, measured in the full-scale test facility at the detector location, are examined to determine a possible threshold for detector response. The threshold represents a dimensionless dispersion value that is observed at any detector in the enclosure at the time of activation and allows the activation time to be predicted using the model dispersion measurements. For each detector the respective temperature rise and smoke mass fraction is computed from the experimental data at the time of alarm. The localized values are presented in Figure 28 and Figure 29, for each respective location. The values were obtained in the full-scale fire experiments by measuring the local gas temperatures with type-k thermocouples and the local light obscuration with a laser and photodiode relative to each detectors position within the enclosure. The computations composed in § 4.1.4 illustrate the conversion from light obscuration to smoke mass fraction.

The temperature data suggests that the heat loss associated with the enclosure walls is significant at the time of alarm. In comparing the localized gas temperatures for the ceiling mounted detectors (RM1 - C, COR - C, RM2 - C), a trend is observed in which the gas temperatures at alarm reduce considerably as the dispersion distance from the source increases. While the initial front propagates from the source plume along the ceiling, it experiences heat loss due to the temperature difference associated with the flow and the enclosure walls. The transient exposure and subsequent losses are significant if the front must travel great distances. The local gas temperatures for the sidewall-mounted detectors (RM1 - S, COR - S) are subjected to even greater losses as gasses are

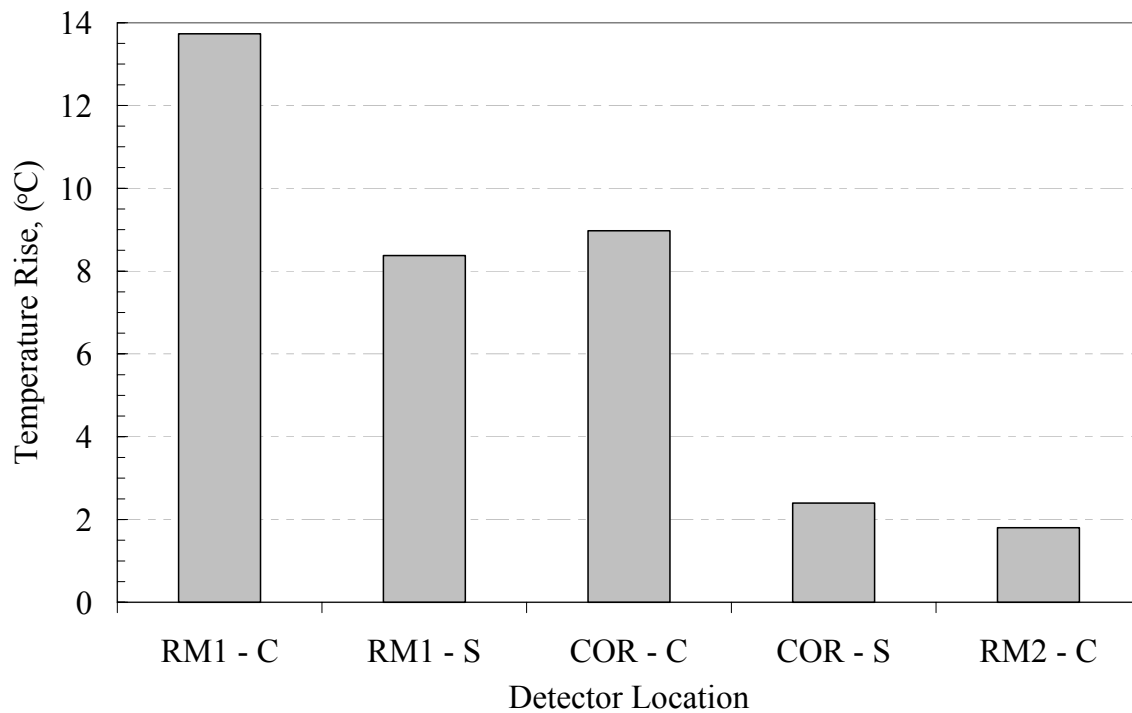


Figure 28: Localized gas temperature rise for each of the five detectors.

exposed to the ceiling as well as the adjacent wall in which the detector is mounted. These losses are observed in the experimental data by comparing detectors (RM1 - C and RM1 - S) as well as detectors (COR - C and RM2 - C). Both sets of detectors are positioned with a relatively similar radial distance from the source, yet for both cases the sidewall-mounted units alarm at much lower local gas temperatures than the neighboring ceiling mounted unit. Furthermore, the local gas temperature rise at the time of activation ranges from almost 14 °C in the source room to less than 2 °C in the adjacent compartment. Therefore, it would be erroneous to depict the response of the ionization smoke detectors in terms of the local gas temperatures without somehow accounting for the proximity of the detector to the source fire.

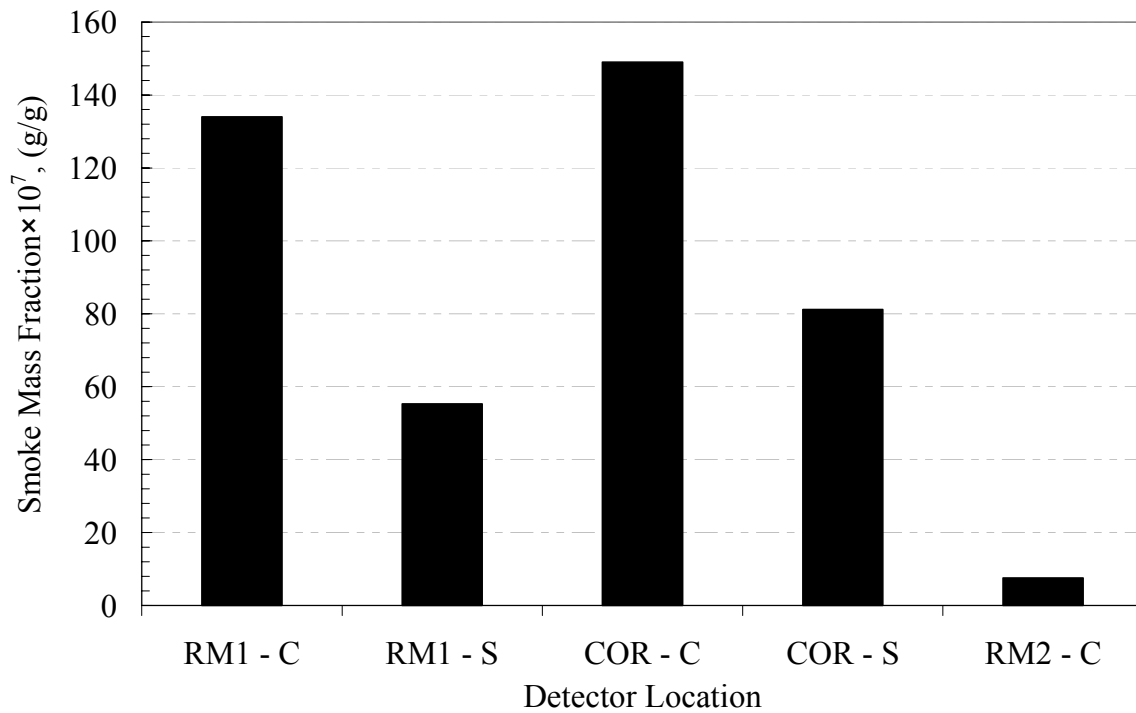


Figure 29: Localized smoke mass fraction at each detector location.

In addition to the temperature measurements, the local smoke mass fraction shown in Figure 29 is examined at the time of activation. Mass loss to the enclosure walls is observed in the experimental data, as the mass fraction of smoke at the time of alarm actually increases; comparing ceiling-mounted detectors (RM1 - C and COR - C), and sidewall-mounted (RM1 - S and COR - S). However, a similar trend is observed in which the sidewall-mounted units alarm at a lower smoke mass fraction than the nearby ceiling-mounted units. Thus, signifying additional information is needed to use the local smoke mass fraction measurements as a predictive indicator of detector response.

### **5.2.2 Dispersion and Detector Response Times**

The initial presence of dispersed gasses, presented in this discussion as the front arrival, is an important element in characterizing the response of a smoke detector. As no visual data was recorded for the full-scale fire tests, the time associated with the front arrival was estimated from local measurements. The thermal front (based on the temperature data) arrives at the same time if not earlier than any observed change in light obscuration as shown in comparing Figure 14 with Figure 16 from § 4.1. As a result, the initial occurrence of an increasing local gas temperature is used as an approximation for the presence of the front for each respective location. The front arrival time represents the time from which the fuel is first ignited to the estimated arrival of the smoke. In addition, the time lag between the front arrival and the activation time of the detector is identified as the activation delay time for this discussion. The front arrival times and delay response times associated with each respective detector location are presented in Figure 30 and Figure 31. It should be noted that the sum of the front arrival time and delay time represents the detector activation time. A previous discussion in § 5.2.1 suggested that the orientation of the smoke detector is a significant factor in determining its response. Therefore, the following results are separated by orientation to better evaluate the response properties. The front arrival and lag time of the ceiling-mounted units is shown in Figure 30 and Figure 31 is representative of sidewall-mounted units.

The detector lag times maintain a relatively constant value and seem to be independent of the detector location and relative position with respect to the source, as shown in Figure 30 and Figure 31. The sidewall-mounted detectors have a mean delay time of 13.5

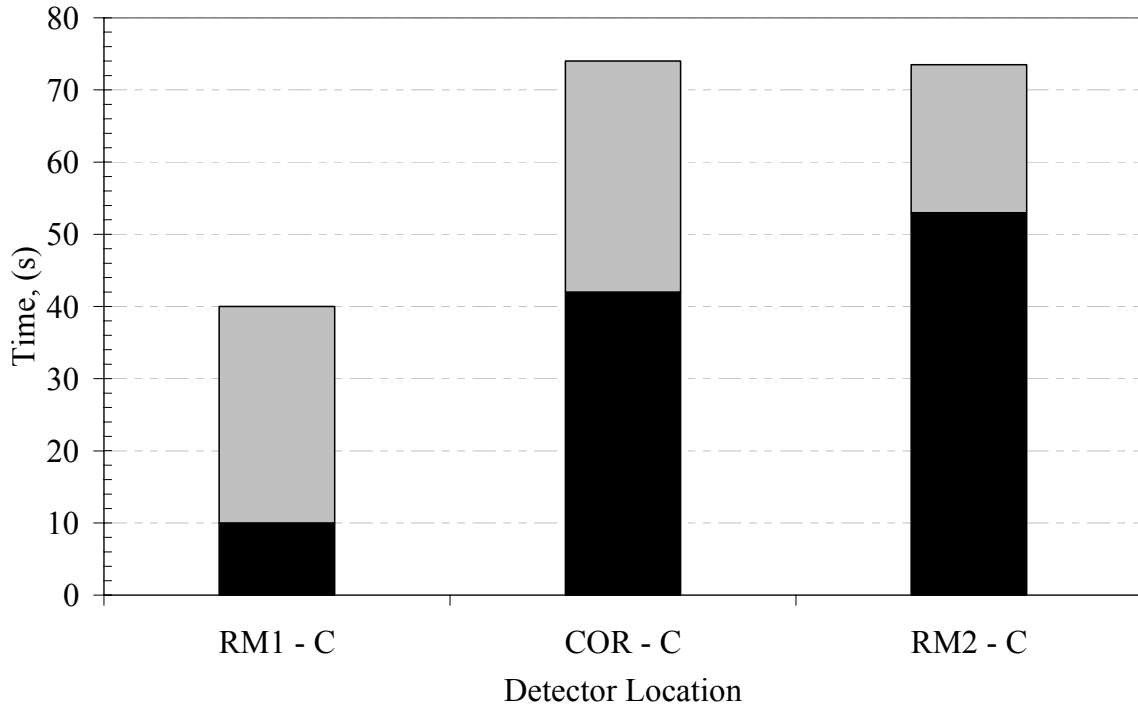


Figure 30: Ceiling-mounted ionization smoke detector response data from full-scale fire experiments; ■ front arrival time, ■ detector activation lag. Note: detector activation time is the sum of the arrival and lag times.

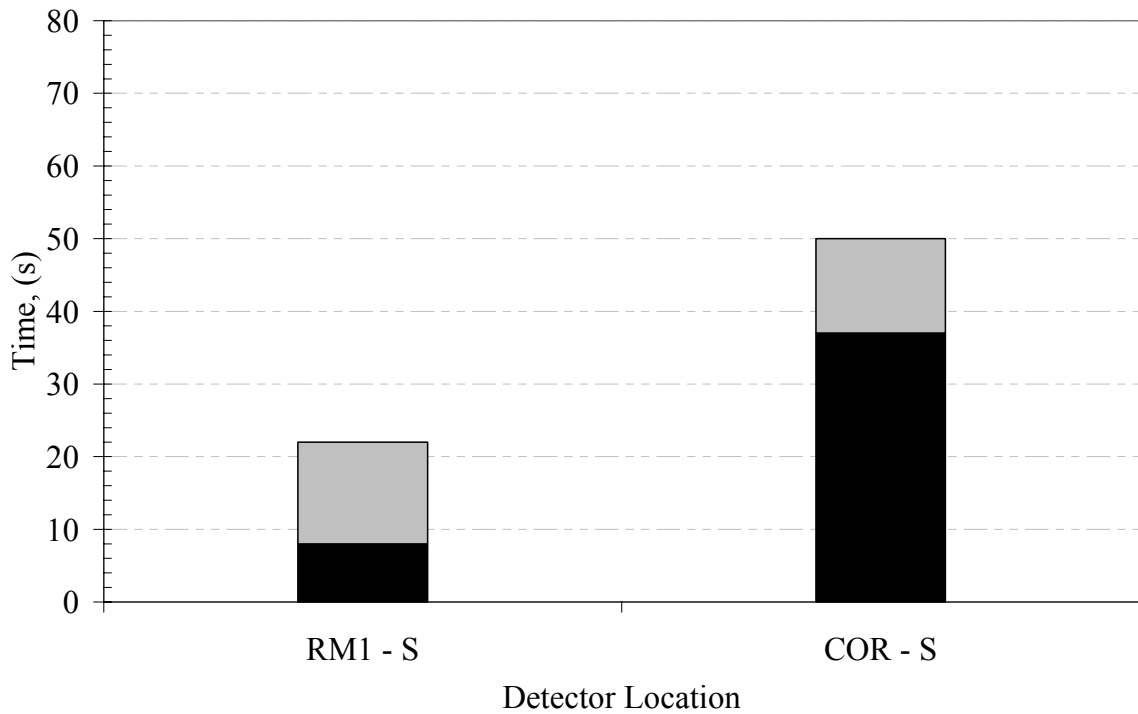


Figure 31 Sidewall-mounted ionization smoke detector response data from full-scale fire experiments; ■ front arrival time, ■ detector activation lag. Note: detector activation time is the sum of the arrival and lag times.

seconds and a standard deviation of 5% and the ceiling-mounted detectors have a mean delay time of 27.5 seconds and a standard deviation of 22%. The data suggests that the orientation of the detector effects the lag time associated with its response. The difference in response times may be due to the unit's sensing chamber orientation with respect to the flow or due to the increased flow velocities, which are not examined or discussed within this study. However, existing literature does suggest the detector response lag is directly related to the external flow velocity.<sup>34</sup> Additionally, the front arrival time provides a first order approximation for the detector response assuming the lag time remains relatively constant. A discussion and comparison of the lag times for the full-scale and salt-water model results is presented in § 5.3.2.

### **5.3 Predicting Detector Response Time**

The following section provides a detailed comparison of the quantitative results obtained from the salt-water experiments conducted within this study with the data acquired from the full-scale test facility. The relevance of the experimental results with regards to detector response is established in this discussion. A comparative analysis between fire and salt-water model data is conducted with a focus on dimensionless front arrival times, detector activation lag times and dimensionless dispersion parameters. A collection of tables summarizing the important parameters and times described in this section is included in Appendix A, for the fire and salt-water experiments.

### 5.3.1 Front Arrival Comparison

To facilitate the comparative analysis, the temporal results of the salt-water model and full-scale fire experiments are dimensionless as discussed in Chapter 4. The arrival of the front in the salt-water experiments was determined based on the initial fluorescence of the dyed salt-water mixture for each location of interest. Both visual and quantitative data were used to establish the front arrival times. The front arrival times for the geometrically scaled detector locations are presented in terms of detector location and non-dimensional time,  $t^*$ . As illustrated in Figure 32, the front arrival times for dispersive flows in the salt-water model are in excellent agreement with the full-scale fire test data. The minor discrepancies in which the salt-water model “over predicts” the front arrival may be due to experimental error in the full-scale experiment. There is a delay time associated with the thermocouple measurements that would create a lag in the estimation of the front arrival from the measured the local gas temperatures. This discrepancy may also be due to the fact that the salt-water model cannot account for the reduction in buoyant forces due to heat loss.<sup>6,7,8,15</sup> The results discussed in § 5.2.2 demonstrate that the front arrival time provides a first order approximation of the detector response times. However, to completely describe the detector response time, the lag time for the detector to alarm, after the front has arrived, must also be considered. In fact, the lag time associated with the detection devices examined in this study is often of the same order as the front arrival time. This lag time is largely dependent on the interaction with the detector. Therefore, a model for the lag time and appropriate measurements for the model inputs would be required to accurately use salt-water modeling to predict smoke detector activation.

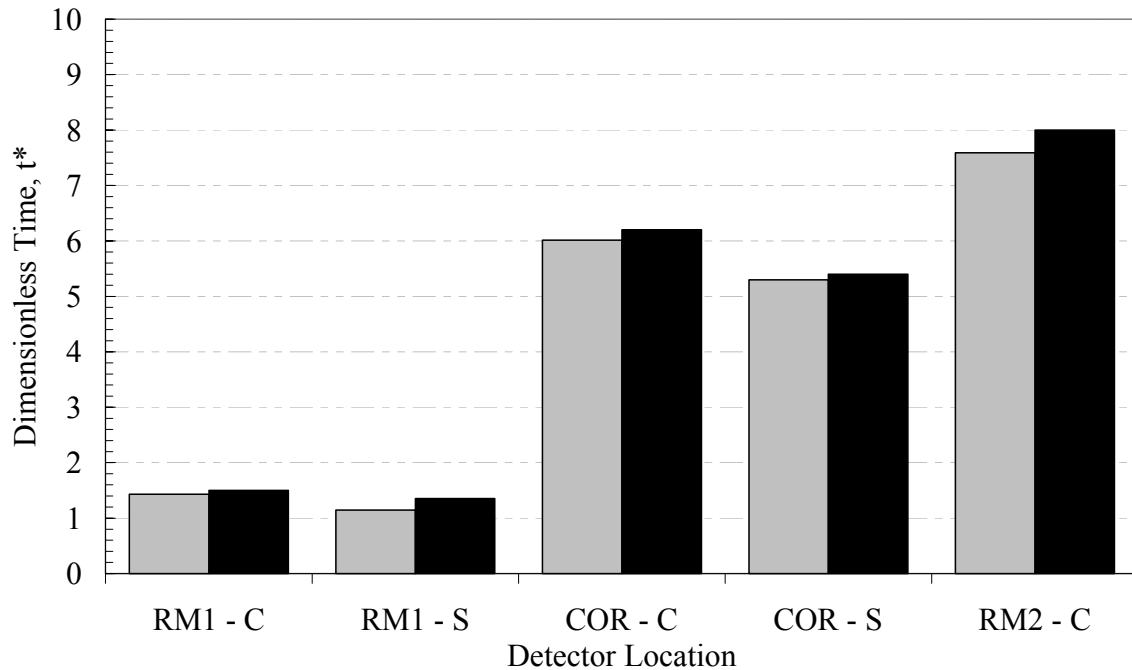


Figure 32: Dimensionless front arrival time for respective detector locations;  
 ■ full-scale fire experiment, ■ salt-water model

### 5.3.2 Activation Lag Time

An evaluation of the dimensionless lag time for the full-scale fire data is presented in Figure 33, for each respective detector location. The results provided in Figure 33 demonstrate that the lag time maintains a relatively constant value for the ceiling-mounted detectors (RM1 - C, COR - C, RM2 - C) as well for the sidewall-mounted detectors (RM1 - S, COR - S). Thus, a characteristic lag time,  $t_{lag}^*$ , is defined for the orientation of the smoke detector. These characteristic values are found by averaging the full-scale fire experimental lag times for the ceiling-mounted detectors as well for the sidewall-mounted detectors. Respective values are found to be  $t_{lag}^* = 3.9$  for ceiling-mounted and  $t_{lag}^* = 1.9$  for sidewall-mounted detectors.

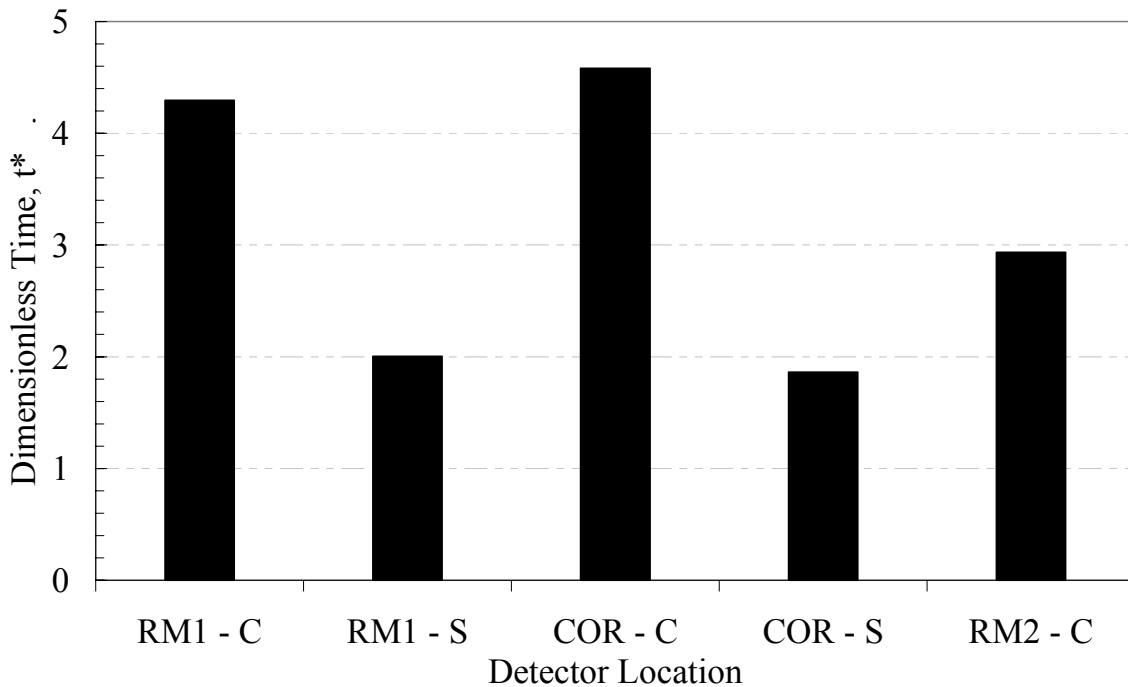


Figure 33: Dimensionless activation lag times for respective detector locations;  
 ■ full-scale fire experiment

### 5.3.3 Detector Response Time Predictions

By combining the salt-water model front arrival time described in § 5.3.1 with the  $t_{lag}^*$  described in § 5.3.2, a simple model is created for predicting the activation times of each smoke detector. The predicted activation times are compared to the actual response time from the full-scale experiment in Figure 34. The model predicts the activation times at every location within the enclosure with very good accuracy. The dimensionless predictions are converted into actual time using the methodology described in § 4.3. The model results are presented alongside the “real” experimental activation times from the full-scale fire experiment within Table 3 including a calculation of the percent error associated with the prediction. The average error in the response time prediction is less

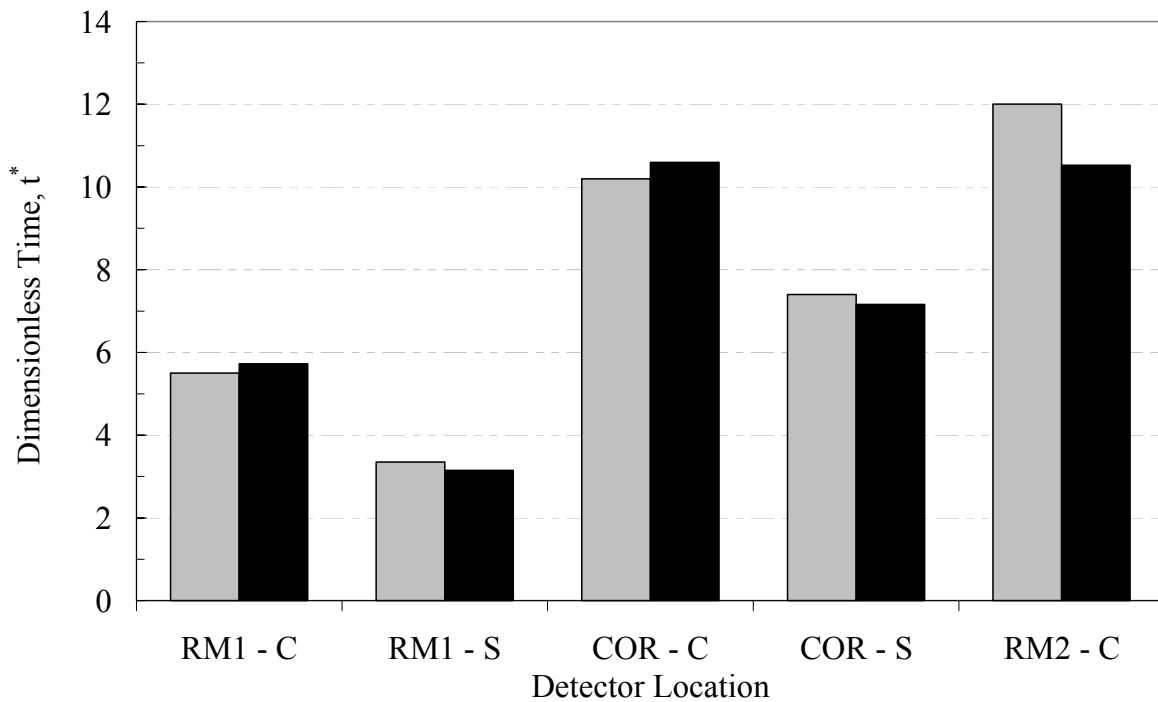


Figure 34: Salt-water models predicted smoke detector response times;  
 ■ salt-water model prediction, ■ actual activation time

then 5% for four of the five detector locations examined within this study (RM1 –C, RM1 – S, CORR – C, COR – S). The response time prediction for the furthest detector from the source (RM2 – C), located in the adjacent room, was still accurately modeled with an error of around 13%. The increased error associated with detector RM2 – C, is most likely due to the poor resolution seen in salt-water model results. At this location the arrival of the dispersive front was difficult to ascertain and a detailed analysis of these results is presented in § 5.4. The simple method used to model the smoke detector activation times shows promise as a predictive tool and provides an excellent foundation for future research pertaining to the objectives of this study. More advanced models may include such things as velocity measurements and detector entrance lag correlations.

Table 3: Dimensionless and actual predicted detector response times

Detector Location	Dimensionless Activation Times, $t^*$			Actual Activation Times, (sec.)		
	Predicted	Real	Percent Error	Predicted	Real	Percent Error
RM1 - C	5.5	5.7	4	38	40.0	4
RM1 - S	3.4	3.2	6	23	22.0	6
COR - C	10.2	10.6	4	71	74.0	4
COR - S	7.4	7.2	3	52	50.0	3
RM2 - C	12.0	10.5	13	84	73.5	13

## 5.4 Salt-Water and Fire Dispersive Parameter Comparison

### 5.4.1 Dispersion Comparison at Activation Time

Dimensionless signatures that characterize the dispersion for both the salt-water and full-scale fire experiments are presented within this section at the time in which each detector alarms. The dimensional analysis of the governing equations, presented in Chapter 2, describes the importance of these dispersion parameters and the manner in which they are computed is presented in Chapter 4. It should be noted that the salt-water analogue is representative of the dispersive characteristics of an adiabatic fire with a constant source strength. Thus, small discrepancies in terms of dispersion characteristics are expected due to the non-ideal boundary conditions associated with a real fire. The thermal dispersion parameter,  $\theta_T^*$ , the smoke dispersion parameter,  $\theta_{smoke}^*$ , and the salt-water dispersion parameter,  $\theta_{sw}^*$ , are all computed at the time of activation for each respective detector location and the results are illustrated in Figure 35. At the time of alarm, the relative value of  $\theta_{sw}^*$  with respect to detector location is comparable to the  $\theta_T^*$  for the full-scale

fire. However, the magnitude of  $\theta_{sw}^*$  at detector locations (RM1 – C, RM1 – S, CORR – C, COR – S) is around three times greater than the  $\theta_T^*$ . This may be due to the fact that the salt-water model does not account for the reduction in gas temperatures associated with heat loss to the enclosure walls. If the losses are significant the model will over predict the temperature dependent  $\theta_T^*$ . The comparison presented in Figure 35 suggests that the heat losses are significant throughout the enclosure geometry. The discrepancy may also be due to the response lag time associated with the type-k thermocouples used to measure the local gas temperatures in the full-scale fire experiment. The amplified dispersion values seen at locations RM1 – C, RM1 – S, CORR – C, COR – S is not observed at location RM2 – C. The difference may be due to the fact that the resolution of the experimental data at this location was poor due to the low levels of dyed saline solution and erratic nature of the flow. A detailed evaluation of these results is presented in § 5.4.2.

No significant trends are observed in comparing the salt-water models  $\theta_{sw}^*$  and the smoke dispersion parameter,  $\theta_{smoke}^*$ , for the full-scale fire experiment. However, a constant value of  $\theta_{smoke}^* \approx 2$  is observed for the ceiling mounted units (RM1 – C, COR – C) and a constant value of  $\theta_{smoke}^* \approx 1$  is observed for the sidewall mounted units (RM1 – S, COR – S) at the time of detector activation. Once again, the ceiling mounted detector located in the adjacent room (RM2 – C) does not follow the trends observed at the other locations within the enclosure, with a  $\theta_{smoke}^* < 0.1$ . The lack of consistency at this location suggests

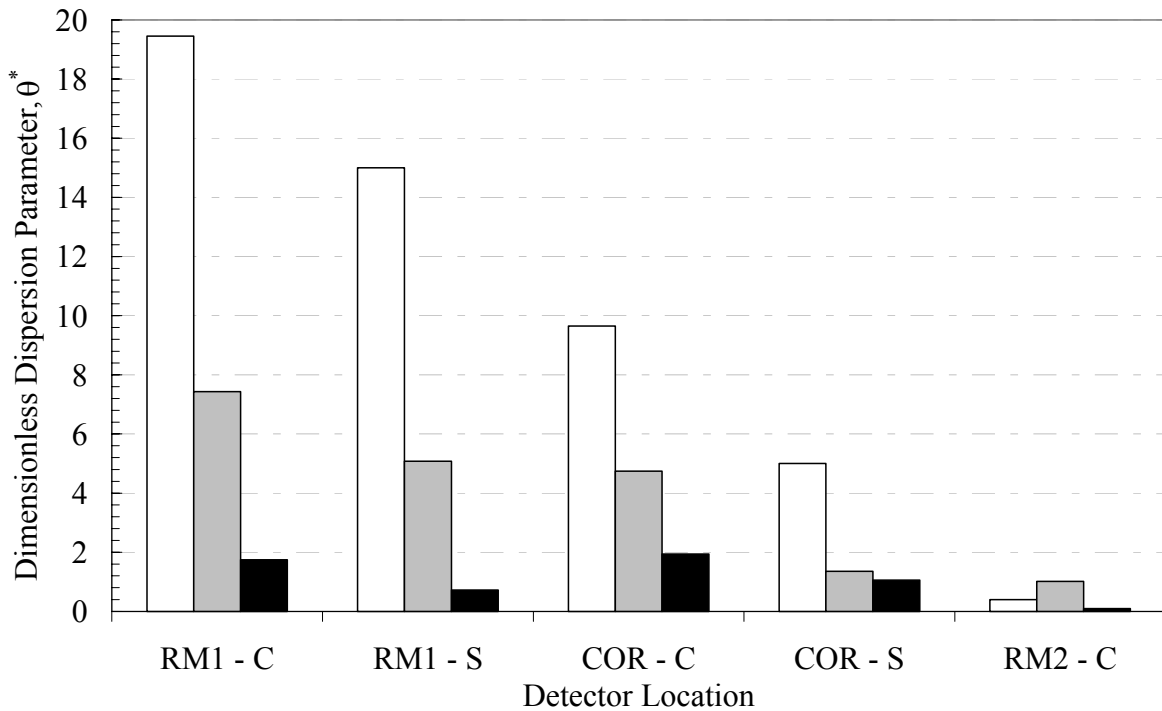


Figure 35: Local dimensionless dispersion signature at detector activation;  $\blacksquare \theta_{smoke}^*$ ,  $\blacksquare \theta_T^*$ ,  $\square \theta_{sw}^*$

that the poor resolution and erratic nature of the flow presents a significant source of error. Further examination of the temporal evolution of the scaled salt-water and fire data at each detector location is essential for determining the reasons for this discrepancy.

#### 5.4.2 Evolving Dispersion Signature Comparison

The temporal evolution of the salt-water and fire dimensionless dispersion signature is presented in Figure 36 through Figure 40, for each detector location. A general description of the trends observed throughout the enclosure is presented within this section. Followed by an evaluation of the local salt-water and fire dispersion parameters and the variations observed at each location within the enclosure.

This study has demonstrated that the scaled front arrival times for the fire and the salt-water systems compare favorably. However, the experimental data suggests that the heat losses down stream of the source significantly reduce the dispersion signature magnitudes from the predicted values measured in the ‘adiabatic’ salt-water analogue. The heat loss to the surroundings is a function of the temperature difference between the gasses and the adjacent surfaces as well as the flow velocity, thus it is difficult to correct for. The losses are very strong as the initial front arrives and become less significant as the boundaries heat up as shown in Figure 36 through Figure 40.

A comparative analysis demonstrates that for all five of the detector locations the salt-water dispersion signature,  $\theta_{sw}^*$ , increases at the same dimensionless time,  $t^*$ , as the smoke and thermal dispersion signatures,  $\theta_{smoke}^*$  and  $\theta_T^*$ , for the full-scale fire. Yet, the fire dimensionless dispersion signature illustrates a slow increase in magnitude when presented with the salt-water results that are nearly discontinuous at the front arrival. The salt-water results throughout the enclosure suggest a strong initial front. At all locations examined within this study  $\theta_{smoke}^*$  is consistently smaller and tends to lag behind  $\theta_T^*$ . This trend may be due to experimental error in the full-scale obscuration measurements or may be due to an assumption made in defining  $\theta_{smoke}^*$ . The measurements taken in the full-scale experiment demonstrate the erratic nature of a fire with an unsteady source in which multiple variations in the temperature rise are observed for a single location and neither the temperature nor the light obscuration measurements converge toward any steady state value. The details associated with each location of interest within the enclosure are presented in a manner that allows the reader to understand and visualize the comparison

made between the full-scale and model results. The detector locations described in this section are illustrated early on in § 5.2 in Figure 27.

Detector RM1-C is ceiling mounted in the source room and is located near the initial plume impingement on the ceiling. The important dimensionless signatures that describe dispersion for the salt-water and fire experiments are presented for this detector location as a function of the subsequent dimensionless time in Figure 36. The salt-water dispersion parameter,  $\theta_{sw}^*$ , at this location increases rapidly upon front arrival and begins to plateau to a value ranging between 27 and 34. The fluctuations in  $\theta_{sw}^*$  may be due to the observed turbulent conditions at this particular location. The small separation (approximately  $\pm 10\%$ ) observed with varying flow conditions suggests that the scaling parameters are not entirely descriptive of the flow behavior. When the flow rates change the virtual origin changes. Modifying the length scale by the virtual origin effect improves the scaling. However, for consistency the length scale used in this study is based on the enclosure height.

The thermal dispersion signature,  $\theta_T^*$ , for RM1-C initially increases at the same dimensionless time,  $t^*$ , as  $\theta_{sw}^*$  for the salt-water model, but at a much lower rate. A sharp increase of  $\theta_T^*$  is observed at  $t^* \sim 10$ , where the slope of  $\theta_T^*$  closely resembles the initial portion of the salt-water model. The temporal evolution of  $\theta_T^*$  reveals the unsteady nature of the fire, a level of complexity that is not accounted for in the hydraulic analogue. This secondary slope may be due to the ceiling layer in the source room contributing to the

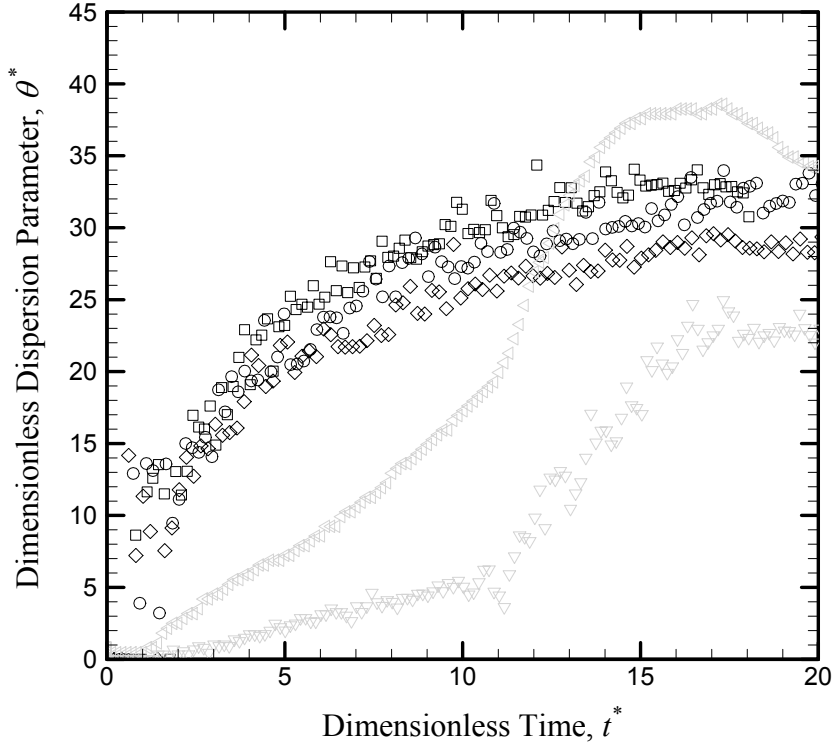


Figure 36: Dispersion parameters at detector location RM1 – C  
 $\triangleleft \theta_T^*$ ,  $\nabla \theta_{smoke}^*$ ,  $\theta_{sw}^*$  ( $\diamond$  200 ml/min,  $\circ$  150 ml/min,  $\square$  100 ml/min)

vaporization of the fuel or restricting the amount of air being entrained into the combustion region. At this location,  $\theta_{smoke}^*$  follows the same trends as described for  $\theta_T^*$  except with a reduction in slope and magnitude. It is important to note that  $\theta_T^*$  and  $\theta_{smoke}^*$  maintain the same order of magnitude as  $\theta_{sw}^*$ , for the duration of the experiment.

Similar observations are made when examining the dimensionless dispersion parameters at RM1–S, mounted on the sidewall of the source room, as shown in Figure 37. However, the scaling separation of  $\theta_{sw}^*$  is greatly improved between flow rates (approximately  $\pm 6\%$ ) in comparison to the neighboring detector RM1–C. In addition, the fluctuations in

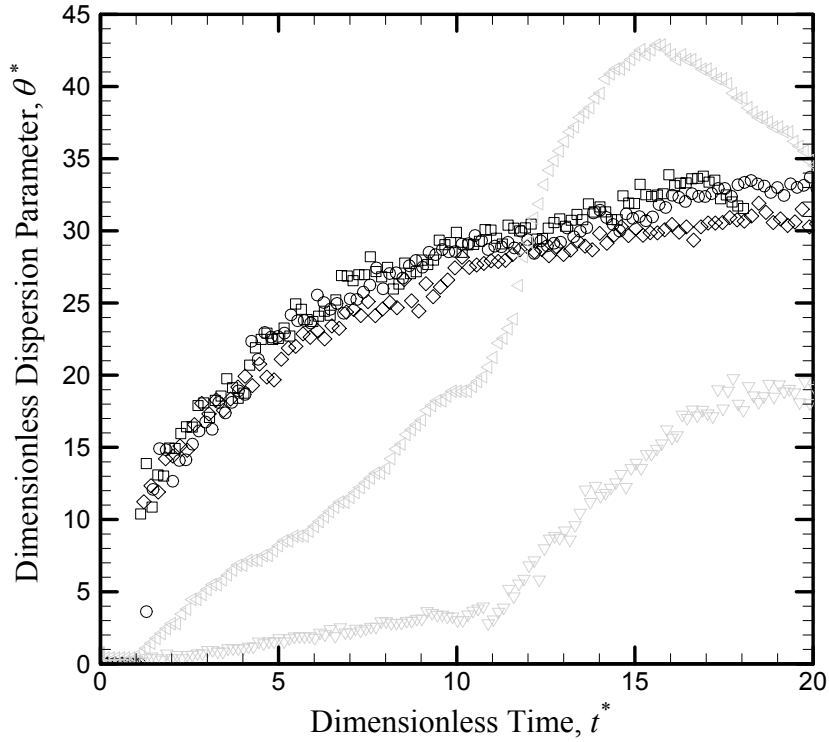


Figure 37: Evolution of dispersion parameters for detector RM1 – S  
 $\triangleleft \theta_T^*$ ,  $\nabla \theta_{smoke}^*$ ,  $\theta_{sw}^*$  ( $\diamond$  200 ml/min,  $\circ$  150 ml/min,  $\square$  100 ml/min)

$\theta_{sw}^*$  are less significant than what is observed at RM1–C. The improvement in scaling and stability is likely due to the detectors positioning being outside of the turbulent plume / ceiling jet interface. Again  $\theta_{sw}^*$  demonstrates a sharp initial increase, which begins to level off as if it were going to converge to a constant value. The  $\theta_T^*$  for this location has a sharper initial and secondary slope compared to RM1 - C and achieves a maximum value at  $\theta_T^* \approx 43$ . The  $\theta_{smoke}^*$  value is almost identical to that of RM1-C, in which it lags behind the  $\theta_T^*$  and experiences the same secondary increase but at a lower magnitude.

Additionally,  $\theta_T^*$ ,  $\theta_{smoke}^*$  and  $\theta_{sw}^*$  increase initially at approximately the same  $t^*$ .

Detector COR-C is mounted on the ceiling of the corridor outside of the doorway leading into the adjacent room, as pictured in Figure 27. A comparison of the dimensionless dispersion parameters for COR-C is provided in Figure 38. At this location the salt-water and fire dispersion parameters are significantly closer in magnitude for the duration of the experiment. Again, the initial  $\theta_{sw}^*$  increases at the same  $t^*$  as  $\theta_T^*$  and  $\theta_{smoke}^*$  with the initial slope of  $\theta_{sw}^*$  being larger. Separation is observed in  $\theta_{sw}^*$  for the different flow rates at  $t^* > 15$ . For the salt-water model a more gradual mixing process is observed at this location demonstrated by the slower increase in  $\theta_{sw}^*$ . This may be due to the subtle

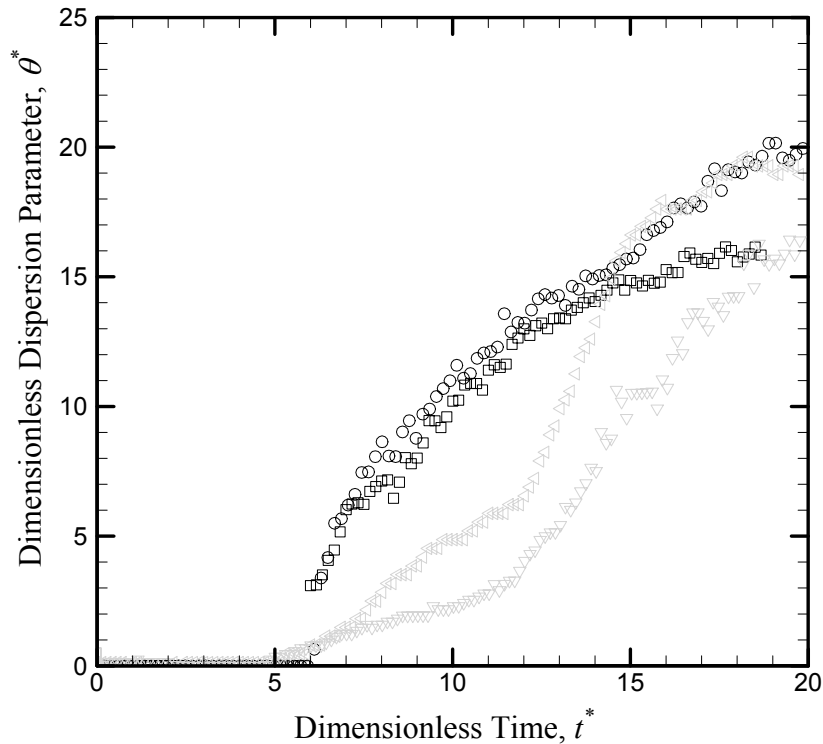


Figure 38: Evolution of dispersion parameters for detector COR – C

$\triangleleft \theta_T^*$ ,  $\nabla \theta_{smoke}^*$ ,  $\theta_{sw}^*$  ( $\circ$  150 ml/min,  $\square$  100 ml/min)

spill process from the source room into the corridor such that the front is initially weak and increases as it grows. The  $\theta_{smoke}^*$  value is still lagging behind  $\theta_r^*$  though the magnitudes are closer than what is observed at RM1-C and RM1-S.

Detector COR - S is sidewall mounted in the corridor outside of the doorway leading into the adjacent room as illustrated in Figure 27. It should be noted that the manner and duration of the salt-water experiments at this location differ from the other four detector locations. The results shown in Figure 39 are representative of three tests, run at the same flow conditions with an injection rate of 100 ml/min. This location was the first examined in the current study in which the reproducibility of the technique was tested. Though, the

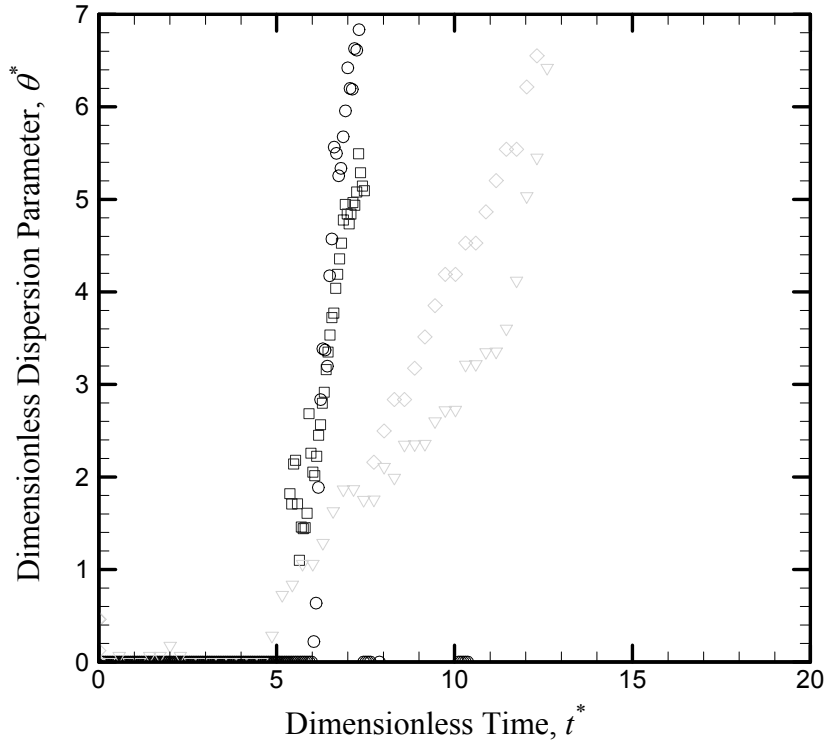


Figure 39: Evolution of dispersion parameters for detector COR – S

$\triangleleft \theta_T^*$ ,  $\nabla \theta_{smoke}^*$ ,  $\theta_{sw}^*$  @ 100 ml/min ( $\circ$  Test 1,  $\square$  Test 2)

experiments were run for a shorter duration, the results encompass the conditions beyond the time of detector activation and illustrate the initial flow dynamics, which satisfies the intent of this study. The observations for COR - S are relatively the same as for COR – C, however the slopes of the dispersive parameters are less similar.

Detector RM2 - C is ceiling mounted in the room adjacent to the source room. The exact location of RM2 – C is provided in Figure 27. The initial arrival of the front for the salt-water model is more difficult to distinguish at this location. The flow visualization images in Figure 26, help describe what is seen in the dispersion data for the adjacent room as illustrated in Figure 40. The subtle spilling from the corridor initially releases

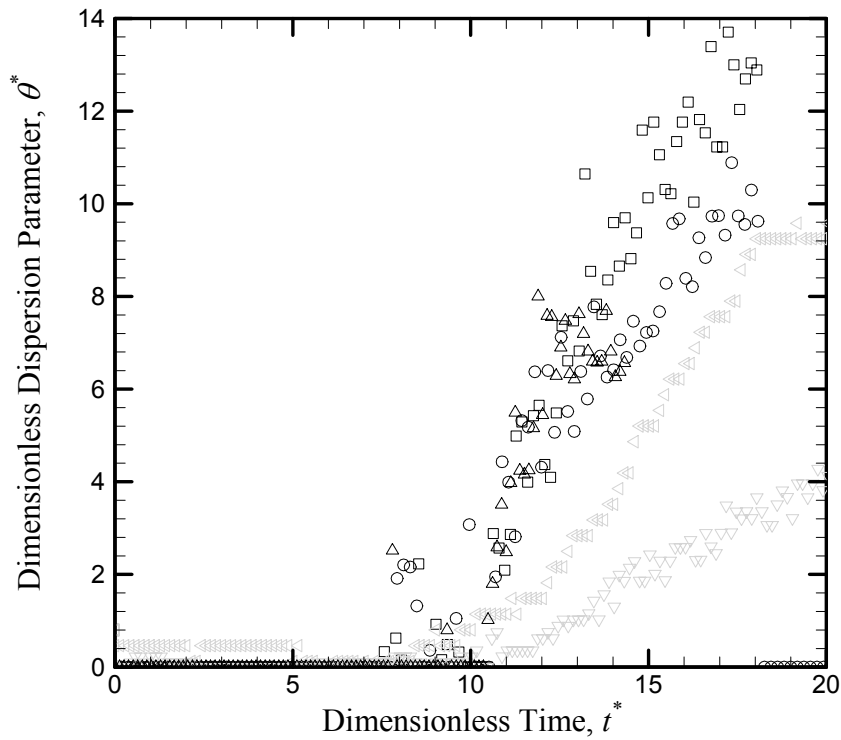


Figure 40: Evolution of dispersion parameters for detector RM2 – C  
 $\triangleleft \theta_T^*$ ,  $\triangle \theta_{smoke}^*$ ,  $\theta_{sw}^*$  ( $\circ$  150 ml/min,  $\square$  100 ml/min)

small quantities of dispersed fluid into the adjacent room, which arrive at the detector location at a variety of times. Therefore, once the doorway spill from the corridor becomes steady,  $\theta_{sw}^*$  increases similar to  $\theta_T^*$ . Although more scatter is observed in  $\theta_{sw}^*$ , the value of  $\theta_T^*$  increases at the same rate and demonstrates similar erratic characteristics early on as seen in the  $\theta_{sw}^*$ . Once again, the  $\theta_{smoke}^*$  lags behind  $\theta_T^*$  in magnitude and maintains a relatively weak rate of rise.

## Chapter 6. Conclusions

This study successfully used planar laser induced fluorescent (PLIF) diagnostics in conjunction with the salt-water analogue to obtain quantitative non-intrusive measurements of dispersion dynamics within a complex enclosure. The spatial and temporal resolved images provide a detailed look into the flow structures and dispersive dynamics for an ideal environment. The quantitative results of the PLIF technique allowed for the time evolution of dispersion parameters from the salt-water model and the full-scale fire to be compared with a detailed examination of the detector activation event.

The source based scaling used in this study proved effective in the comparative analysis of the salt-water and fire experiments. The front arrival times measured for both the salt-water and full-scale fire tests were made dimensionless and an excellent agreement was observed between the two systems. The scaled salt-water data for various flow conditions and salt mass fractions collapsed together internally with very good agreement. However, the heat losses and unsteady nature of the full-scale fire present non-ideal boundary conditions making comparisons of fire and salt-water analogue signatures challenging. Nevertheless, these dispersion signatures stay within the same order of magnitude throughout the duration of the tests and at every location examined within the enclosure even without correcting for heat loss effects. Furthermore, the heat loss effects demonstrate little significance with respect to convective dispersion dynamics within the enclosure. In addition, the scaled smoke detector activation times were shown to be a dynamic effect demonstrating little correlation with local obscuration or temperature.

This study reveals that although the magnitude of the local gas temperatures and smoke concentrations impact the detector response, a simple model based on these values alone cannot be used as a predictive indicator of detector response time. A more rational modeling alternative has been introduced where the detector response time is modeled based on the combination of a front arrival time and a detector lag time. The results show that the salt-water model accurately predicts the front arrival time at all detector locations. The activation lag time following the arrival of the front is of the same order and its significance must be appreciated. This lag reduces substantially with an increased flow velocity and is a strong function of the geometric configuration of the detectors housing as well as the relative positioning within the enclosure, i.e. ceiling or sidewall mounted. The results of the full-scale fire experiment demonstrate that the lag time maintains a relatively constant value throughout the enclosure for the ionization type smoke detectors examined in this study. However, the constant value for the lag time does change based on whether the detector is ceiling mounted or sidewall mounted. Based on these findings a constant value is used for the lag time and incorporated in the simple predictive model. Using this methodology the salt-water model accurately predicts the response time of the smoke detectors with very little error. A more sophisticated time lag model may prove necessary as more fire data becomes available. Overall, the salt-water modeling technique shows promise as a predictive tool in establishing the response of ionization smoke detectors within a complex environment.

## Appendix A: Experimental Results

Table 4: Full-Scale Fire Experimental Results

Detector Location	Measured Times, (s)			Local Conditions at Activation	
	Front Arival	Detector Activation	Activation Lag	Temperature Rise	Smoke Mass Fraction
RM1 - C	10	40	30	13.7	134.0
RM1 - S	8	22	14	8.4	55.3
COR - C	42	74	32	9.0	149.0
COR - S	37	50	13	2.4	81.2
RM2 - C	53	73.5	20.5	1.8	7.6

(x 10<sup>7</sup>)

Table 5: Non-Dimensional Fire Experimental Results

Detector Location	Non-Dimensional Times, t*			Non-Dimensional Parameters	
	Front Arival	Detector Activation	Activation Lag	Temperature	Smoke Mass Fraction
RM1 - C	1.4	5.7	4.3	7.4	1.7
RM1 - S	1.1	3.2	2.0	5.1	0.7
COR - C	6.0	10.6	4.6	4.7	1.9
COR - S	5.3	7.2	1.9	1.4	1.1
RM2 - C	7.6	10.5	2.9	1.0	0.1

Table 6: Non-Dimensional Salt-Water Model Experimental Results

Detector Location	Non-Dimensional Times, t*			Non-Dimensional Parameters
	Front Arival	Detector Activation	Activation Lag	Salt Mass Fraction
RM1 - C	1.5	5.7	4.2	19.5
RM1 - S	1.4	3.2	1.8	15.0
COR - C	6.2	10.6	4.4	9.7
COR - S	5.4	7.2	1.8	5.0
RM2 - C	8.0	10.5	2.5	0.4

## Appendix B: Check List

DATE:

TEST#

----- EXPERIMENTAL -----	----- EXPERIMENTAL -----
<input type="checkbox"/> Turn salt water pump on	<input type="checkbox"/> Dye Concentration (mg/l)
<input type="checkbox"/> Record salinity and temperature of the SW	<input type="checkbox"/> Salt Concentration (%)
<input type="checkbox"/> Circulate SW solution through tubes	<input type="checkbox"/> SW Temperature (C)
<input type="checkbox"/> Turn Laser On / record laser power	<input type="checkbox"/> Tank Water Temperature (C)
<input type="checkbox"/> Check spatial filter for proper alignment	<input type="checkbox"/> Laser power
<input type="checkbox"/> Check the vertical planar alignment	<input type="checkbox"/> Location of Max light from bottom
<input type="checkbox"/> Check proper location of light distribution	<input type="checkbox"/> Injector Location -top (mm)
<input type="checkbox"/> Measure the frame and injector locations	<input type="checkbox"/> Gain value (o'clock)
<input type="checkbox"/> Place model on frame and adjust	<input type="checkbox"/> Brightness mod
<input type="checkbox"/> Align camera and ruler for scale (IMAGE)	<input type="checkbox"/> Noise (+/- GL)
<input type="checkbox"/> Adjust and Record brightness mod	<input type="checkbox"/> CJ Peak signal (GL)
<input type="checkbox"/> Hook up injector and run preliminary	<input type="checkbox"/> Flow setting
<input type="checkbox"/> Adjust flow to 40 and stop test	<input type="checkbox"/> Tube peak signal (GL)
<input type="checkbox"/> Adjust gain and record +/- noise and peak signal	<input type="checkbox"/> Background Noise (+/- GL)
<input type="checkbox"/> Recirculate water in tank tank	<input type="checkbox"/> Calibration Peak Signal (GL)
<input type="checkbox"/> Measure light profile of tube	<input type="checkbox"/> Calibration /max Gain Peak Signal (GL)
<input type="checkbox"/> Take background image record +/- noise	
<input type="checkbox"/> Split background images!!	
<input type="checkbox"/> Begin macro for data acq.	
<input type="checkbox"/> Start flow and make sure it is ~ 40	
<input type="checkbox"/> Mix calibration tank and record peak signal	
----- POSTPROCESSING -----	----- POSTPROCESSING -----
<input type="checkbox"/> Create and Save Background image	<input type="checkbox"/> Total number of images
<input type="checkbox"/> Create and Save Calibration image	<input type="checkbox"/> Number of images prior to injection
<input type="checkbox"/> Save final tiff's (gray scale)	<input type="checkbox"/> Threshold value
<input type="checkbox"/> Save raw tiff's	<input type="checkbox"/> Cut value
<input type="checkbox"/> Save .dat file	<input type="checkbox"/> Prenoise value
	<input type="checkbox"/> Scale (pixel/cm)
	<input type="checkbox"/> X-initial

## **Appendix C: Experimental Procedure**

### **Water Treatment**

The fresh water used to fill the large tank is filtered through a high capacity sediment and rust filter. The filter is rated to 50-microns and allows a flow rate of 25 gallons per minute. The purpose of this filtration is to remove any foreign particulate from the water contained within the scale model and the large tank that would interfere with the light sheet intensity. Water treatment is necessary for the salt-water solution as well, in order to remove unwanted sediment and to reduce the hydrophobic reaction between the Rhodamine dye and the water.

In preparing the saline solution, a large 40-gallon container is filled with warm tap water in which a nylon bag filled with water softening rock salt (NaCl) is suspended in the water. The salt is suspended and not just placed in the water to accelerate the mixing process. The heavy salt water moves to the bottom of the container allowing the rock salt to be exposed to fresh water, this natural convection allows the salt to completely dissolve in the water without any forced mixing. The initial salt mixture is made at a relatively high concentration, around 20 percent NaCl by mass. The high concentration saline solution is then filtered from the large mixing tank to a secondary container where the salt mass fraction is measured and adjusted accordingly by mixing in additional fresh water. From the secondary container the saline solution is filtered once again into a 5-gallon food grade plastic carboy. It has been observed by previous researchers that residual chlorine reacts with Rhodamine 6G. The reaction causes a significant decay in the dye concentration. The chlorine level of the solution is tested using a chlorine test kit and the chlorine is removed by adding a small amount of de-chlorinating agent to the

solution. The mixture is agitated for several minutes, poured into the top section of the gravity feed system, and mixed with the prescribed amount of Rhodamine 6G dye. The inline filter used for the treatment of the salt-water solution is a carbon based sediment and rust filter with a 5-micron rating and a maximum filtration rate of 5-gallons per minute. The water is driven through the filter using a submersible salt-water fish tank pump.

### **Dye Treatment**

Rhodamine 6G is used as the fluorescent dye for the PLIF diagnostics within this study. The lab grade Rhodamine dye is 99.9% pure and is purchased in solid form from Lycros Chemicals Inc. In pure form, the dye must be stored in a dry environment and kept away from any ambient light. It is important to note, that prepared laser dye solutions usually contain very minute amounts of dye. Thus, the type of solvent used as well as its purity is of great importance. Impurities and additives may strongly effect the lifetime of the dye and may catalyze photochemical reactions. For this reason distilled water is used as the preliminary solvent. The pure dye is weighed using a precision digital scale with an accuracy of  $\pm .001$  grams. An initial solution is made with a concentration of 0.1 grams of dye per liter of solute, which is added, in liquid form, to the saline solution prior to experimentation.

### **Gravity Feed System**

Prior to each experiment a 5 gallon volume of salt-water solution is prepared and the salinity is measured using a hydrometer. The large fresh water tank is filled with filtered tap water and the temperature is monitored, adjusted and recorded. The treated saline

solution is transferred to the top container of the gravity feed system and the temperature is measured and recorded using a mercury/glass thermometer. The temperature of the saline solution and the water within the enclosure is measure to assure that the density. The necessary amount of concentrated dye solution is added to the treated salt-water and agitated by hand with a glass-stirring rod to ensure proper mixing; the dye concentration used is tabulated.

### **Optical Setup**

It should be noted that much care has been taken to maintain a stable optical set up for creation of the light sheet, however, it is still necessary to ensure the optics are correct prior to each experiment. The Argon-Ion laser is activated and the power is reduced to 40 mW for the duration of the optical alignment. The proper alignment of the spatial filter is confirmed by placing a white piece of paper between the collimating lens and the spatial filter. If the expanded beam is not perfectly round then adjustments must be made. Any adjustment made to the spatial filter necessitates a realignment of the collimating lens. This is done by; 1) changing the location of the collimating lens with respect to the spatial filter, manually on the optical traverse system, and 2) placing two adjustable apertures in the optical path beyond the lens to ensure the beam diameter remains constant. After adjusting both the spatial filter and the collimating lens, the focus is placed on the optical mirrors. Both mirrors are cleaned of excess dust and debris using an optical cleaning cloth. The alignment of the optical mirrors is established by passing the collimated beam through a series of adjustable apertures in the beam path beyond the mirrors. Once this is complete the next step is to establish the proper position of the laser sheet.

### **Laser Sheet Alignment**

Preliminary tests have been conducted to locate the optimal light sheet dimensions and position, for each plane of interest within the room-corridor-room model. Because of the Gaussian light intensity distribution, the vertical location of the light sheet is of great significance. It is important that the sheet is introduced in such a manner that the area of most significance is adequately illuminated, while at the same time providing adequate illumination throughout the entire spatial domain. Several steps are required prior to experimentation in order to assure the laser sheet is oriented properly. First, the cylindrical lens is removed from the beam path and the vertical location of the beam is measured, at two locations, from the top of the model frame within the large freshwater tank; the values are compared to prior tests, adjusted, and recorded. The height and angle of the horizontal beam is varied by carefully adjusting the optical mirrors. Next, the cylindrical lens is replaced and the vertical planar alignment is conducted by passing the laser sheet through a plum line. For the final step the laser power is set to 500 mW and the light intensity distribution is tested. The laser sheet is passed through an acrylic cylindrical tube filled with 0.02 mg/L of dye and vertically suspended from the large tank at two specific locations. Instantaneous images are recorded and the light sheet distribution is plotted. The profile is evaluated in two ways: 1) by the pixel location of the maximum light intensity and 2) the distance from the max to 50% of the max. If necessary the sheet is adjusted to match prior tests. If further adjustments are necessary the power of the laser must be reduced.

### **Image Acquisition**

The polycarbonate scale model is placed on the positioning system within the large freshwater tank. The CCD camera is positioned and adjusted based on the geometric view

factor of the planar sheet. Then, a standard stainless steel ruler is placed vertically in the model within the path of the laser sheet. The camera is focused on the ruler and an image is recorded to represent the physical scale of the test images. Next, the room lights are turned off and the aperture of the camera is fully opened. Within the image acquisition software the brightness modification is adjusted to ensure that the background noise is greater than zero and the percent modification is tabulated.

Prior to the first experiment it is necessary to complete several steps that are not required until the setup is changed. Firstly, the position of the injector is measured with calipers, adjusted, and recorded. Secondly, the tube from the delivery system is connected to the injector and a high flow rate of saline solution is sent through the lines to remove any air bubbles present in the injector or in the lines. The flow rate is then adjusted to that required for testing and the camera's gain is adjusted to prevent saturation.

Preceding each experimental run, a series of background images are recorded and the +/- background noise values are tabulated. The image acquisition program is triggered prior to the injection of the saline solution; the relative time is recorded and tabulated.

Following each experiment the new flow rate is adjusted and the water in the model is recirculated until no dye is visible. After the experiments are conducted a series of calibration images are recorded in which model is filled with a known dye concentration. Only one average calibration image is needed for each series of tests representing a geometric planar slice. Finally, the model enclosure is removed from the large tank and replaced by a stainless steel injector. The injector is positioned slightly above the

maximum light intensity region of the laser sheet. Dyed salt-water is injected into the tank at various dye and salt concentrations and an average of 300 images is taken. The initial region of these forced plumes have a known salt and dye concentration and can be used to determine the effect of salt on the fluorescence intensity. This effect is included in calibration. The respective values for the dye concentrations and salt mass fractions are reported.

### **Converting Raw Tiff Images**

The captured images are saved in binary format, in which the two consecutive images for each time step are contained in a single binary file. A macro written within the data acquisition program is used to separate the files, convert them into tiff images, and assign a proper file name accordingly. The calibration and background binary files are separated into a series of tiff images as well. The raw tiff images are then transferred to an ftp file server in which they are backed up and are now accessible to the university's Unix based servers. The program X-Win32 is used to gain access to the Unix servers from a Windows based PC. Within the Unix server a temporary directory is created from which the raw tiff images are transferred.

### **Processing Data**

Several procedures have been written in the international data language program (IDL) for post processing and analysis. The foundation of these programs is based on converting an 8-bit tiff image into quantitative data. The images are read in and then each row and column is scanned allowing the grayscale for each pixel within the image to be converted into a numerical array. For the first stage of post processing a program reads in the raw background images and combines them into a single average background image

that is saved for further data analysis. Taking the average of several hundred images allows the digital noise to be removed, leaving only the noise associated with the enclosure itself. A similar program is used to create an average calibration image. The program subtracts out the average background image prior to saving the average calibration image. The calibration image allows the laser sheet profile to be quantified spatially thus providing a means to normalize the experimental images.

The instant image code is somewhat complex and is used as one of the final steps in processing the data. Prior to normalization there are several steps that must be performed in order to create a clean image with sufficient depth. The following parameters are input variable defined by the user:

CUT – defines the maximum multiplication factor from the light sheet

THRESH – defines the minimum value that the normalized image can have

PRENOISE – defines a minimum value for the image prior to normalization

CJPOINTVALUE – defines the grayscale value of a specified point of interest which creates an image multiplication factor

SCALE – defines length scale in terms of the amount of pixels in one centimeter

ORIGINX – defines the initial x-location of the image

ORIGINY – defines the initial y-location of the image

TIMESHIFT – defines the time lapse prior to the flow of saline solution

Using the scale image taken prior to the experiment, the pixel location of the enclosures origin and the actual ratio of the image in pixels to the model in centimeters can be

obtained. These are the first values to be defined by the user in the instant image post processing code. The program is written to map out the boundaries of the enclosure for all specific configurations as well as the location of the probes representative of the smoke detectors in the full-scale experiment. There are several input parameters that define the experimental configuration and the manner in which the raw images will be processed.

To input the proper values for post processing it is necessary to first load up a set of images that is representative of a steady state flow. The program can be run and the processed image can be evaluated. Adjusting the CUT, THRESH, and PRENOISE values before running the entire set of test data allows the bounds of the normalized image to be set by the user and removes the digital noise from the raw images prior to the normalization. Once these inputs are optimized, the CJPOINTVALUE is set to prescribe an acceptable gray level at a specific point of interest. For a ceiling jet flow that is downstream of the impinging plume, a gray scale value of 100 out of 255 is acceptable for the research at hand. The program will then process the steady state image and output a multiplication factor for the entire spatial domain based on the prescribed gray level. This assures that finalized images will have good resolution within the area of interest. Due to the fact that the testing requires the image acquisition to begin prior to the introduction of the saline solution, it is necessary for the time lapse to be an input parameter within the code. This allows the program to save the images with a time stamp resembling the time from the initial introduction of the source.

The “instant images” program uses several steps in order to process the raw images. The program first reads in both consecutive images for each time step and converts the images into two numerical arrays. Since the images taken are interlaced the program is written to read every other row of the array and stretch the values to fill the original spatial coordinates. Now there are four arrays/images representative of a single time step. These images are then added together and the average background image is subtracted. A multiplication factor is applied to the clean images to correct for the Gaussian light intensity distribution. The program creates the multiplication factor for the entire spatial domain by loading the average calibration image in as a numerical array and dividing the maximum gray level by this entire array. Finally, the corrected gray level values are converted into values representative of the salt mass fraction by applying a third order polynomial interpolation. The computation repeated for each time step of the experiment.

### **Output Parameters**

The program is written to output the processed data in several formats. The final and clean images, in terms of gray level, are saved as tiff images for each respective time step. A data file is also created to allow the quantitative images to be open in TecPlot.

The data file consists of the spatial coordinates of each pixel, the gray level value, the salt mass fraction, the non-dimensional salt mass fraction, and the non-dimensional time (for probe locations). The point measurements made at the relative locations of each smoke detector are presented in terms of non-dimensional mass fraction vs. non-dimensional time, which are used in comparison with the full-scale test results.

## Bibliography

1. Munson, B. R., Young D. F. and Okiishi T.H., (1998) "Fundamentals of Fluid Mechanics," 3<sup>rd</sup> Ed., John Wiley and Sons, New York.
2. Drydale, D.D., (1998) "An Introduction to Fire Dynamics," 2<sup>nd</sup> Ed., John Wiley and Sons, New York.
3. Worrell, C.L., Lynch, J.A., Jomass, G., Roby, R.J. (2003) "Effect of Smoke Source and Horn Configuration on Enhanced Deposition, Acoustic Agglomeration, and Chladni Figures in Smoke Detectors," *Fire Technology*, 39, pp. 309-346.
4. Thomas, P.H., Hinkley, P.L., Theobald, C.R. and Simms, D.L., (1963) "Investigations into the Flow of Hot Gases in Roof Venting," *Fire Research Technical Paper No. 7*, HMSO, London.
5. Tangren, E. N., Sargent, W. S. and Zukoski, E. E., (1978) "Hydraulic and Numerical Modeling of Room Fires," California Institute of Technology, Pasadena, California.
6. Zukoski, E.E, (1978) "Prediction of Smoke Movement in Buildings," California Institute of Technology, Pasadena, Ca.
7. Steckler, K.D, Baum, H.R., and Quintiere, J.G (1986) "Salt Water Modeling of Fire Induced Flows in Multi-Compartment Enclosures," NBSIR 86-3327, Gaithersburg, MD: National Bureau of Standards.
8. Kelly, A. A. (2001) "Examination of Smoke Movement in a Two-Story Compartment Using Salt Water and Computational Fluid Dynamics Modeling," M.S. Thesis, Dept. Fire Protection Engineering, University of Maryland, College Park, MD.
9. Webster, D.R. and Liu, Y. (2001) "Velocity Measurements of Turbulence Collapse in a Linearly Stratified Jet," *Experiments in Fluids*, vol. 31(4), pp. 394-400.
10. Houssine, I., Vivier, H., Plasari, R. and Villermaux, J. (1996) "Planar laser induced fluorescence technique for measurements of concentration fields in continuous stirred reactor tanks," *Exp. Fluids*, Vol. 22, pp. 95 – 102.
11. Fukushima, C., Aanen, L., Westerweel, J. (2000) "Investigation of the Mixing Process in an Axisymmetric Turbulent Jet Using PIV and LIF," Laboratory for Aero and Hydrodynamics, Delft University of Technology, The Netherlands.

12. Lengright, J. and Graw, K-U. (1995) "Flow Field Analysis Beneath Gravity Waves. In: Flow Visualization and Image Processing of Multiphase Systems," ASME, FED 209, pp. 57 – 64. New York.
13. Law, A.W. K. and Wang, H. (2000) "Measurement of mixing processes with combined digital particle image velocimetry and planar laser induced fluorescence", *Exp. thermal and Fluid Science*, **22**, 213-229.
14. Peters, W.D., Codswell, S.R., and Venart, J.E.S (1997) "Mixing in Gravity Current Heads Flowing Over Rough Surfaces," Developments in Laser Techniques and Fluid Mechanics, Eds. R.J. Adrian et al., Springer Berlin, Ch. III, pp. 325 – 339.
15. Clement, M.J. (2000) "Experimental Verification of the Fire Dynamics Simulator (FDS) Hydrodynamic Model," PhD Thesis Draft, University of Canterbury, New Zealand.
16. Baum, H.R., Rehm, R.G. (1984) "Calculations of Three Dimensional Bouyant Plumes in Enclosures," National Bureau of Standards, Washington, DC.
17. Rehm, R.G, Baum, H.R (1978) "The Equations of Motion for Thermally Driven Buoyant Flows," *N.B.S J. Res.* 83, 297.
18. Turner, J.S. (1973) "Buoyancy Effects in Fluids," Cambridge University Press, Cambridge.
19. Morton, B.R., Taylor, G.I., and Turner, J.S. (1956) "Turbulent Gravitational Convection from Maintained and Instantaneous Sources," Proc. of the Royal Society of London, Vol. 234, Issue 1196, pp. 1 – 23.
20. Dai, Z., Tseng, L.K., and Faeth, G.M. (1994) "Structure of Round, Fully-Developed, Buoyant Turbulent Plumes," Journal of Heat Transfer, Vol. 116, pp. 409-417.
21. Morton, B.R. (1959) "Forced Plumes," Journal of Fluid Mechanics, Vol. 5, pp. 151 - 163.
22. Heskestad, G. and Delichatsios, M.A., (1977) "Enviornments of Fire Detectors – Phase I: Effect of Fire Size, Ceiling Height and Material," Volume I and II, National Bureau of Standards, Gaithersburg, MD.
23. Schifiliti, R. P. and Pucci, W. E. (1996) "Fire Detection Modeling: State of the Art," Fire Detection Inst., Bloomfield, CT, p. 57.

24. Bukowski, R. W. and Averill, J. D. (1998) "Methods for Predicting Smoke Detector Activation," Building and Fire Research Laboratory, National Institute of Standards and Technology, Gaithersburg, MD 20899, USA.
25. Evans, D. and Stroup, D., (1985) "Methods to Calculate the Response Time of Heat and Smoke Detectors Installed Below Large Unobstructed Ceilings," NBSIR 85-3167, National Bureau of Standards, Gaithersburg, MD.
26. Milke, J. A., (1990) "Smoke Management for Covered Malls and Atria," Fire Technology, Vol. 26, No. 3, pp. 223 - 243.
27. Beyler, C. and DiNenno, P., (1991) "Letters to the Editor," Fire Technology, Vol. 27, No. 2, pp. 160 – 169.
28. Davis, W.D. and Notarianni, K.A., (1996) "NASA Fire Detector Study," NISTIR 5798, National Institute of Standards and Technology.
29. Mowrer, F.W. and Friedman, J., (1998) "Experimental Investigation of Heat and Smoke Detector Response," Proceedings of Fire Suppression and Detection Research Application Symposium, pp. 256 – 264.
30. Geiman, J. A. and Gottuk, D. T., (2003) "Alarm Thresholds for Smoke Detector Modeling," Fire Safety Science – Proceedings of the 7<sup>th</sup> International Symposium, International Association for Fire Safety Science, pp. 197 – 208.
31. Schifiliti, R.P., Meacham, B.J. and Custer, R.L.P., (2002) "Design of Detection Systems," SFPE Handbook of Fire Protection Engineering, 3<sup>rd</sup> edition, National Fire Protection Association, Quincy, MA.
32. Geiman, J.A., (2003) "Evaluation of Smoke Detector Response Estimation Methods," Masters Thesis, University of Maryland Department of Fire Protection Engineering.
33. Bukowski, R.W. and Mulholland, G.W., (1978) "Smoke Detector Design and Smoke Properties: Final Report," NBS Technical Note 973, National Bureau of Standards, Gaithersburg, MD.
34. Cleary, T., Chernovsky, A., Grosshandler, W. and Anderson, M., (2000) "Particulate Lag Entry in Spot-Type Smoke Detectors," Fire Safety Science – Proceedings of the 6<sup>th</sup> International Symposium, International Association for Fire Safety Science, pp. 779 –780.
35. Bejan, A. (1984), "Convection Heat Transfer," Wiley Publications, New York.
36. Chandrasekhar, S. (1957), "An Introduction to the Study of Stellar Structure," New York: Dover

37. Walker, D.A. (1987), "A Fluorescence Technique for Measurements of Concentration in Mixing Liquids," Journal of Physics E: Scientific Instruments, Vol. 20, pp. 217 – 224.
38. Guilbault, G.C. (1973) "Practical Fluorescence," New York: Marcel Dekker.
39. Arcoumanis, C., McGuirk, J.J., and Palma, L.M. (1990) "On the Use of Fluorescent Dyes for Concentration Measurements in Water Flows," Experiments in Fluids, Vol. 10, pp. 177 – 180.
40. Davidson, M.J., Pun, K.L., Wang, H.J. (1997) "Applications of laser induced fluorescence and image processing in observing plume behavior." Proc. 3<sup>rd</sup> Int. Conf. On Fluid Dynamic Measurements and its Applications, International Academic, Beijing, China.
41. Barbrauskas, V. (1995) "The cone calorimeter," SFPE Handbook of Fire Protection Engineering, 2<sup>nd</sup> Edition, pp. 3.37 – 3.52, Society of Fire Protection Engineering, Boston.